A CAR-BORNE SAR SYSTEM FOR DEFORMATION MONITORING: POSITIONING AND INTERFEROMETRIC PERFORMANCE ANALYSIS

A thesis submitted to attain the degree of

DOCTOR OF SCIENCES of ETH ZURICH
(Dr. sc. ETH Zurich)

presented by

Roberto Coscione

Laurea Magistrale in Ingegneria delle Telecomunicazioni
Università degli studi di Napoli Federico II
born on 10.02.1985
citizen of Italy

accepted on the recommendation of

Prof. Dr. Irena Hajnsek
Prof. Dr. Andreas Reigber
Dr. Gianfranco Fornaro
Dr. Othmar Frey

2021

Contents

ABSTRACT

Synthetic aperture radar (SAR) is a well established imaging technique used in a broad range of Earth monitoring applications, such as topographic mapping, landslides and rockfall monitoring, glacier surface velocity and mass balance estimation, and much more. Specifically, changes in the order of a fraction of the electromagnetic wavelength occurring in the imaged areas can be measured via repeat-pass differential SAR interferometry (DInSAR), in which temporally separated SAR acquisitions of the same area are coherently combined.

In this context, spaceborne SAR systems are an invaluable asset thanks to their capability to provide global coverage over extended periods of time. However, due to the fixed satellite revisit time, the temporal resolution of spaceborne SAR systems can be insufficient to monitor fast surface changes. Furthermore, the monitoring of areas characterised by steep slopes with respect to the radar look angle, such as in mountainous regions, is challenged by geometric distortions occurring in the SAR imagery due to the acquisition geometry, such as layover and shadowing.

On the other hand, airborne SAR systems can offer a larger flexibility in terms of revisit time and, potentially, more favourable acquisition geometries for the observation of steep slopes, but their extended and regular use is limited by the high acquisitions cost.

In light of the above, ground-based (or terrestrial) radar systems offer valuable and complementary monitoring capabilities. In fact, despite the lower coverage area compared to airborne and spaceborne systems, ground-based radar systems can easily achieve high temporal resolutions, on the order of minutes or even seconds, necessary to sample fast and potentially non-linear deformation phenomena at low acquisitions cost. Furthermore, they offer an optimal acquisition geometry for steep surface slopes, which makes them ideal for monitoring local-scale surface changes such as rockfall and landslides.

Nevertheless, given the limited length of their (real or synthetic) antenna, ground-based radar systems are constrained to use high frequency bands, typically X- or Ku-band, to achieve good azimuth resolutions. However, the temporal decorrelation behavior of high frequency bands is such that the monitoring capabilities of ground-based systems are limited to short time spans or to surfaces free of vegetation cover due to the high temporal decorrelation of the high frequency bands. With the objective to monitor deformation phenomena over relatively long time spans also in natural areas potentially covered by vegetation, the use of radar systems operating in lower frequency bands, such as L-band, is desirable to achieve better decorrelation properties over time (lower temporal decorrelation). To this aim, it is necessary to remove the physical constraint on the maximum achievable length of the synthetic antenna.

In this research work a car-borne SAR system aimed at DInSAR applications in natural areas is presented. A car-borne SAR allows to employ a radar transmitter operating at L-band while still achiev-

ing a good azimuth resolution thanks to the possibility to form long synthetic apertures through the movement of the car along a (potentially curvilinear) road. Furthermore, given the availability of a sufficiently long road with unobstructed line of sight to the target area, the car-borne system can theoretically achieve the full SAR azimuth resolution equal to half the length of the real antenna. Nevertheless, compared to rail-based or stationary radars, a car-borne SAR system requires accurate position and attitude measurements of the antenna phase centre during the acquisitions in order to minimize focusing errors. Inertial navigation systems integrated with global navigation satellite systems (INS/GNSS) are typically employed for such purpose.

The first investigation presented in this dissertation reports the analysis of the positioning accuracy of a high-performance INS/GNSS system achieved both within the SAR integration time and between different passes of the radar platform, relevant for repeat-pass DInSAR applications. A controlled (rail-based) setup was employed to achieve an almost perfect repeatability of the radar platform over multiple passes while performing positioning and radar measurements. The positioning accuracy was assessed in function of the distance of the platform from different GNSS reference stations employed for differential GNSS processing. The impact of the positioning errors on the repeat-pass interferometric performance was then evaluated by analysing the differential interferometric phase obtained with SAR data focused with each of the different INS/GNSS trajectories and by comparing it with the interferometric phase of SAR data focused with the nominal trajectory. Additionally, a non-standard interferometric combination of the SAR imagery, entailing the use of SAR acquisition pairs focused from the same raw data but using the nominal trajectory and the measured one, respectively, allowed to isolate the positioning-related phase errors from the interferometric phase owed to surface deformations and to tropospheric phase gradients. The results showed the interferometric phase error trends caused by the limited positioning accuracy achieved by using remote reference stations of the national network of permanent GNSS receivers as a consequence of the large influence of the post-processed GNSS data on the final positioning solution. On the other hand, a large reduction of interferometric phase errors can be accomplished by using a GNSS receiver located in the vicinity of the SAR platform during the SAR acquisitions, indicating that such approach is critical for DInSAR applications.

The second investigation is focused on the repeat-pass interferometric performance achievable with the L-band car-borne SAR system when employed for the observation of a natural terrains characterised by the presence of vegetation. In particular, the objective was to evaluate the level of interferometric coherence and phase stability achievable in different classes of land cover over short and medium time spans (on the order of minutes, hours, and days) and with increasing temporal baselines. Additionally, an analysis of the interferometric fluctuations in relation to the environmental state of the imaged areas subject to time-varying weather conditions was conducted. The results showed an overall high coherence level with temporal baselines up to about two weeks also in vegetated areas, denoting the limited temporal decorrelation in such time span thanks to the robustness of the L-band electromagnetic signals towards small changes in the imaged area and the potential to perform deformation monitoring in natural terrains. The strong influence of the environmental changes on the interferometric coherence and phase was also observed, in particular due to wind and changes in the moisture level due, for example, to rainfalls, with marked differences depending on the land cover type.

In conclusion, a car-borne SAR is a valuable remote sensing system that can complement the existing spaceborne and airborne SAR systems for the retrieval of geophysical information of interest in a flexible and cost-effective fashion.

Sommario

Il radar ad apertura sintetica (SAR) è una tecnica di imaging ben consolidata e utilizzata in una vasta gamma di applicazioni per il monitoraggio della Terra tra cui mappatura topografica, monitoraggio di frane e caduta massi, valutazione di effetti post-sismici e stima del bilancio di massa e della velocità di scorrimento dei ghiacciai. In particolare, cambiamenti intervenuti nella zona osservata nell'ordine di una frazione della lunghezza d'onda elettromagnetica possono essere misurati tramite l'interferometria SAR differenziale a passaggi ripetuti (DInSAR), in cui acquisizioni SAR di una stessa area separate nel tempo sono combinate in modo coerente.

Grazie alla loro capacità di fornire una copertura globale per lunghi periodi di tempo, i sistemi SAR satellitari rappresentano un prezioso asset per l'osservazione della Terra. Tuttavia, a causa del tempo di rivisitazione fisso, la risoluzione temporale dei sistemi SAR satellitari può risultare insufficiente per monitorare cambiamenti rapidi delle aree osservate. Inoltre, superfici caratterizzate da forti pendenze rispetto all'angolo di vista del radar, come quelle tipicamente presenti in zone montuose, sono soggette a distorsioni geometriche, quali il *layover* e lo *shadowing*), che limitano la possibilità di una corretta stima dei parametri di interesse. D'altra parte, i sistemi SAR da aereo offrono una maggiore flessibilità in termini di tempo di rivisitazione e geometrie di acquisizione potenzialmente più favorevoli per l'osservazione di pendii ripidi, ma l'uso esteso e regolare di tali sistemi trova un limite negli alti costi di acquisizione.

Alla luce di quanto sopra, i sistemi radar terrestri offrono capacità di monitoraggio complementari ai sistemi precedentemente descritti. Infatti, nonostante offrano una minore area di copertura rispetto ai sistemi SAR satellitari e da aereo, i sistemi radar terrestri permettono di ottenere un'alta risoluzione temporale, nell'ordine di minuti o secondi, necessaria per campionare fenomeni di deformazione rapidi e potenzialmente non lineari. Inoltre, grazie ai bassi costi di acquisizione e alla geometria di acquisizione ottimale per l'osservazione di pendii ripidi, i radar terrestri sono strumenti ideali per il monitoraggio di fenomeni di deformazione su scala locale quali la caduta massi e le frane.

Tuttavia, a causa della limitata lunghezza dell'antenna (reale o sintetica) impiegata dagli stessi, i sistemi radar terrestri sono tipicamente vincolati ad utilizzare alte bande di frequenza, generalmente X o Ku, al fine di ottenere una buona risoluzione spaziale in azimut. Ciò implica che la capacità di monitoraggio di tali sistemi sia limitata a superfici prive di vegetazione o ad acquisizioni separate da brevi intervalli temporali a causa dell'elevata decorrelazione temporale tipica delle alte frequenze, particolarmente problematica in aree coperte da vegetazione. Con l'obiettivo di monitorare fenomeni di deformazione su finestre temporali relativamente lunghe anche in aree naturali potenzialmente coperte da vegetazione, è raccomandabile l'uso di sistemi radar operanti a basse frequenze, ad esempio in banda L, allo scopo di ottenere migliori proprietà di decorrelazione nel tempo (minore decorrelazione temporale). A

tal fine, è necessario rimuovere il vincolo fisico della lunghezza massima dell'antenna reale o sintetica tipicamente ottenibile con sistemi radar terrestri (nell'ordine di alcuni metri).

Il presente lavoro di ricerca tratta di un sistema SAR da auto finalizzato ad applicazioni DInSAR in aree naturali. Un SAR da auto permette di utilizzare un trasmettitore radar operante in banda L pur ottenendo una buona risoluzione azimutale grazie alla possibilità di formare lunghe aperture sintetiche tramite il movimento dell'auto lungo una strada (potenzialmente curvilinea). Inoltre, qualora vi sia una strada sufficientemente lunga e la linea di vista verso l'area di interesse sia libera, il sistema SAR da auto può teoricamente raggiungere la massima risoluzione azimutale SAR pari alla metà della lunghezza dell'antenna reale. Tuttavia, rispetto ai sistemi radar terrestri stazionari o su rotaia, un sistema SAR da auto richiede accurate misure di posizione e di orientamento del centro di fase dell'antenna durante l'acquisizione SAR al fine di minimizzare errori di focalizzazione. Tali misure di posizione e orientamento sono generalmente eseguite tramite sistemi di navigazione inerziale integrati con sistemi globali di navigazione satellitare (INS/GNSS).

La prima indagine presentata in questa dissertazione riguarda l'analisi dell'accuratezza di posizionamento di un sistema INS/GNSS ad alte prestazioni ottenuta sia durante il tempo di integrazione SAR sia tra diversi passaggi della piattaforma radar, pertinente ad applicazioni DInSAR a passaggi ripetuti. L'analisi è stata condotta utilizzando un setup di misurazione controllato (basato su rotaia) che ha permesso di ottenere una ripetibilità quasi perfetta del movimento della piattaforma nei diversi passaggi durante l'esecuzione di misure di posizionamento e radar. L'accuratezza di posizionamento è stata valutata in funzione della distanza del radar da diverse stazioni di riferimento GNSS impiegate per l'elaborazione GNSS differenziale. L'impatto degli errori di posizionamento sulle prestazioni interferometriche è stato poi esaminato analizzando la fase interferometrica differenziale ottenuta con dati SAR focalizzati con ciascuna delle diverse traiettorie INS/GNSS e confrontandola con la fase interferometrica dei dati SAR focalizzati con la traiettoria nominale. Inoltre, una combinazione interferometrica non standard delle immagini SAR, che consiste nell'uso di coppie di acquisizioni SAR focalizzate partendo dagli stessi dati grezzi ma utilizzando, rispettivamente, la traiettoria nominale e quella misurata, ha permesso di isolare gli errori di fase legati al posizionamento dai contributi di fase interferometrici dovuti alle deformazioni della superficie e ai gradienti di fase troposferici. I risultati hanno mostrato l'andamento degli errori di fase interferometrici causati dalla limitata precisione di posizionamento dovuta all'utilizzo di stazioni di riferimento remote della rete nazionale di ricevitori GNSS permanenti, in conseguenza dell'alta influenza dei dati GNSS post-processati sulla traiettoria finale. D'altra parte, utilizzando un ricevitore GNSS situato nelle vicinanze della piattaforma durante le acquisizioni SAR, ü stata realizzata una considerevole riduzione degli errori di fase, indicando l'importanza di tale approccio per applicazioni DInSAR.

La seconda indagine è incentrata sulle prestazioni interferometriche repeat-pass ottenibili con il sistema SAR da auto in banda L impiegato per l'osservazione di un area caratterizzata dalla presenza di vegetazione. In particolare, l'obiettivo è stato quello di valutare il livello di coerenza interferometrica e la stabilità di fase ottenibili in diverse classi di copertura del suolo su intervalli di tempo brevi e medi (dell'ordine di minuti, ore e giorni) e con baseline temporali crescenti. Inoltre, è stata condotta un'analisi delle fluttuazioni interferometriche in relazione alla variabilità delle condizioni ambientali nel tempo. I

risultati hanno mostrato un livello di coerenza complessivamente elevato con baseline temporali fino a circa due settimane anche in aree vegetate, denotando la limitata decorrelazione temporale in tale arco di tempo grazie alla robustezza dei segnali elettromagnetici in banda L rispetto a piccoli cambiamenti della zona interessata e indicando la possibilità di eseguire il monitoraggio delle deformazioni in terreni naturali. È stato altresì osservato il notevole impatto dei cambiamenti ambientali sulla coerenza interferometrica e sulla fase, in particolare quello del vento, della pioggia e, in generale, e delle variazioni di umidità, con marcate differenze a seconda del tipo di copertura del suolo.

In conclusione, un SAR da auto è un valido sistema di telerilevamento che può integrare gli esistenti sistemi SAR satellitari e da aereo per il recupero di informazioni geofisiche di interesse in maniera flessibile.

1

INTRODUCTION

1.1 BACKGROUND

E ARTH observation is of primary importance on global, national, and local levels to monitor and understand environmental changes over time. Research institutes, policy makers, and stakeholders seek for timely, integrated, and material information to understand past and future environmental trends, to identify critical areas in need for intervention, and to develop policies and protocols aimed at reducing the negative impacts of natural hazards on the population and on the economy. Data collection, processing, interpretation, and modelling are required to track natural and anthropogenic environmental changes and to support the development of our knowledge base.

In this context, the employment of spaceborne, airborne, and ground-based remote sensing instruments is of paramount importance.

Spaceborne systems   Satellite remote sensing plays a fundamental role in providing continuous and wide-area measurements using various bands of the electromagnetic spectrum. Specifically, spaceborne synthetic aperture radar (SAR) systems represent an invaluable asset for the observation of Earth's surface. Differently from optical systems, whose measurements can be obstructed by clouds, fog, and rain, SAR systems use microwave signals that are able to provide all-weather observation capabilities [1]. Moreover, since radar systems are active sensors, they do not rely an external illumination sources and can perform day and night observations. Such characteristics are essential to obtain continuous data time-series necessary to understand global trends over long time spans and to maintain key environmental indicators up to date [2]. Topographic mapping [3], landslides and rockfall monitoring [4, 5], post-seismic assessments [6, 7], glacier surface velocity and mass balance estimation [8, 9], are only some of the possible fields of applicability of the SAR imagery. With the ever increasing involvement of numerous governmental and commercial players in the SAR field, progressively more extensive monitoring capabilities are being offered.

Airborne systems   While spaceborne SAR systems are critical for global and continuous monitoring of Earth's environmental dynamics, airborne SAR systems are particularly appealing for their flexibility in terms of revisit time and for the possibility to achieve acquisition geometries complementary to

spaceborne systems. Therefore, airborne SAR systems can meet more stringent requirements for environmental monitoring on regional or local scales compared to spaceborne ones.

The revisit time of spaceborne SAR systems, in fact, is limited by the satellites orbital parameters and is usually on the order of days or weeks, depending on the latitude and on the number of satellites belonging to the constellation. A limited revisit time poses a lower bound on the achievable temporal resolution, which represents an important constraint for some applications as it restricts the ability to track the evolution of geophysical processes as they develop over time. Areas characterised by relatively high rates of change, such as fast landslides, require appropriately short temporal baselines to reduce decorrelation and phase aliasing [10]. Airborne SAR systems can fill this gap by performing multiple acquisitions of the same area at higher temporal sampling, although the manoeuvring time necessary to repeat approximately the same trajectory over multiple passes also imposes a lower limit on the achievable temporal sampling. Furthermore, thanks to the possibility to carry multiple sensors operating at different wavelengths and polarizations [11–15], airborne SAR systems can operate in different acquisition modes and can be used to test novel SAR concepts for future spaceborne missions and for the validation of theoretical models [16].

A limiting factor to the extended and regular use of airborne SAR systems is the high cost per acquisition. Small uninhabited aerial vehicles (UAVs) and small aircraft can have an economical advantage over large aircraft but are subject to larger platform instabilities and are usually constrained in terms of weight and size of the payload (i.e. the radar system, including transmitting and receiving antennas, and the positioning measurement system).

Ground-based systems   Despite the lower coverage area compared to airborne and spaceborne systems, ground-based radar systems (real aperture and SAR), also known as terrestrial radar systems, are widely used for monitoring local-scale surface changes such as glaciers movements, rockfall, and landslides [5, 17, 18]. The typically low acquisitions cost of ground-based radars allows to perform a large number of acquisitions potentially resulting in temporal resolutions on the order of minutes or even seconds depending on the speed of the scan, thus allowing to sample also fast surface changes and non-linear deformation phenomena such as accelerating landslides [10].

Furthermore, ground-based radar systems offer an ideal acquisition geometry for steep surface slopes, such as in mountainous regions, where spaceborne and airborne SAR systems have inherent limitations due to layover and shadowing.

SAR interferometry   Interferometric SAR techniques (InSAR) are widely adopted for topographic and surface deformation mapping. The coherent nature of SAR systems, that is the ability to retain the phase information related to the two-way path length of the transmitted and received electromagnetic signals, can be leveraged to retrieve Earth's surface information [19, 20]. Specifically, differential SAR interferometry (DInSAR) exploits the phase difference between SAR images acquired at different times to retrieve surface changes of the imaged area on the order of a fraction of the electromagnetic wavelength [21–23]. Furthermore, in the absence of surface deformations, other important environmental parameters, such as soil moisture and vegetation water content variations, can be potentially measured [24–28].

Nevertheless, the high sensitivity of the interferometric techniques to small phase variations implies a high susceptibility to phase errors. For example, atmospheric changes between the acquisitions determine a variation of the signal path length from the SAR sensor to the target area and back that can mask the deformation signal of interest [29]. The atmospheric disturbance is exacerbated in the case of airborne and spaceborne SAR sensors due to the large distance from the ground. Although the atmospheric effect can be, to some extent, mitigated by using advanced DInSAR techniques such as the persistent scatterer interferometry [30–32], it is still a challenge in many applications and it is therefore the focus of ongoing research.

The most important limitation to repeat-pass interferometric SAR techniques is the temporal decorrelation, which is the loss of mutual correlation, or coherence, between the complex-valued pixels of SAR acquisition pairs relevant to the same area. The temporal decorrelation is caused by physical changes in the resolution cells occurring between different acquisitions and can severely hinder the exploitation of the interferometric phase for the retrieval of surface dynamics. Such effect is particularly critical in vegetated areas or partially vegetated areas, where a large number of scatterers are typically in constant motion and, therefore, decorrelation can occur even for acquisitions separated by short time spans. Longer electromagnetic wavelengths are more robust towards temporal decorrelation. This can be well illustrated by the following temporal coherence model [33–35]

$$\gamma_{\text{temp}} = \exp\left\{-\frac{1}{2}\left(\frac{4\pi}{\lambda}\right)^2 \sigma_r^2\right\} \tag{1.1}$$

that shows how the temporal coherence γ_{temp} decreases exponentially with the squared ratio between the standard deviation of the targets movement within the resolution cell σ_r and the radar wavelength λ. Equation 1.1 highlights that for a given value of σ_r, longer wavelengths (i.e. lower frequency bands) imply lower decorrelation. Low frequency bands, like for example P-band and L-band, can at least partially penetrate through the vegetation and are more likely to interact with the stable parts of the scatterers in the resolution cells such as tree trunks and the ground, thus retaining higher coherence.

Nevertheless, there is a trade-off between the robustness towards temporal decorrelation and the sensitivity to surface changes. In fact, if φ is the (differential) interferometric phase owed to a surface change D, it is immediate to show that the sensitivity to the surface change is inversely proportional to the radar wavelength:

$$\varphi = \frac{4\pi}{\lambda} D \implies \frac{\partial \varphi}{\partial D} = \frac{4\pi}{\lambda} \tag{1.2}$$

The capability of low frequency bands to retain higher interferometric coherence over long time spans potentially allows to perform deformation monitoring also in areas partially or completely covered by vegetation and to retrieve the geophysical parameters of interest of the imaged scene, such as soil moisture, vegetation water content, and biomass.

Many articles in literature highlight the relatively high coherence achievable with L-band SAR systems in natural areas over long time spans. A coherence of 0.2–0.4 was measured in forested areas with the DLR E-SAR airborne SAR system with a temporal baseline of 1 year [11]. In [7], image pairs from ALOS-2 with

1

temporal baselines of more than 2 years could achieve coherence high enough to reveal post-seismic surface deformations even in vegetated areas. In [36], a coherence above 0.4 was reported in vegetated areas using ALOS-2 acquisitions with 3 years of temporal baseline.

1.2 MOTIVATION

While spaceborne and airborne systems are operationally employed also at low frequency bands, the majority of ground-based radar systems work in high frequency bands such as X-band and Ku-band [37] to achieve good azimuth resolution. For ground-based radars, in fact, the latter can be expressed as [38]:

$$\delta_{az} \simeq \frac{\lambda}{2L} \cdot r \tag{1.3}$$

where δ_{az} is the azimuth resolution, r is the slant range, λ is the radar wavelength, and L is the antenna length. From Eq. 1.3 it follows that to achieve good azimuth resolutions with ground-based systems, the radar wavelength must be much smaller than the antenna length, particularly for long range distances. The limited length of the real or the synthetic antenna is an important drawback of ground-based radars, as it limits *de facto* the maximum electromagnetic wavelength that can be employed for the acquisitions.

Compared to real aperture radars, ground-based SAR (GB-SAR) systems can achieve better azimuth resolution by sliding a small antenna along a rail [39] or by performing an arc scan with the antenna mounted on a boom [40]. Nevertheless, for practical reasons the synthetic antenna is typically not longer than a few meters. To provide an idea of the requirements, considering a wavelength of 23 cm (L-band), the synthetic antenna should be 575 m long to achieve a resolution of 1 m at a distance of 5 km, while a synthetic antenna of 10 m would achieve an azimuth resolution of 57.5 m at the same range.

In order to use low frequency bands also from GB-SAR systems it is necessary to achieve longer synthetic apertures without the need to install impractically long rails. Such requirement is the basic motivation for the development of an L-band car-borne SAR system [41, 42]. By transmitting and receiving radar echoes while driving a car along a road, longer synthetic apertures can be formed compared to rail-based or arc-scanning systems and the constraint on the maximum radar wavelength can be relaxed while still achieving relatively good azimuth resolutions. Furthermore, given the availability of a sufficiently long road with unobstructed visibility of the target area, the car-borne system can theoretically achieve the full SAR azimuth resolution equal to half the length of the real antenna [1].

A car-borne SAR system shares most of the advantages common to the commercially available GB-SAR systems, such as the possibility to perform repeat-pass acquisitions with flexible temporal baselines at low cost and with acquisition geometries suited for monitoring steep slopes.

In the context of repeat-pass DInSAR applications, an additional advantage of ground-based radar systems is the possibility to perform acquisitions with small spatial baselines, which is ideal for deformation mapping. In fact, small perpendicular baselines between the acquisition entail a low sensitivity to the topography of the imaged scene and hence a small topography-related interferometric phase,

which needs to be removed when the goal is the measurement of the surface changes occurring between the acquisitions. Furthermore, small baselines also imply small geometrical decorrelation [34]. In the car-borne case it is rather easy to achieve sub-meter perpendicular interferometric baselines, which is instead challenging in the case of airborne and spaceborne SAR systems.

Therefore, a car-borne SAR system can be an additional and complementary asset to the existing systems for the monitoring of local-scale deformation phenomena, especially in natural areas that typically pose challenges to (high frequency) ground-based and to airborne/spaceborne SAR systems for the reasons outlined above.

Nevertheless, compared to rail-based GB-SAR systems, a car-borne SAR requires accurate positioning measurements necessary to perform focusing and interferometric processing, which represents a potential source of errors and an additional processing burden, as documented with regard to UAV-borne and airborne SAR applications [43–45].

The impact of positioning errors on the repeat-pass interferometric performance is one of the important aspects to investigate in the development of a car-borne SAR system, particularly in consideration of the close-range acquisition geometry along with the wide-beam antennas. Furthermore, with the goal to perform deformation monitoring in natural terrains, it is of interest to understand the interferometric performance over short-time spans measured in areas covered by vegetation and under different weather conditions in absence of ground deformation phenomena. Such analysis would then provide a reference for the decorrelation patterns that can be expected during the observation of deformation phenomena in natural areas.

1.3 STATE OF THE ART

National and international organisations worldwide are committing to the development of L-band SAR missions to address important environmental challenges such as modelling the carbon cycle through global measurements of the forests biomass [46].

After the success of the L-band missions JERS-1 (1992–1998), ALOS/PALSAR (2006–2011), and ALOS-2/PALSAR-2 (2014–present), the Japan Aerospace Exploration Agency (JAXA) is planning the deployment of ALOS-4/PALSAR-3 [47, 48], due to be launched in 2022 to ensure the continuity of Japan's goal to provide national disaster monitoring, land information, agricultural monitoring, as well as worldwide global forest mapping. The German Aerospace Center (DLR) plans to launch its two Tandem-L satellites by 2024 [49], which are foreseen to be in orbit for at least 10 years and to have a revisit time of 16 days. A joint effort of the American and the Indian space agencies NASA and ISRO will put in orbit the NISAR L/S-band SAR system by 2022, for a 3–5 years mission [50] with a revisit time of 12 days. The European Space Agency (ESA) is working on the Radar Observation System for Europe in L-band (ROSE-L) SAR system, whose launch is planned for 2028 to expand Europe's mapping capabilities with an additional and complementary wavelength to the existing C-band SAR systems on board of Sentinel-1A and Sentinel-1B. Argentina completed the deployment of its two SAOCOM satellites in 2020 [51].

Meanwhile, a number of airborne SAR systems have been operating in low frequency bands such as P-

1

and L-band, which have been successfully used in multiple campaigns and also served as technology demonstrators for the upcoming spaceborne missions [16, 52–56].

However, the availability of ground-based radar systems operating at L-band is very limited [37]. In [57] the development of a truck-mounted arc-scanning SAR systems at L-band capable of achieving an azimuth resolution equivalent to a 12.6 m linear scanning SAR was presented. A similar system was presented in [58]. A 3-D rail-based SAR with an aperture of 20 m horizontally and 1.5 m vertically operating on a wide range of frequencies (50 MHz to 20 GHz) through the use of a vector network analyzer was presented in [59] and used for the evaluation of the polarimetric backscatter response from vegetation.

Car-borne SAR systems were presented in literature as imaging or single-pass InSAR systems [60–64], but none of them works in L-band nor was used for repeat-pass DInSAR monitoring. Therefore, there is no analysis of the performance of L-band repeat-pass DInSAR observations from a car-borne SAR. The car-borne SAR system is equipped with a high-performance (navigation-grade) inertial navigation system with an embedded global navigation satellite system receiver (INS/GNSS). Such systems are commonly employed on board of airborne SAR systems for trajectory measurements as well as for navigation purpose. However, the finite accuracy of the INS/GNSS system leads to positioning errors in the trajectory data that vary within the time span of the synthetic aperture and are uncorrelated from pass to pass. Autofocus and multisquint techniques [65–68] can be useful to reduce the magnitude of such errors but they are limited by the need to achieve high interferometric coherence (multisquint) [68] and long synthetic apertures [66]. Furthermore, the correction of global offset terms requires the use of corner reflectors or phase trend removal methods. There is therefore an interest in minimizing the positioning errors independently from the radar data.

Short-term temporal decorrelation has been largely observed with GB-SAR, but at high-frequency bands [69–71]. At L-band, short-term InSAR time series analyses are available from airborne SAR systems, although generally not over extended periods of time. In [72], a coherence analysis employing multiple acquisitions over a time interval of 71 minutes was performed using data acquired by the DLR E-SAR airborne polarimetric SAR system during the BioSAR mission [54]. In [73] the authors analysed 27 interferograms spanning 2.5 hours highlighting interferometric fluctuations in agricultural area possibly linked to soil moisture changes. A polarimetric-interferometric analysis was presented in [74] using data acquired with the NASA/JPL UAVSAR systems over a period of two weeks. In view of the future ESA BIOMASS mission [75], notable experiments at L- and P-band assessing short-term decorrelation effects in forested areas over extended periods of time have been performed with a tower-based scatterometer [76, 77], where coherence dependence on the vegetation water content and the wind speed variance was observed.

1.4 RESEARCH OBJECTIVES

The main goal of this research is to assess the suitability of the L-band car-borne SAR system for monitoring natural areas via repeat-pass DInSAR.

An important aspect of repeat-pass DInSAR monitoring is the accuracy of the estimated radar trajectories both during the synthetic aperture and from pass to pass, which ultimately impacts the phase

sensitivity to changes in the mapped area.

When the positioning measurement system is based on GNSS measurements, such as for an integrated INS/GNSS system, one or more GNSS reference stations are often employed to perform differential GNSS processing to reduce the positioning errors. Since the performance of the differential GNSS techniques depend on the distance from the reference stations, the following research questions arise:

- **How much does the positioning error change in function of the distance of the radar platform from the GNSS reference station?**

- **Is the use of a GNSS reference station deployed in the vicinity of the radar platform required to achieve the desired positioning accuracy or are the available reference stations of the permanent GNSS network sufficient?**

Depending on the platform speed and the road length, the integration time of a typical car-borne SAR acquisition can be on the order of tens of seconds or minutes. Such long integration times can be problematic in terms of positioning accuracy. In fact, as a consequence of the continuously changing visibility of the GNSS satellites and the atmospheric variations affecting the one-way signal path from the satellites to the GNSS receiver, the accuracy of the integrated INS/GNSS trajectory can change over time. The positioning accuracy may therefore vary during the integration time of the synthetic aperture and from pass to pass as the temporal baseline between the acquisitions increases. The research question to investigate in this regard is therefore the following:

- **How much does the positioning error change within the time span of the synthetic aperture and from pass to pass?**

The different positioning errors experienced from pass to pass ultimately result in interferometric phase errors. The acquisition geometry of the car-borne SAR, pointing slightly up- or down-wards (side-looking with respect to the driving direction), entails large variations of look angles, which has an impact on the positioning-related phase errors. Furthermore, as the intended application is the observation of natural areas, strong topographic variations have to be expected, which also have an impact on the phase error. Therefore we are interested in observing the positioning phase errors in a typical acquisition scenario for the car-borne SAR. The relevant research question can be summarised as follows:

- **What is the variation of positioning-related interferometric (DInSAR) phase errors in the typical acquisition geometry of the car-borne SAR?**

To answer the previous questions we performed a controlled (rail-based) experiment involving simultaneous measurements of positioning and repeat-pass SAR data. Such experiment allowed us to estimate

1

the positioning errors owed to the navigation-grade INS/GNSS system and to assess their effect on the repeat-pass DInSAR phase as a function of the distance of the radar platform from different GNSS reference stations. The positioning errors were evaluated within the time-frame of single SAR acquisitions with relatively long integration times and between different passes relevant to InSAR/DInSAR acquisitions. We exploited the constrained position of the rail-based setup by combining the interferometric pairs in a way that results in a complete isolation of the interferometric phase from the tropospheric path delays affecting the radar signals. This allowed to quantify the effect of the positioning errors on the DInSAR data in a real acquisition scenario, characterised by an acquisition geometry that is typical for the car-borne system.

In a subsequent work we analysed the results of a SAR measurement campaign performed in a natural area characterised by the presence of vegetation, focusing on the interferometric performance in different land covers as a function of time. Specifically, by taking advantage of the flexible temporal baselines of the car-borne SAR, we investigated the interferometric coherence and phase variations in vegetated areas over time intervals ranging from few minutes up to 15 days.

A number of research questions were investigated in the context of this work with the intent to better understand the main drivers of coherence change over different time spans.

Primarily, we intended to observe the average coherence level achievable on different land covers, the spread of coherence within each land cover, and the coherence variation for increasing temporal baselines, in particular for vegetated areas. The relevant research questions follow:

- **What is the level of interferometric coherence achievable with the car-borne SAR system in a natural environment characterised by the presence of vegetation?**

- **How does the coherence change depending on the land cover class and as a function of time?**

- **Do longer temporal baselines, within the relatively short time span of 15 days, entail lower coherence?**

Furthermore, in a measurement campaign aimed at the identification and/or monitoring of deformation phenomena such as landslides, it is important to understand what other phenomena can determine coherence and/or phase variations in the observed areas. Weather-related events such as humidity changes, rainfall, and wind, for example, are possible sources of interferometric signals that need to be identified and possibly distinguished from deformation-related signals. The high temporal sampling achievable with the car-borne SAR system is an important asset in this context as it allows to closely observe the interferometric behaviour as the environmental changes develop in time. The research questions we aim to answer can be summarised as follows:

- **Can interferometric phase and coherence variations be linked to weather-related changes in the imaged areas such as humidity, rainfall, and wind?**

- **Do such weather-related interferometric changes appear as fading signals?**

- **Is the availability of multiple acquisitions per day beneficial to circumvent temporally localised decorrelation effects?**

- **What are the implications of such interferometric changes for repeat-pass DInSAR acquisitions for deformation monitoring?**

REFERENCES

[1] G. Franceschetti and R. Lanari, *Synthetic Aperture Radar Processing.* Electronic engineering systems series, Taylor & Francis, 1999.

[2] A. de Sherbinin, M. A. Levy, E. Zell, S. Weber, and M. Jaiteh, "Using satellite data to develop environmental indicators," *Environmental Research Letters*, vol. 9, p. 084013, Aug 2014.

[3] H. A. Zebker and R. M. Goldstein, "Topographic mapping from interferometric synthetic aperture radar observations," *Journal of Geophysical Research: Solid Earth*, vol. 91, no. B5, pp. 4993–4999, 1986.

[4] C. Colesanti, A. Ferretti, C. Prati, and F. Rocca, "Monitoring landslides and tectonic motions with the Permanent Scatterers Technique," *Engineering Geology*, vol. 68, no. 1-2, pp. 3–14, 2003.

[5] T. Strozzi, R. Caduff, U. Wegmüller, H. Raetzo, and M. Hauser, "Widespread surface subsidence measured with satellite SAR interferometry in the Swiss alpine range associated with the construction of the Gotthard base tunnel," *Remote Sensing of Environment*, vol. 190, 2017.

[6] T. Kobayashi, "Remarkable ground uplift and reverse fault ruptures for the 2013 Bohol earthquake (Mw 7.1), Philippines, revealed by SAR pixel offset analysis," *Geoscience Letters*, vol. 1, no. 1, p. 7, 2014.

[7] M. Hashimoto, "Postseismic deformation following the 2016 Kumamoto earthquake detected by ALOS-2/PALSAR-2," *Earth, Planets and Space*, vol. 72, Oct 2020.

[8] T. Nagler, H. Rott, M. Hetzenecker, K. Scharrer, E. Magnússon, D. Floricioiu, and C. Notarnicola, "Retrieval of 3D-glacier movement by high resolution X-band SAR data," in *2012 IEEE International Geoscience and Remote Sensing Symposium*, pp. 3233–3236, 2012.

[9] H. Rott, D. Floricioiu, J. Wuite, S. Scheiblauer, T. Nagler, and M. Kern, "Mass changes of outlet glaciers along the Nordensjköld Coast, northern Antarctic Peninsula, based on TanDEM-X satellite measurements," *Geophysical Research Letters*, vol. 41, no. 22, pp. 8123–8129, 2014.

[10] A. Manconi, "How phase aliasing limits systematic space-borne DInSAR monitoring and failure forecast of alpine landslides," *Engineering Geology*, vol. 287, p. 106094, 2021.

[11] A. Reigber and R. Scheiber, "Airborne differential SAR interferometry: First results at L-band," *IEEE Transactions on Geoscience and Remote Sensing*, vol. 41, no. 6 PART II, pp. 1516–1520, 2003.

[12] A. Reigber, K. Papathanassiou, M. Jger, and R. Scheiber, "First results of multispectral polarimetry and single-pass PolInSAR with the F-SAR airborne SAR instrument," in *2013 IEEE International Geoscience and Remote Sensing Symposium - IGARSS*, pp. 2305–2308, Jul 2013.

[13] S. Hensley, K. Wheeler, G. Sadowy, C. Jones, S. Shaffer, H. Zebker, T. Miller, B. Heavey, E. Chuang, R. Chao, K. Vines, K. Nishimoto, J. Prater, B. Carrico, N. Chamberlain, J. Shimada, M. Simard, B. Chapman, R. Muellerschoen, C. Le, T. Michel, G. Hamilton, D. Robison, G. Neumann, R. Meyer, P. Smith, J. Granger, P. Rosen, D. Flower, and R. Smith, "The UAVSAR instrument: Description and first results," in *2008 IEEE Radar Conference*, pp. 1–6, May 2008.

[14] S. Perna, C. Wimmer, J. Moreira, and G. Fornaro, "X-band airborne differential interferometry: Results of the OrbiSAR campaign over the Perugia area," *IEEE Trans. Geosci. Remote Sens.*, vol. 46, pp. 489–503, Feb. 2008.

[15] P. Dubois-Fernandez, O. du Plessis, D. le Coz, J. Dupas, B. Vaizan, X. Dupuis, H. Cantalloube, C. Coulombeix, C. Titin-Schnaider, P. Dreuillet, J. Boutry, J. Canny, L. Kaisersmertz, J. Peyret, P. Martineau, M. Chanteclerc, L. Pastore, and J. Bruyant, "The ONERA RAMSES SAR system," in *2002 IEEE International Geoscience and Remote Sensing Symposium*, vol. 3, pp. 1723–1725 vol.3, Jun 2002.

[16] L. Fatoyinbo, N. Pinto, M. Hofton, M. Simard, B. Blair, S. Saatchi, Y. Lou, R. Dubayah, S. Hensley, J. Armston, L. Duncanson, and M. Lavalle, "The 2016 NASA AfriSAR campaign: Airborne SAR and lidar measurements of tropical forest structure and biomass in support of future satellite missions," in *2017 IEEE International Geoscience and Remote Sensing Symposium*, pp. 4286–4287, IEEE, Jul 2017.

[17] R. Caduff, F. Schlunegger, A. Kos, and A. Wiesmann, "A review of terrestrial radar interferometry for measuring surface change in the geosciences," *Earth Surface Processes and Landforms*, vol. 40, no. 2, pp. 208–228, 2015.

[18] G. Antonello, N. Casagli, P. Farina, D. Leva, G. Nico, A. J. Sieber, and D. Tarchi, "Ground-based SAR interferometry for monitoring mass movements," *Landslides*, vol. 1, no. 1, pp. 21–28, 2004.

[19] P. A. Rosen, S. Hensley, I. R. Joughin, F. K. Li, S. N. Madsen, E. Rodriguez, and R. M. Goldstein, "Synthetic aperture radar interferometry," *Proceedings of the IEEE*, vol. 88, no. 3, pp. 333–382, 2000.

[20] R. Bamler and P. Hartl, "Synthetic aperture radar interferometry," *Inverse Problems*, vol. 14, pp. 1–54, Aug 1998.

[21] F. Gatelli, A. Monti Guamieri, F. Parizzi, P. Pasquali, C. Prati, and F. Rocca, "The wavenumber shift in SAR interferometry," *IEEE Transactions on Geoscience and Remote Sensing*, vol. 32, pp. 855–865, Jul 1994.

[22] D. Massonnet and K. L. Feigl, "Radar interferometry and its application to changes in the Earth's surface," *Reviews of Geophysics*, vol. 36, no. 4, pp. 441–500, 1998.

[23] D. Massonnet and K. L. Feigl, "Discrimination of geophysical phenomena in satellite radar interferograms," *Geophysical Research Letters*, vol. 22, pp. 1537–1540, Jun 1995.

[24] A. K. Gabriel, R. M. Goldstein, and H. A. Zebker, "Mapping small elevation changes over large areas: differential radar interferometry," *Journal of Geophysical Research*, vol. 94, no. B7, pp. 9183–9191, 1989.

[25] M. Nolan, D. Fatland, and L. Hinzman, "DInSAR measurement of soil moisture," *IEEE Transactions on Geoscience and Remote Sensing*, vol. 41, no. 12, pp. 2802–2813, 2003.

[26] F. De Zan, A. Parizzi, P. Prats-Iraola, and P. López-Dekker, "A SAR interferometric model for soil moisture," *IEEE Transactions on Geoscience and Remote Sensing*, vol. 52, no. 1, pp. 418–425, 2014.

[27] V. Brancato, F. Liebisch, and I. Hajnsek, "Impact of plant surface moisture on differential interferometric observables: A controlled electromagnetic experiment," *IEEE Transactions on Geoscience and Remote Sensing*, vol. 55, no. 7, pp. 3949–3964, 2017.

[28] I. Hajnsek and P. Prats, "Soil moisture estimation in time with D-InSAR," in *2008 IEEE International Geoscience and Remote Sensing Symposium*, vol. 3, pp. III – 546–III – 549, 2008.

[29] H. A. Zebker, P. Rosen, and S. Hensley, "Atmospheric effects in interferometric synthetic aperture radar surface deformation and topographic maps," *Journal of Geophysical Research: Solid Earth*, vol. 102, pp. 7547–7563, 1997.

[30] A. Ferretti, C. Prati, and F. Rocca, "Permanent scatterers in SAR interferometry," *Geoscience and Remote Sensing, IEEE Transactions on*, vol. 39, pp. 8–20, Jan 2001.

[31] A. Ferretti, G. Savio, R. Barzaghi, A. Borghi, S. Musazzi, F. Novali, C. Prati, and F. Rocca, "Submillimeter accuracy of InSAR time series: Experimental validation," *IEEE Transactions on Geoscience and Remote Sensing*, vol. 45, no. 5, pp. 1142–1153, 2007.

[32] C. Werner, U. Wegmüller, T. Strozzi, and A. Wiesmann, "Interferometric point target analysis for deformation mapping," in *2003 IEEE International Geoscience and Remote Sensing Symposium*, vol. 7, pp. 4362–4364 vol.7, 2003.

[33] M. Lavalle, M. Simard, and S. Hensley, "A temporal decorrelation model for polarimetric radar interferometers," *IEEE Transactions on Geoscience and Remote Sensing*, vol. 50, pp. 2880–2888, Jul 2012.

[34] H. A. Zebker and J. Villasenor, "Decorrelation in interferometric radar echoes," *IEEE Transactions on Geoscience and Remote Sensing*, vol. 30, pp. 950–959, Sep 1992.

[35] F. Rocca, "Modeling interferogram stacks," *IEEE Transactions on Geoscience and Remote Sensing*, vol. 45, pp. 3289–3299, Oct 2007.

[36] T. Abe, G. Iwahana, P. V. Efremov, A. R. Desyatkin, T. Kawamura, A. Fedorov, Y. Zhegusov, K. Yanagiya, and T. Tadono, "Surface displacement revealed by L-band InSAR analysis in the Mayya area, Central Yakutia, underlain by continuous permafrost," *Earth, Planets and Space*, vol. 72, Sep 2020.

1

[37] M. Pieraccini and L. Miccinesi, "Ground-based radar interferometry: A bibliographic review," *Remote Sensing*, vol. 11, no. 9, 2019.

[38] M. Pieraccini, "Real beam vs. synthetic aperture radar for slope monitoring," pp. 1627–1632, 01 2013.

[39] S. Placidi, A. Meta, L. Testa, and S. Rödelsperger, "Monitoring structures with FastGBSAR," in *2015 IEEE Radar Conference*, pp. 435–439, Oct 2015.

[40] M. Pieraccini and L. Miccinesi, "ArcSAR: Theory, simulations, and experimental verification," *IEEE Transactions on Microwave Theory and Techniques*, vol. 65, pp. 293–301, Jan. 2017.

[41] O. Frey, C. Werner, and R. Coscione, "Car-borne and UAV-borne mobile mapping of surface displacements with a compact repeat-pass interferometric SAR system at L-band," in *2019 IEEE International Geoscience and Remote Sensing Symposium*, pp. 274–277, Jul 2019.

[42] R. Coscione, I. Hajnsek, and O. Frey, "Trajectory uncertainty in repeat-pass SAR interferometry: A case study," in *2019 IEEE International Geoscience and Remote Sensing Symposium*, pp. 338–341, Jul 2019.

[43] S. Buckreuss, "Motion compensation for airborne SAR based on inertial data, RDM and GPS," in *1994 IEEE International Geoscience and Remote Sensing Symposium*, vol. 4, pp. 1971–1973, IEEE, 1994.

[44] G. Fornaro, "Trajectory deviations in airborne SAR: analysis and compensation," *IEEE Transactions on Aerospace and Electronic Systems*, vol. 35, pp. 997–1009, jul 1999.

[45] G. Fornaro, E. Sansosti, R. Lanari, and M. Tesauro, "Role of processing geometry in SAR raw data focusing," *IEEE Transactions on Aerospace and Electronic Systems*, vol. 38, pp. 441–454, Apr 2002.

[46] T. Le Toan, S. Quegan, I. Woodward, M. Lomas, N. Delbart, and G. Picard, "Relating radar remote sensing of biomass to modelling of forest carbon budgets," *Climatic Change*, vol. 67, pp. 379–402, Dec 2004.

[47] S. H. Miura, Y. Kankaku, T. Motohka, K. Yamamoto, and S. Suzuki, "ALOS-4 current status," in *Sensors, Systems, and Next-Generation Satellites XXIII* (S. P. Neeck, P. Martimort, and T. Kimura, eds.), vol. 11151, pp. 25 – 30, International Society for Optics and Photonics, SPIE, 2019.

[48] T. Motohka, Y. Kankaku, S. Miura, and S. Suzuki, "Alos-4 L-band SAR mission and observation," in *2019 IEEE International Geoscience and Remote Sensing Symposium*, pp. 5271–5273, Jul 2019.

[49] A. Moreira, M. Bachmann, W. Balzer, D. B. Tridon, E. Diedrich, T. Fritz, C. Grigorov, R. Kahle, G. Krieger, I. Hajnsek, S. Huber, H. Jörg, P. Klenk, M. Lachaise, M. Maier, E. Maurer, K. Papathanassiou, A. Parizzi, P. Prats, J. Reimann, M. Rodriguez, B. Schättler, M. Schwinger, D. Schulze, U. Steinbrecher, M. Villano, M. Younis, F. De Zan, M. Zink, and M. Zonno, "Tandem-L: Project status and main findings of the phase B1 study," in *2018 IEEE International Geoscience and Remote Sensing Symposium*, pp. 8667–8670, Jul 2018.

[50] P. Rosen, S. Hensley, S. Shaffer, W. Edelstein, Y. Kim, R. Kumar, T. Misra, R. Bhan, R. Satish, and R. Sagi, "An update on the NASA-ISRO dual-frequency DBF SAR (nisar) mission," in *2016 IEEE International Geoscience and Remote Sensing Symposium*, pp. 2106–2108, Jul 2016.

[51] Y. Roa, P. Rosell, A. Solarte, L. Euillades, F. Carballo, S. García, and P. Euillades, "First assessment of the interferometric capabilities of SAOCOM-1A: New results over the Domuyo volcano, Neuquén Argentina," *Journal of South American Earth Sciences*, vol. 106, p. 102882, 2021.

[52] A. Reigber, R. Scheiber, M. Jager, P. Prats-Iraola, I. Hajnsek, T. Jagdhuber, K. P. Papathanassiou, M. Nannini, E. Aguilera, S. Baumgartner, R. Horn, A. Nottensteiner, and A. Moreira, "Very-high-resolution airborne synthetic aperture radar imaging: Signal processing and applications," *Proceedings of the IEEE*, vol. 101, pp. 759–783, Mar. 2013.

[53] I. Hajnsek, F. Kugler, S.-K. Lee, and K. P. Papathanassiou, "Tropical-forest-parameter estimation by means of Pol-InSAR: The INDREX-II campaign," *IEEE Transactions on Geoscience and Remote Sensing*, vol. 47, pp. 481–493, Feb 2009.

[54] I. Hajnsek, R. Scheiber, M. Keller, R. Horn, S. Lee, L. Ulander, A. Gustavsson, G. Sandberg, T. Le Toan, S. Tebaldini, A. M. Guarnieri, and F. Rocca, "Biosar 2008: Final report," tech. rep., Nov 2009.

[55] M. Simard and M. Denbina, "An assessment of temporal decorrelation compensation methods for forest canopy height estimation using airborne L-band same-day repeat-pass polarimetric SAR interferometry," *IEEE Journal of Selected Topics in Applied Earth Observations and Remote Sensing*, vol. 11, no. 1, pp. 95–111, 2018.

[56] M. Simard, S. Hensley, M. Lavalle, R. Dubayah, N. Pinto, and M. Hofton, "An empirical assessment of temporal decorrelation using the uninhabited aerial vehicle synthetic aperture radar over forested landscapes," *Remote Sensing*, vol. 4, no. 4, pp. 975–986, 2012.

[57] H. Lee, J.-H. Lee, K.-E. Kim, N.-H. Sung, and S.-J. Cho, "Development of a truck-mounted arc-scanning synthetic aperture radar," *IEEE Transactions on Geoscience and Remote Sensing*, vol. 52, pp. 2773–2779, May 2014.

[58] D. Garmatyuk and R. Narayanan, "Ultra-wideband continuous-wave random noise arc-SAR," *IEEE Transactions on Geoscience and Remote Sensing*, vol. 40, pp. 2543–2552, Dec 2002.

[59] Z.-S. Zhou, W.-M. Boerner, and M. Sato, "Development of a ground-based polarimetric broadband SAR system for noninvasive ground-truth validation in vegetation monitoring," *IEEE Transactions on Geoscience and Remote Sensing*, vol. 42, pp. 1803–1810, Sep. 2004.

[60] Y. Yamaguchi, M. Sengoku, and S. Motooka, "Using a van-mounted FM-CW radar to detect corner-reflector road-boundary markers," *IEEE Transactions on Instrumentation and Measurement*, vol. 45, no. 4, pp. 793–799, 1996.

[61] O. Frey, C. L. Werner, U. Wegmüller, A. Wiesmann, D. Henke, and C. Magnard, "A car-borne SAR and InSAR experiment," in *2013 IEEE International Geoscience and Remote Sensing Symposium*, pp. 93–96, IEEE, Jul 2013.

[62] V. Androsov, S. Vityazev, A. Kharin, and V. Vityazev, "An approach to autofocus in car-borne radar imaging systems," in *2018 IEEE East-West Design Test Symposium (EWDTS)*, pp. 1–4, 2018.

[63] D. Valuyskiy, S. Vityazev, and V. Vityazev, "Resolution improvement in ground-mapping car-borne radar imaging systems," in *2019 IEEE International Conference on Imaging Systems and Techniques (IST)*, pp. 1–5, 2019.

[64] D.-H. Jung and S.-O. Park, "Ku-band car-borne FMCW stripmap synthetic aperture radar," in *2017 International Symposium on Antennas and Propagation (ISAP)*, pp. 1–2, Oct 2017.

[65] P. Decroix, X. Neyt, and M. Acheroy, "Trade-off between motion measurement accuracy and autofocus capabilities in airborne SAR motion compensation," in *2nd Microwave and Radar Week in Poland - International Radar Symposium, IRS 2006, Proceedings*, 2006.

[66] K. A. C. de Macedo, R. Scheiber, and A. Moreira, "An autofocus approach for residual motion errors with application to airborne repeat-pass SAR interferometry," *IEEE Transactions on Geoscience and Remote Sensing*, vol. 46, pp. 3151–3162, Oct 2008.

[67] P. Prats and J. J. Mallorqui, "Estimation of azimuth phase undulations with multisquint processing in airborne interferometric SAR images," *IEEE Transactions on Geoscience and Remote Sensing*, vol. 41, no. 6 PART II, pp. 1530–1533, 2003.

[68] P. Prats, R. Scheiber, A. Reigher, C. Andres, and R. Horn, "Estimation of the surface velocity field of the Aletsch glacier using multibaseline airborne SAR interferometry," *IEEE Transactions on Geoscience and Remote Sensing*, vol. 47, no. 2, pp. 419–430, 2009.

[69] A. Monti-Guarnieri, M. Manzoni, D. Giudici, A. Recchia, and S. Tebaldini, "Vegetated target decorrelation in SAR and interferometry: Models, simulation, and performance evaluation," *Remote Sensing*, vol. 12, no. 16, 2020.

[70] M. Lort, A. Aguasca, C. López-Martínez, and X. Fabregas, "Impact of wind-induced scatterers motion on GB-SAR imaging," *IEEE Journal of Selected Topics in Applied Earth Observations and Remote Sensing*, vol. 11, pp. 3757–3768, Oct 2018.

[71] L. Pipia, A. Aguasca, X. Fabregas, J. Mallorqui, and C. Lopez-Martinez, "Temporal decorrelation in polarimetric differential interferometry using a ground-based SAR sensor," in *2005 IEEE International Geoscience and Remote Sensing Symposium*, vol. 6, pp. 4108–4111, 2005.

[72] W. Li, E. Chen, Z. Li, W. Zhang, and H. Li, "Temporal decorrelation on airborne repeat pass P-, L-band T-SAR in boreal forest," in *2016 IEEE International Geoscience and Remote Sensing Symposium (IGARSS)*, pp. 5–8, Jul 2016.

[73] P. Prats, A. Reigber, J. J. Mallorqui, R. Scheiber, and A. Moreira, "Estimation of the temporal evolution of the deformation using airborne differential SAR interferometry," *IEEE Transactions on Geoscience and Remote Sensing*, vol. 46, no. 4, pp. 1065–1078, 2008.

[74] S. Hensley, T. Michel, J. Van Zyl, R. Muellerschoen, B. Chapman, S. Oveisgharan, Z. S. Haddad, T. Jackson, and I. Mladenova, "Effect of soil moisture on polarimetric-interferometric repeat pass observations by UAVSAR during 2010 Canadian soil moisture campaign," in *2011 IEEE International Geoscience and Remote Sensing Symposium*, pp. 1063–1066, 2011.

[75] T. Le Toan, S. Quegan, M. Davidson, H. Balzter, P. Paillou, K. Papathanassiou, S. Plummer, F. Rocca, S. Saatchi, H. Shugart, and L. Ulander, "The BIOMASS mission: Mapping global forest biomass to better understand the terrestrial carbon cycle," *Remote Sensing of Environment*, vol. 115, no. 11, pp. 2850–2860, 2011. DESDynI VEG-3D Special Issue.

[76] A. Hamadi, L. Villard, P. Borderies, C. Albinet, T. Koleck, and T. Le Toan, "Comparative analysis of temporal decorrelation at P-band and low L-band frequencies using a tower-based scatterometer over a tropical forest," *IEEE Geoscience and Remote Sensing Letters*, vol. 14, pp. 1918–1922, Nov 2017.

[77] S. E. I. Essebtey, L. Villard, P. Borderies, T. Koleck, B. Burban, and T. Le Toan, "Comparative study of temporal decorrelation at P, L and C-bands: First insights from the Tropiscat-2 experiment," in *2020 Mediterranean and Middle-East Geoscience and Remote Sensing Symposium (M2GARSS)*, pp. 246–249, Mar 2020.

2

EXPERIMENTAL SETUP AND PROCESSING

2.1 MEASUREMENT SETUP

The car-borne SAR system, shown in Fig. 2.1, is composed of an L-band radar system, four planar L-band antennas (three receiving and one transmitting in the present setup), a GNSS antenna, and the INS/GNSS system.

(a) Car-borne SAR system overview

(b) INS/GNSS system

(c) Radar main module (bottom) and battery pack (top)

Figure 2.1: Car-borne SAR system comprising one transmitting antenna, three receiving antennas, one GNSS antenna, and the INS/GNSS system rigidly mounted on the aluminium rack on the roof of the vehicle. The L-band radar main module (transceiver and computer) is hosted inside the car and connected via coaxial cables to the L-band patch antennas.

2

Type	FMCW L-band
Frequency range	1.2 – 1.4 GHz (used 1.325 GHz)
Chirp bandwidth	50 – 200 Mhz (used 100 MHz)
Chirp length	250 μs – 8 ms
Transmit power	10 W (used 5 W)
Transmit channels	2 (used 1)
Receive channels	4 (used 3)
Dimensions (L ×W×H)	40.6 cm× 33 cm ×17.4 cm
Weight	7.65 kg

Table 2.1: Radar system specifications

The antennas and the INS/GNSS system are mounted on an rigid aluminium rack fastened to the rooftop of the car. The main module of the L-band radar (comprising the transceiver and the internal computer) is hosted inside the car and connected to the antennas via coaxial cables. A battery pack is employed to power the radar and the INS/GNSS systems. The GNSS antenna is connected to the GNSS receiver (enclosed inside the INS frame) via a coaxial cable.

Radar system   The radar antennas are dual linearly polarized patch antennas with a 3 dB beamwidth of approximately 40° × 40° (azimuth × elevation), a front to back ratio of about 20dB, and power rating of 10 W.

The radar system is a frequency modulated continuous wave (FMCW) system[1] that operates in the frequency band 1.2–1.4 GHz (L-band) and has a maximum bandwidth of 200 Mhz. The central frequency used for the acquisitions is 1.325 GHz, corresponding to a wavelength of 22.6 cm, with a bandwidth limited to 100 MHz to meet the frequency spectrum allocation requirements in Switzerland. The main characteristics of the radar are summarised in Table 2.1. Four receive channels and two alternating transmit channels allow to operate in different acquisition modes. Fully polarimetric acquisitions can be performed using two receive and two transmit channels connected to the H and V antenna ports. Along-track and across-track single-pass interferometric acquisitions can be performed with one transmitting antenna and three receiving antennas of which two aligned along the driving direction and two aligned across the driving direction (see Fig. 2.1). A combination of interferometric and polarimetric acquisition schemes can be also implemented. Received signals are converted to baseband using a dechirp-on-receive scheme, digitized via a 14-bit field programmable gate array (FPGA), and finally stored on a solid state disk (SSD). The radar is controlled by an integrated Linux-based computer [1].

Positioning measurement system   The positioning measurement system used to retrieve precise trajectory information of the car during the repeated SAR acquisitions consists of a navigation-grade INS (iMAR iNAV-RQH-10018) with an integrated dual-frequency and dual-constellation receiver (GPS and GLONASS). The INS is composed of three ring laser gyroscopes and three servo accelerometers for dynamic motion measurements (orientation, attitude, and acceleration) along with a data processor. The internal data acquisition rate of the INS is 1800 Hz, which is then converted to a 300 Hz output data

---

[1]Radar system provided by Gamma Remote Sensing AG.

Accelerometer	3 servo accelerometers	Gyroscope	3 ring laser gyro
Accelerometer bias	< 25 μ**g**	Gyro bias	< 0.002°/h
Accelerometer resolution	< 5 m**g**	Gyro resolution	<0.001°/s
Spectral noise	< 8 μ**g**/$\sqrt{\text{Hz}}$	Angular random walk	< 0.0015°/$\sqrt{\text{h}}$
Attitude accuracy (unaided)	<0.01°	True heading	< 0.025°/ cos(*lat*)
Position accuracy (unaided)	0.6 nmi/h(~1.1 km/h)	GNSS receiver	Novatel (GPS, GLONASS)
Inertial data rate	300 Hz	GNSS data rate	1 Hz

Table 2.2: Technical data of the navigation-grade inertial navigation system (INS) iMAR iNAV-RQH-10018. Gyro and accelerometer biases are responsible for the inertial drift and define the performance of the system in absence of external aids (e.g. during a GNSS outage). **g** $\simeq$ 9.81m/s^2.

rate after correcting for coning and sculling motion [2], while the GNSS data is logged at a rate of 1 Hz. The acquired data is stored on an internal solid-state flash-disk. The INS/GNSS system is rigidly mounted on the aluminium rack on the car (strapdown configuration [2]), close to the radar antennas. The characteristics of the INS/GNSS system are summarised in Table 2.2.

Figure 2.2: Local GNSS reference station employed for differential GNSS processing (PPK).

Additionally, a static GNSS receiver (Fig. 2.2) is employed as local reference station for differential GNSS processing. The GNSS receiver is a dual-frequency and dual-constellation (GPS and GLONASS) Trimble R7 system. Data logging rate is 1–20 Hz (used 1 Hz). The antenna of the local GNSS reference station is an L-band Trimble Zephyr Geodetic model 2. It is characterised by a small cross-section to reduce wind loading, by the presence of an integrated ground plane to reduce multiplath interference, and by a high signal gain (50dB) to allow for high quality satellite signal tracking also at low elevation angles.

2.2 Measurement campaigns

2.2.1 Stein glacier campaign

In July 2018 we performed a series of rail-based SAR and positioning measurements to assess the positioning errors caused by the finite accuracy of the INS/GNSS system and the relevant interferometric phase errors in a real acquisition scenario characterised by an acquisition geometry similar to that typically achieved from the car-borne SAR system. The employed procedures and the results of the analysis relevant to such campaign are reported in Chapter 3.

The rail-based system is shown in Fig. 2.3. The target of the radar measurements was the Stein glacier, in central Switzerland (Canton of Bern) during which we performed almost 3 hours of repeat-pass SAR measurements for a total of 58 acquisitions.
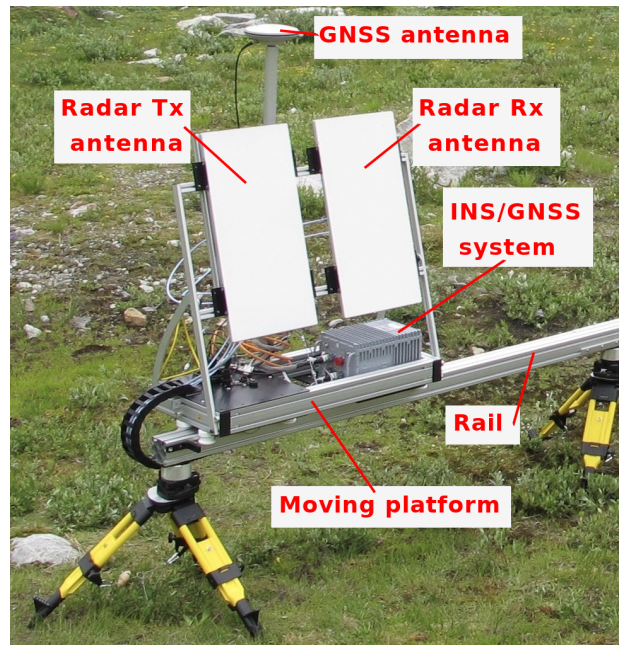

Figure 2.3: Experimental setup for positioning error analysis using the L-band SAR system and the INS/GNSS navigation system (iMAR iNAV-RQH-10018) deployed in a rail-based configuration with a length of the synthetic aperture of 10m.

The rail is made of six 2m-long aluminium profiles supported by tripods. A platform controlled by a motor synchronized with the radar transmissions slides forth and back along the rail at a speed of about 40 cm/s on a quasi-linear trajectory. The radar antennas, the INS/GNSS system, and the GNSS antenna are rigidly mounted on the moving platform. The employed INS/GNSS and radar systems are the same ones used for the car-borne SAR acquisitions. The two patch antennas (one transmitting and one receiving) are similar to the ones used in the car-borne setup with the sole difference of a smaller elevation beamwidth: 40° × 20° (azimuth × elevation).

2.2.2 Weesen/Amden campaign

In November 2018 we performed a series of car-borne SAR acquisitions in the area of Weesen/Amden, in Northeastern Switzerland (Canton of St. Gallen).
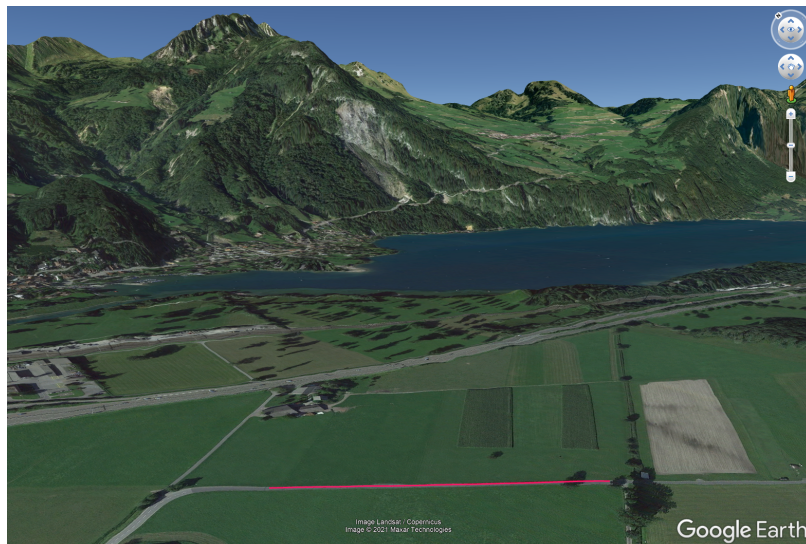

Figure 2.4: Google Earth view of the car-borne acquisition site in Weesen/Amden (Northeastern Switzerland, Canton of St. Gallen). The car-borne repeat-pass trajectories are visible at the bottom of the image.

A large dataset comprising tens of acquisitions per day with different modes in terms of polarizations, chirp lengths, and integration time was collected. In Chapter 4 the results of the interferometric analysis of a subset of the available dataset (chirp length of 2 ms and 40 seconds of integration time) are reported. Specifically, a set of 32 HH polarized acquisitions relevant to Nov. 05–08 and Nov. 19–20, and 39 VV polarized acquisitions relevant to Nov. 14–15 and Nov. 19–20 were used in the analyses of Chapter 4.

Fig. 2.4 shows the measurement area and the trajectories of the car during the SAR acquisitions. The length of the synthetic aperture is about 250 meters and the road is roughly straight. Although the road allows to achieve a SAR length of 500 m, for the analyses reported in Chapter 4 we used half of the maximum synthetic aperture length to reduce possible errors due to the presence of a small building in the middle of the road, behind the trees in the lower-right part of Fig. 2.4, causing a brief occultation of the transmitted and received radar signals. Moreover, in the same position the road presents a uneven surface that caused the car to bump during the acquisitions, with consequent damping oscillations of the car, which could be the source of unwanted residual effects in the positioning and in the radar data.

2.3 POSITIONING PROCESSING

An INS can perform very accurate and high-rate acceleration and angular rate measurements from which position and orientation are calculated via single and double mathematical integration over the time window of interest. However, accelerometers and gyroscopes composing the INS are affected by systematic and random biases that accumulate over time as a consequence of the integration. Such accumulation error (also known as integration drift) causes the measured position and orientation to
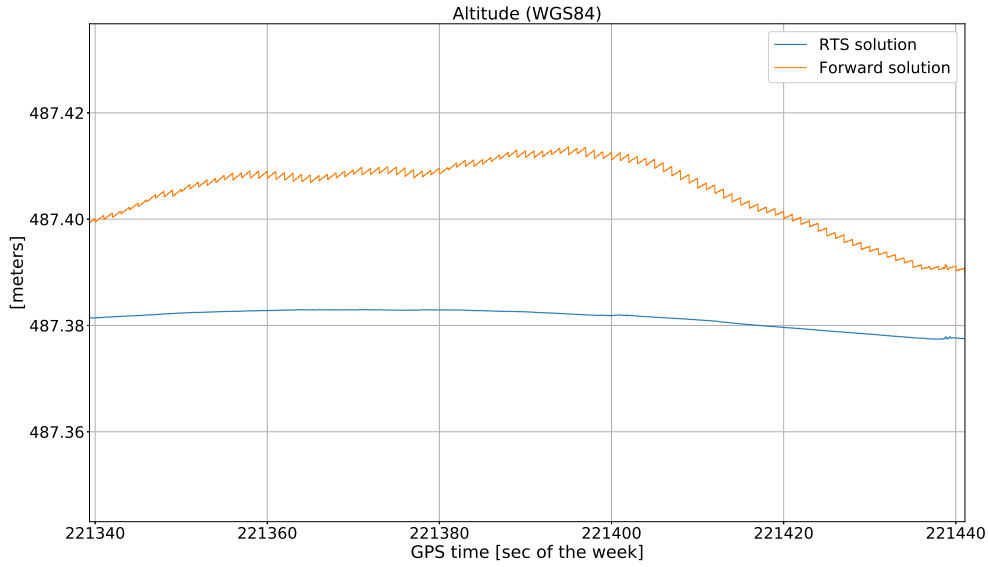
Figure 2.5: Combined INS/GNSS positioning solutions (altitude only) measured during a standstill period. The forward solution (i.e. after the first EKF) shows a peak-to-peak variation of about 2 cm in 100 seconds while the RTS solution (i.e. after the second EKF) shows altitude variations 4 times smaller (below 0.5 cm). The effect of the INS integration drift occurring between two GNSS updates (at a rate of 1 Hz) is visible on the forward solution as a sawtooth-like error signal with a magnitude of 1 mm. After RTS smoothing residual oscillations are below 0.3 mm.

drift away from their actual values, leading to positioning errors up to kilometres per hour even for high-performance systems [3]. For example, as reported in Table 2.2, the position uncertainty of the navigation-grade INS, that is the class of INS used for airborne navigation, used on board of the carborne SAR system increases of more than 1 km per hour as a consequence of the integration drift.

In a combined INS/GNSS system the integration drift is compensated by regularly updating the INS data with the GNSS measurements (with an update interval of one second or longer), which are more stable over long time spans [2, 3]. However, GNSS measurements are affected by different error sources, the most notable of which is the atmospheric (ionospheric and tropospheric) refraction of the GNSS signals that can lead to positioning errors in the order of tens of meters if not properly compensated [4–6]. Differential GNSS techniques exploit the spatial correlation of the atmosphere to reduce its impact. The position of the platform is calculated with respect to a second GNSS receiver (reference station) with known and fixed coordinates [7]. When the two receivers are in the vicinity, the errors common to both receivers, such as the correlated part of the atmospheric error as well as satellites and receivers clock biases, cancel out by calculating single and double differences of the GNSS observables. Thus, the performance of differential GNSS processing methods worsen when the distance between the GNSS receiver on the moving platform and the reference station increases, since the atmospheric error affecting the signal at the two receivers becomes uncorrelated.

In the present work, we use a differential GNSS technique called post-processed kinematic (PPK) based on carrier-phase GNSS observables. PPK data at 1 Hz rate is then used to regularly update the INS measurements to compensate for the integration drift [2, 8].

The integration of INS and post-processed GNSS measurements is performed through a loosely-coupled extended Kalman filter (EKF), which is a widely used recursive algorithm for the estimation of the state of a system through the evaluation of the covariance matrix of multiple measurements corrupted by noise [2, 9]. Additionally, the INS/GNSS integration scheme employed in the present work includes a Rauch-Tung-Striebel (RTS) smoother [8, 10], which is an additional extended Kalman filter that operates backwards (i.e. in reverse time) while using the covariance error matrix calculated during the forward step as initial value for the recursive estimation.

An issue of the combined INS/GNSS approach summarised above, which can be problematic for SAR processing in particular with lower-grade INS systems, is the sawtooth-like error signal resulting in the output trajectory in consequence of the INS integration drift occurring between two GNSS updates. Such effect is shown in Fig. 2.5 using the data of the car-borne INS/GNSS system measured during a standstill period. Fig. 2.5 also shows the large reduction of the sawtooth signal as well as the increased position stability achieved with the RTS smoother.

The position, velocity, and attitude data of the platform calculated after INS/GNSS integration are relevant to a reference point inside the INS. Through the knowledge of the lever-arms between the INS reference point and the radar antenna phase centre (APC), position and orientation over time of the latter during the SAR acquisition can be calculated as required to perform SAR focusing. Finally, since in the specific case the RTS output has a sampling rate of 20 Hz, we upsample it to the radar PRF to retrieve the position, velocity, and attitude data of the APC relevant to each radar echo.

2.4 RADAR PROCESSING

SAR focusing algorithms operating in frequency domain typically assume linear or circular platform trajectories, in which case the positioning data typically provided by the INS/GNSS system is used to compensate for the deviations of the SAR platform from the nominal path [11–23] using aperture- and topography-dependent motion compensation algorithms [20, 21, 24–28]. Such approach is commonly adopted for airborne SAR system [15, 29] but might be inadequate for platforms characterised by highly non-linear trajectories such as ground vehicles or low-altitude and light-weight aircraft [30–33].

On the other hand, in the case of SAR focusing based on time-domain backprojection (TDBP) no assumption needs to be made about the shape of the synthetic aperture and the measured SAR sensor trajectory is directly used to build the time-varying 3-D matched filter applied to the raw data. Therefore, TDBP algorithms are best suited to focus data acquired from agile platforms that can potentially have highly non-linear sensor trajectories [30, 34–36].

In the specific case, to focus the SAR data acquired with the car-borne SAR system we use a modified TDBP algorithm adapted to the FMCW case, which accounts for the non validity of the start and stop approximation [31, 36, 37]. The employed algorithm exploits parallelization on a graphics processing unit to reduce the typically high computational cost of the TDBP processing [34, 38, 39].

A characteristic of the TDPB is that it requires the distance of the APC from the scattering centre of the resolution cell. For this purpose, we use the knowledge of the APC trajectory (calculated as reported

in Section 2.3) and a digital elevation model (DEM) of the imaged area[2]. A direct consequence of the combined use of positioning and DEM information is that the TDBP produces focused images that are automatically geocoded and coregistered, and for which aperture- and topography-dependent effects are inherently compensated [32, 33, 38, 40]. Furthermore, the focused data does not contain the phase term related to the topography of the imaged scene [32] and, therefore, the Hermitian product of two complex images focused via TDBP directly results in a differential interferogram, in which the only interferometric topographic phase components are related to positioning and DEM errors.

Since the actual scattering centre of the resolution cell is unknown, in practice the physical centre of the cell is considered to calculate the time-varying distance of the sensor's APC from the resolution cell. This approximation entails a phase error in the focused image that is proportional to the difference between the actual APC-to-target distance and the one used in the TDBP matched filter [30], and is smaller at higher resolution. Nevertheless, in practice, the TDBP algorithm works on a pixel-by-pixel basis, where a pixel usually corresponds to an area smaller than the resolution cell due to the applied oversampling, which is a necessary step for interferometric application in order to avoid aliasing when combining SAR image pairs [41]. Therefore, the phase error in each pixel is smaller for higher oversampling factors. In our case, the applied oversampling is defined by the grid spacing of the DEM (posting), which is homogeneous throughout the area and tailored to the dimension of the resolution cell in close range. Since the azimuth resolution worsens with the increase of the range distance, the oversampling factor increases and the phase error decreases.

REFERENCES

[1] O. Frey, C. Werner, and R. Coscione, "Car-borne and UAV-borne mobile mapping of surface displacements with a compact repeat-pass interferometric SAR system at L-band," in *2019 IEEE International Geoscience and Remote Sensing Symposium*, pp. 274–277, Jul 2019.

[2] D. Titterton and J. L. Weston, *Strapdown Inertial Navigation Technology*. Radar, Sonar and Navigation, Institution of Engineering and Technology, 2004.

[3] P. D. Groves, *Principles of GNSS, inertial, and multisensor integrated navigation systems*. GNSS technology and applications series, Boston: Artech House, 2nd ed. ed., 2013.

[4] P. Georgiadou and A. Kleusberg, "On the effect of ionospheric delay on geodetic relative GPS positioning," *Journal of Geodesy*, vol. 13, no. 1, pp. 1–8, 1988.

[5] H. Nahavandchi and A. Soltanpour, "Local ionospheric modelling of GPS code and carrier phase observations," *Survey Review*, vol. 40, no. 309, pp. 271–284, 2008.

[6] T. Hobiger and N. Jakowski, *Atmospheric Signal Propagation*, pp. 165–193. Springer International Publishing, 2017.

[7] B. Hofmann-Wellenhof, H. Lichtenegger, and E. Wasle, *GNSS — Global Navigation Satellite Systems: GPS, GLONASS, Galileo, and more*. Springer Vienna, 2008.

---

[2]SwissAlti-3D DEM provided by the Swiss Federal Office of Environment swisstopo.

[8] E. L. Hinüber, C. Reimer, T. Schneider, and M. Stock, "INS/GNSS integration for aerobatic flight applications and aircraft motion surveying," *Sensors (Switzerland)*, vol. 17, p. 941, Apr 2017.

[9] R. E. Kalman, "A New Approach to Linear Filtering and Prediction Problems," *Journal of Basic Engineering*, vol. 82, no. 1, p. 35, 1960.

[10] H. E. Rauch, C. T. Striebel, and F. Tung, "Maximum likelihood estimates of linear dynamic systems," *AIAA Journal*, vol. 3, pp. 1445–1450, Aug 1965.

[11] C. Cafforio, C. Prati, and F. Rocca, "SAR data focusing using seismic migration techniques," *IEEE Transactions on Aerospace and Electronic Systems*, vol. 27, pp. 194–207, Mar. 1991.

[12] R. Bamler, "A comparison of range-doppler and wavenumber domain SAR focusing algorithms," *IEEE Transactions on Geoscience and Remote Sensing*, vol. 30, no. 4, pp. 706–713, 1992.

[13] R. K. Raney, H. Runge, R. Bamler, I. G. Cumming, and F. H. Wong, "Precision SAR processing using chirp scaling," *IEEE Transactions on Geoscience and Remote Sensing*, vol. 32, no. 4, pp. 786–799, 1994.

[14] A. Moreira, J. Mittermayer, and R. Scheiber, "Extended chirp scaling algorithm for air- and spaceborne SAR data processing in stripmap and ScanSAR imaging modes," *IEEE Transactions on Geoscience and Remote Sensing*, vol. 34, no. 5, pp. 1123–1136, 1996.

[15] A. Reigber, R. Scheiber, M. Jager, P. Prats-Iraola, I. Hajnsek, T. Jagdhuber, K. P. Papathanassiou, M. Nannini, E. Aguilera, S. Baumgartner, R. Horn, A. Nottensteiner, and A. Moreira, "Very-high-resolution airborne synthetic aperture radar imaging: Signal processing and applications," *Proceedings of the IEEE*, vol. 101, pp. 759–783, Mar. 2013.

[16] J. R. Moreira, "A new method of aircraft motion error extraction from radar raw data for real time motion compensation," *IEEE Transactions on Geoscience and Remote Sensing*, 1990.

[17] S. Buckreuss, "Motion compensation for airborne SAR based on inertial data, RDM and GPS," in *1994 IEEE International Geoscience and Remote Sensing Symposium*, vol. 4, pp. 1971–1973, IEEE, 1994.

[18] A. Moreira and Y. Huang, "Airborne SAR processing of highly squinted data using a chirp scaling approach with integrated motion compensation," *IEEE Transactions on Geoscience and Remote Sensing*, vol. 32, no. 5, pp. 1029–1040, 1994.

[19] D. R. Stevens, I. G. Cumming, and A. L. Gray, "Options for airborne interferometric SAR motion compensation," *IEEE Transactions on Geoscience and Remote Sensing*, vol. 33, no. 2, pp. 409–420, 1995.

[20] A. Potsis, A. Reigber, J. Mittermayer, A. Moreira, and N. Uzunoglou, "Sub-aperture algorithm for motion compensation improvement in wide-beam SAR data processing," *Electronics Letters*, vol. 37, no. 23, pp. 1405–1407, 2001.

2

[21] S. N. Madsen, "Motion compensation for ultra wide band SAR," in *2001 IEEE International Geoscience and Remote Sensing Symposium*, vol. 3, pp. 1–3, 2001.

[22] A. Reigber, A. Potsis, E. Alivizatos, N. Uzunoglu, and A. Moreira, "Wavenumber domain SAR focusing with integrated motion compensation," in *2003 IEEE International Geoscience and Remote Sensing Symposium*, vol. 3, pp. 1465–1467, 2003.

[23] A. Reigber, E. Alivizatos, A. Potsis, and A. Moreira, "Extended wavenumber-domain synthetic aperture radar focusing with integrated motion compensation," *IEE Proceedings - Radar, Sonar and Navigation*, vol. 153, no. 3, pp. 301–310, 2006.

[24] A. Reigber and K. Papathanassiou, "Correction of residual motion errors in airborne repeat-pass interferometry," in *2001 IEEE International Geoscience and Remote Sensing Symposium*, vol. 7, pp. 3077–3079, IEEE, 2001.

[25] K. A. C. de Macedo and R. Scheiber, "Precise topography- and aperture-dependent motion compensation for airborne SAR," *IEEE Geoscience and Remote Sensing Letters*, vol. 2, no. 2, pp. 172–176, 2005.

[26] P. Prats, A. Reigber, and J. J. Mallorqui, "Topography-dependent motion compensation for repeat-pass interferometric SAR systems," *IEEE Geoscience and Remote Sensing Letters*, vol. 2, pp. 206–210, Apr 2005.

[27] P. Prats, K. A. C. de Macedo, A. Reigber, R. Scheiber, and J. J. Mallorqui, "Comparison of topography- and aperture-dependent motion compensation algorithms for airborne SAR," *IEEE Geoscience and Remote Sensing Letters*, vol. 4, no. 3, pp. 349–353, 2007.

[28] K. A. C. de Macedo, C. Wimmer, T. L. M. Barreto, D. Lubeck, J. R. Moreira, L. M. L. Rabaco, and W. J. De Oliveira, "Long-term airborne DInSAR measurements at X- and P-bands: A case study on the application of surveying geohazard threats to pipelines," *IEEE Journal of Selected Topics in Applied Earth Observations and Remote Sensing*, vol. 5, no. 3, pp. 990–1005, 2012.

[29] R. Scheiber, "A three-step phase correction approach for airborne repeat-pass interferometric SAR data," in *2003 IEEE International Geoscience and Remote Sensing Symposium*, vol. 2, pp. 1190–1192, July 2003.

[30] M. I. Duersch and D. G. Long, "Analysis of time-domain back-projection for stripmap SAR," *International Journal of Remote Sensing*, vol. 36, no. 8, pp. 2010–2036, 2015.

[31] A. Ribalta, "Time-domain reconstruction algorithms for FMCW-SAR," *IEEE Geoscience and Remote Sensing Letters*, vol. 8, pp. 396–400, May 2011.

[32] N. Cao, H. Lee, E. Zaugg, R. Shrestha, W. E. Carter, C. Glennie, Z. Lu, and H. Yu, "Estimation of residual motion errors in airborne SAR interferometry based on time-domain backprojection and multisquint techniques," *IEEE Transactions on Geoscience and Remote Sensing*, vol. 56, pp. 2397–2407, Apr 2018.

[33] E. Yigit, S. Demirci, C. Ozdemir, and M. Tekbas, "Short-range ground-based synthetic aperture radar imaging: performance comparison between frequency-wavenumber migration and back-projection algorithms," *Journal of Applied Remote Sensing*, vol. 7, no. 1, pp. 1–13, 2013.

[34] O. Frey, C. Magnard, M. Rüegg, and E. Meier, "Focusing of airborne synthetic aperture radar data from highly nonlinear flight tracks," *IEEE Transactions on Geoscience and Remote Sensing*, vol. 47, pp. 1844–1858, Jun 2009.

[35] L. Ulander, H. Hellsten, and G. Stenstrom, "Synthetic-aperture radar processing using fast factorized back-projection," *IEEE Transactions on Aerospace and Electronic Systems*, vol. 39, pp. 760–776, Jul 2003.

[36] E. C. Zaugg and D. G. Long, "Generalized frequency scaling and backprojection for LFM-CW SAR processing," *IEEE Transactions on Geoscience and Remote Sensing*, vol. 53, pp. 3600–3614, Jul 2015.

[37] O. Frey, C. L. Werner, and U. Wegmüller, "GPU-based parallelized time-domain back-projection processing for agile SAR platforms," in *2014 IEEE International Geoscience and Remote Sensing Symposium*, pp. 1132–1135, 2014.

[38] O. Frey, E. H. Meier, and D. R. Nüesch, "Processing SAR data of rugged terrain by time-domain back-projection," in *SAR Image Analysis, Modeling, and Techniques VII* (F. Posa, ed.), vol. 5980, pp. 71 – 79, International Society for Optics and Photonics, SPIE, Oct 2005.

[39] O. Frey, C. Magnard, M. Rüegg, and E. Meier, "Non-linear SAR data processing by time-domain back-projection," *Synthetic Aperture Radar (EUSAR)*, pp. 1–4, 2008.

[40] O. Frey, E. Meier, and D. Nüesch, "A study on integrated SAR processing and geocoding by means of time-domain backprojection," in *Proc. Int. Radar Symp.*, 2005.

[41] R. F. Hanssen, *Radar Interferometry: Data Interpretation and Error Analysis*. Remote Sensing and Digital Image Processing, Springer, 2001.

2

3

IMPACT OF POSITIONING ERRORS IN CAR-BORNE REPEAT-PASS SAR INTERFEROMETRY: A CASE STUDY

3.1 INTRODUCTION

Accurate knowledge of the trajectory and the orientation of the radar antenna during the SAR data acquisition is a critical requirement for SAR image focusing and interferometric processing [1–4]. Especially for agile platforms such as small aircraft, unmanned aerial vehicles (UAV), or road vehicles, which can have highly non-linear sensor trajectories [5–7], accurate positioning data along with topographic information of the mapped area are needed to build the spatially varying matched filter for azimuth focusing and to produce well-focused motion-compensated SAR and InSAR data based on the 3-D geometry of the mapped scene [5, 8–11].

Commonly, position and attitude of the radar platform are measured with positioning measurement systems mounted on board such as integrated inertial navigation systems and global navigation satellite systems (INS/GNSS) [12–14]. The finite accuracy of the positioning measurement system causes a mismatch between the actual sensor trajectory and the measured one, often referred in literature as residual motion errors, that lead to residual phase errors in the focusing and in the interferometric products [9–11, 15–18]. Since positioning errors are subject to temporal variations, these errors are especially critical for repeat-pass (differential) interferometric applications.

For agile SAR platforms, factors such as non-linear sensor trajectories, long integration time, large variation of look angles and range distances [19, 20], and strong topographic variations, further increase the impact of positioning errors on the interferometric phase and derived products [4, 10, 18, 21]. Moreover, in case of strong topographic variations, DEM height errors lead to different range shifts of the target location as a function of the look angle [22].

In a combined INS/GNSS system the changing GNSS satellite visibility and the atmospheric variations influence the positioning performance. Therefore, the longer the integration time, the higher the probability of experiencing relative positioning errors along the synthetic aperture as a consequence of the time-varying performance of the INS/GNSS system.

To assess the positioning errors in a real acquisition scenario, multiple positioning measurements should be performed while the radar platform repeats exactly the same trajectory over multiple passes [23, 24]. Since a sufficiently accurate repetition of the sensor trajectory is unfeasible with a car-borne, UAV-borne, or airborne system, we performed a controlled repeat-pass experiment with the L-band SAR mounted on a rail additionally equipped with a navigation-grade INS/GNSS system [25].

The main error sources of an INS system are the biases affecting its accelerometers and gyroscopes, which lead to significant position drifts over time due to the integration necessary to obtain relative positions and attitude information from accelerations and angular velocities. Such position drift is usually compensated by combining INS and GNSS positioning measurements, generally performed using a Kalman filter [14, 26]. Therefore, keeping the errors of the GNSS positioning as small as possible is critical to minimise time-varying positioning errors.

Error sources of GNSS-based positioning include satellite orbit and clock errors, tropospheric and iono-spheric path delays, and, potentially, multipath effects [27–30]. Differential GNSS processing such as real-time kinematic (RTK) or post-processing kinematic (PPK) with respect to a reference GNSS station allows to compensate for the first three error sources. RTK/PPK allows to exploit the spatial correlation of the tropospheric path delay in the GNSS signals and reduce its impact [30], although the performance of the correction worsen with the distance between the GNSS rover and the reference station (the closer, the better) [31, 32]. Additionally, since the ionosphere is a dispersive medium, by using dual-frequency GNSS systems a ionosphere-free solution can be obtained.

Networks of permanent and continuously operating GNSS ground reference stations are available in many countries worldwide, like CORS (continuously operating reference station) in America, EPN (EU-REF permanent network) in Europe, and AGNES (automated GNSS network for Switzerland) in Switzerland [33–35] but their mean distance from the SAR platform is fixed once the measurement target area is established. Portable GNSS reference stations can be deployed in the vicinity of the SAR platform in an effort to further reduce the tropospheric disturbance, although such option adds additional burden in terms of measurement setup and processing.

In view of operational repeat-pass DInSAR measurements from agile platforms, it is relevant to understand whether using one or more reference stations of the available network of permanent GNSS receivers is sufficient or whether the local GNSS reference stations is required to guarantee high positioning accuracy and, hence, low residual phase errors. Although residual motion compensation [15, 20, 36–40] and autofocusing techniques [8, 41–43] can, to some extent, reduce the impact of positioning errors, achieving accurate trajectory estimates in the first instance is desirable to minimise aperture- and topography-dependent phase trends.

The aim of this work is to quantify the trajectory errors measured with a high-performance (navigation-grade) INS/GNSS system for different GNSS reference station setups and to analyze their impact on the interferometric phase in a real acquisition scenario relevant to the acquisition geometry of the car-borne SAR system [44–46]. In particular, we investigate the effect of the trajectory errors on repeat-pass SAR acquisitions as a function of the distance of the radar platform from different GNSS reference stations. We set up a rail-based SAR and INS/GNSS measurement system [25] to guarantee an almost exact

Figure 3.1: Photograph of the Stein Glacier acquired during the measurement campaign in July 2018.

repeatability of the platform trajectories over multiple passes and, thus, to quantify the time-varying positioning errors with respect to the actual platform trajectory. We compare the positioning solutions obtained with the closest reference stations of the AGNES network and with a local non-permanent GNSS receiver deployed few meters away from the SAR platform, and analyse the PPK-only and the integrated INS/PPK positioning solutions.

The residual positioning errors are evaluated during the time-frame of single SAR acquisitions with long integration times and between different passes relevant to InSAR/DInSAR acquisitions. The rail-based setup allows to quantify the effect of positioning errors on the DInSAR data by isolating the residual phase errors from the troposphere-induced interferometric phase.

3.2 METHODS

3.2.1 Experimental measurement setup

To collect high-quality repeat-pass positioning and attitude data and guarantee an almost perfect repeatability of the platform trajectory in a controlled setup, we performed repeat-pass SAR data acquisitions along a fixed 10 m-long rail additionally equipped with a navigation-grade INS/GNSS system (see Fig. 2.3). The constrained position of the sensor trajectory along the rail allows to evaluate the accuracy (trueness and precision [23]) of the estimated trajectory with respect to the nominal path of the platform.

The measurement setup includes the following elements (see Fig. 2.3).

- A platform moving along a 10m-long rail at a speed of about 40 cm/s controlled by a motor synchronised with the radar transmissions. Start and end positions of the platform are the same for every pass.

- A linearly frequency modulated continuous wave (FMCW) system operating at L-band with a bandwidth of 100 MHz and a chirp length of 2 ms (PRF 500MHz) [46].

- Two radar antennas (one transmitting and one receiving) rigidly mounted to the moving platform, with 3 dB beamwidth of 40° in azimuth and 20° in elevation.
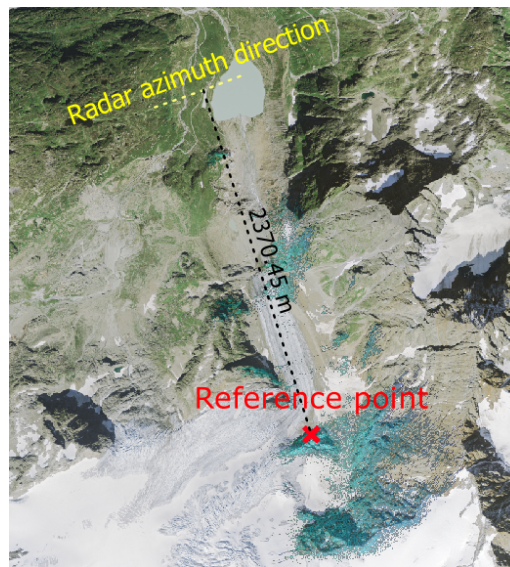
Figure 3.2: Map of the imaged area (Stein glacier) located at a distance from the radar ranging roughly from 400 m to 3200 m for a total area of 2.6 km². The straight dotted yellow line indicates the direction of the rail (the length is exaggerated to highlight the azimuth direction of the radar). North is upwards. The interferometric reference point (red cross) is set on an exposed rock at a distance of about 2370 m from the rail midpoint.

- A INS/GNSS system and a GNSS antenna fixed to the platform moving along the rail (strapdown configuration [14]). Table 2.2 summarises the specifications of the INS/GNSS system.

- A non-permanent stationary GNSS receiver (Fig. 2.2) steadily mounted few meters away from the rail (in the following indicated as "local reference station") used as reference station for GNSS differential processing.

- Two permanent, continuously operating, stationary GNSS reference stations of the AGNES network [35], located at different heights at a distance of about 20 km from the rail (see Table 3.1), used for GNSS differential processing.

The moving GNSS receiver—called "rover" in the GNSS jargon—and the reference stations are dual-frequency and multi-constellation (GPS and GLONASS).

The radar acquisitions were performed at every pass during the forward movement of the platform. Position, velocity, and attitude measurements were performed for the entire duration of the campaign at a data acquisition rate of 1 Hz for the GNSS and 300 Hz for the INS.

The measurement campaign took place in July 2018 in the Bernese Alps, where radar acquisitions of the Steingletscher (Stein glacier) were performed from a distance of about 3200 m from the target area (Figs. 3.1 and 3.2). The height difference between the radar position and the top part of the mapped area is about 1200 m, corresponding to a variation of look angles between near range and far range of 20°.

Station name	OALP	HABG	Local
Description	Permanent station of the AGNES network: Oberalppass	Permanent station of the AGNES network: Hasliberg	Stationary non-permanent (portable) receiver.
Antenna type	TRM59800.00	TRM59800.00	TRM77971.00
Baseline	~20 km	~20 km	< 10 m
Height	2139.53 m	1147.97 m	2000.37 m

Table 3.1: GNSS stations used as reference for carrier-phase differential GNSS processing (PPK).

Reference station	Carrier	Legend entry
local station	L1	local_L1
local station	L1+L2	local_L1L2
AGNES: OALP	L1+L2	OALP
AGNES: OALP + HABG	L1+L2	2agnes
AGNES: HABG	L1+L2	HABG

Table 3.2: GNSS reference stations and carrier signals used for PPK processing. The column "legend entry" indicates the name used in the plots for the PPK and the related RTS positioning solutions.

3.2.2 Trajectory estimation via GNSS and INS data processing

To retrieve the trajectory information required to focus the SAR data, inertial and GNSS data were integrated in post-processing to reduce the accumulation error affecting accelerometers and gyroscopes of the INS. First, for each reference station, the GNSS measurements were processed using the carrier-phase differential GNSS technique known as post-processed kinematic (PPK) [30, 47], which provides the time-series of platform positions for the entire duration of the measurement campaign. The PPK solutions were then integrated with the inertial data via a loosely-coupled extended Kalman filter followed by a Rauch-Tung-Striebel (RTS) smoother [26, 48, 49]. In the following we refer to the integrated and smoothed INS/PPK positioning solutions, which were then used for SAR focusing, as RTS solutions[1].

The PPK positioning solutions and, hence, the related RTS ones were independently calculated for each reference station indicated in Table 3.1:

- Two solutions are based on the local reference station located less than 10 m away from the rover using single-frequency and dual-frequency processing, respectively. The coordinates of the local reference station were calculated via static carrier-phase differential processing using one of the AGNES stations as reference, specifically the one with the lower altitude difference with respect to the rover (the OALP station of Table 3.1).

- One solution is based on the "OALP" AGNES reference station (dual-frequency).

- One solution is based on the "HABG" AGNES reference station (dual-frequency).

- One solution is based on both the OALP and the HABG AGNES stations used at the same time (dual-frequency).

---

[1]PPK processing performed with the commercial software Novatel GrafNAV 8.70. Kalman filter and RTS smoother used for INS/PPK integration provided by iMAR Navigation GmbH.

In the case of the AGNES reference stations, dual-frequency processing proved necessary to reduce the ionospheric effect on the received data and obtain integer carrier-phase ambiguity solutions [30, 50]. A processing elevation mask of 15° was used to exclude highly attenuated signals transmitted from satellites visible at low-elevation angles and to reduce multipath.

To calculate the nominal radar trajectory, we retrieved each trajectory relevant to the radar acquisitions from the single-frequency local RTS solution (local_L1), for a total of 58 trajectories that were then averaged together. The average trajectory is a good approximation of the actual shape of the rail that, given its length and the mounting system based on tripods, slightly deviates in altitude from a perfectly linear trajectory. By averaging the available trajectories, we exploited the redundancy of the repeat-pass positioning data offered by the constrained position of the moving platform. The repeated trajectories are separated by a temporal baseline of at least 2 minutes for an overall time window of more than 2 hours and are, therefore, mostly uncorrelated [51, 52]. Hence, the standard deviation of the average trajectory is at least one order of magnitude lower than the individual trajectories.

3.2.3 Radar processing and "self-interferograms"

Together with a digital elevation model (DEM) of the mapped area, the integrated RTS trajectories were used for SAR focusing via time-domain back-projection (TDBP) [53–55]. The TDBP focusing algorithm can be used for any non-linear trajectory [6, 56] and produces motion compensated, coregistered, and geocoded SLCs. Since in TDBP the topographic phase is removed by means of the DEM and the trajectory information, the interferometric combination of two focused images automatically produces a differential interferogram [18, 57].

Nevertheless, as for other focusing algorithms, the correctness of the focusing is limited by the accuracy of the positioning system (INS/GNSS) [22]. Due to trajectory estimation errors, different from pass to pass, the interferometric phase contains residual phase components originating from the presence of a baseline error that varies with range and azimuth. The trajectory errors, and hence the residual phase, depend on the distance to the reference station used for differential GNSS processing.

To show the effect of trajectory errors on the differential interferometric phase for different GNSS setups we exploited the inherent zero spatial baseline of the rail-based system. Specifically, first we performed TDBP focusing of the raw radar data, acquired from the rail-based system, using the nominal sensor trajectory and the different RTS trajectories, namely the trajectories based on the local reference station and the ones based on the vertically closer AGNES reference station (indicated as local_L1 and OALP in Table 3.2, respectively). Then, we created a set of differential interferograms using the data focused with the nominal trajectory as primary and the data focused with each RTS trajectory as secondary. We refer to this non-standard interferometric product as "self-interferograms".

A simple model for the self-interferograms can be derived from the repeat-pass DInSAR phase

$$\varphi_{DInSAR} = \varphi_{\text{def}} + \varphi_{\text{pos}} + \varphi_{\text{tropo}} + \varphi_{\text{DEM}} + \varphi_{\text{noise}} \tag{3.1}$$

where φ_{def} is the deformation signal of interest, φ_{pos} is the residual phase due to positioning errors,

φ_{tropo} is the tropospheric path delay (also known as atmospheric phase screen), φ_{DEM} is the residual phase due to DEM errors, and φ_{noise} includes thermal noise and other unmodeled noise sources.

Since the self-interferograms are generated from image pairs relevant to the same raw data, the temporal baseline is zero and both the deformation and the tropospheric phase components cancel out in the interferogram ($\varphi_{\text{def}} = \varphi_{\text{tropo}} = 0$). Therefore, only the effect of baseline and DEM errors affect the phase of the self-interferogram φ_{self}:

$$\varphi_{\text{self}} = \varphi_{\text{pos}} + \varphi_{\text{DEM}} + \varphi_{\text{noise}} \tag{3.2}$$

Note that such experiment involving the creation of self-interferograms is only possible with systems physically constrained in two dimensions, such as the rail-based one, equipped with a positioning system, which is usually not necessary for rail-based systems [58–60]. The same radar and INS/GNSS systems are employed on the car-borne SAR.

In addition to the self-interferograms, canonical repeat-pass differential interferograms were also created using the nominal trajectory, the RTS local_L1 trajectories, and the RTS OALP trajectories, respectively.

Regarding the resolution of the rail-based interferograms, the slant-range resolution is defined by the radar bandwidth while the azimuth resolution depends on the range and the rail length, that is

$$\Delta_{rg} = \frac{c}{2B_W} \tag{3.3}$$

$$\Delta_{az} = \frac{\lambda}{2L} r \tag{3.4}$$

where L is the length of the synthetic aperture that can be obtained on the rail, λ is the radar wavelength, r is the slant range, and B_W is the chirp bandwidth. As it is typical for a rail-based SAR system [58–60], whose length is usually smaller than the azimuth extension of the radar footprint on the scene, the resolution is not constant with the range. With $L = 10$ m, $\lambda = 22.6$ cm, and r between 400 m and 3.2 km, the azimuth resolution varies between 4.5 m and 35 m from near-range to far-range, while the range resolution is 1.5 m for a bandwidth of $B_W = 100 MHz$. The DEM posting is 1 m and a multilooking windows of 35×35 pixels was applied.

3.2.4 Sensitivity analysis

In this section, a sensitivity analysis of the interferometric phase to baseline errors is reported. For a generic target, the interferometric phase φ is related to the range difference δr measured between two SAR acquisitions [61, 62]:

$$\varphi = \frac{4\pi}{\lambda} \delta r \tag{3.5}$$

In this case only the geometric component of the interferometric phase is taken into account. From the geometry depicted in Fig. 3.3 the following equation is obtained using the law of cosines:

$$(r + \delta r)^2 = r^2 + B^2 - 2rB\sin(\theta - \alpha_B) \tag{3.6}$$

where r is the slant range, θ is the target look angle, B is the baseline length, and α_B is the baseline tilt angle.
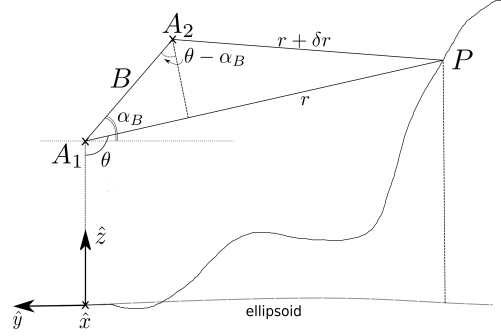

Figure 3.3: Acquisition geometry of the car-borne SAR systems. A1 and A2 indicate the antenna positions for two different passes. B is the baseline length, α_B is the baseline tilt angle, θ is the look angle, r is the range distance, δr is the range difference between the two passes. The geometry is also valid for the rail-based experimental setup (with $B = 0$).

Substituting Eq. (3.6) in Eq. (3.5), it follows:

$$\varphi = \frac{4\pi}{\lambda}(r + \delta r - r) = \frac{4\pi}{\lambda}\left(\sqrt{r^2 + B^2 - 2rB\sin(\theta - \alpha_B)} - r\right) \tag{3.7}$$

Using the error propagation formula truncated to the first order [63], the phase error due to baseline and roll errors is given by:

$$\sigma_\varphi^2 \simeq \left(\frac{\partial\varphi}{\partial B}\right)^2 \sigma_B^2 + \left(\frac{\partial\varphi}{\partial\alpha_B}\right)^2 \sigma_{\alpha_B}^2 \tag{3.8}$$

where σ_φ^2, σ_B^2, and $\sigma_{\alpha_B}^2$ are the variance of the phase, the baseline length, and the baseline tilt angle, respectively.

From Eq. (3.7) the first derivatives of the phase with respect to the baseline length and the tilt angle are:

$$\begin{aligned}
\frac{\partial\varphi}{\partial B} &= \frac{4\pi}{\lambda}\frac{B - r\sin(\theta - \alpha_B)}{\sqrt{r^2 + B^2 - 2rB\sin(\theta - \alpha_B)}} \\
\frac{\partial\varphi}{\partial\alpha_B} &= \frac{4\pi}{\lambda}\frac{Br\cos(\theta - \alpha_B)}{\sqrt{r^2 + B^2 - 2rB\sin(\theta - \alpha_B)}}
\end{aligned} \tag{3.9}$$

Substituting Eq. (3.9) in Eq. (3.8), and considering alternatively the baseline length error and the baseline tilt angle error, it follows:

(a) $\alpha_B = 0°$, $\sigma_{\alpha_B} = 0$

(b) $\alpha_B = 90°$, $\sigma_{\alpha_B} = 0$

(c) $\alpha_B = 0°$, $\sigma_B = 0$
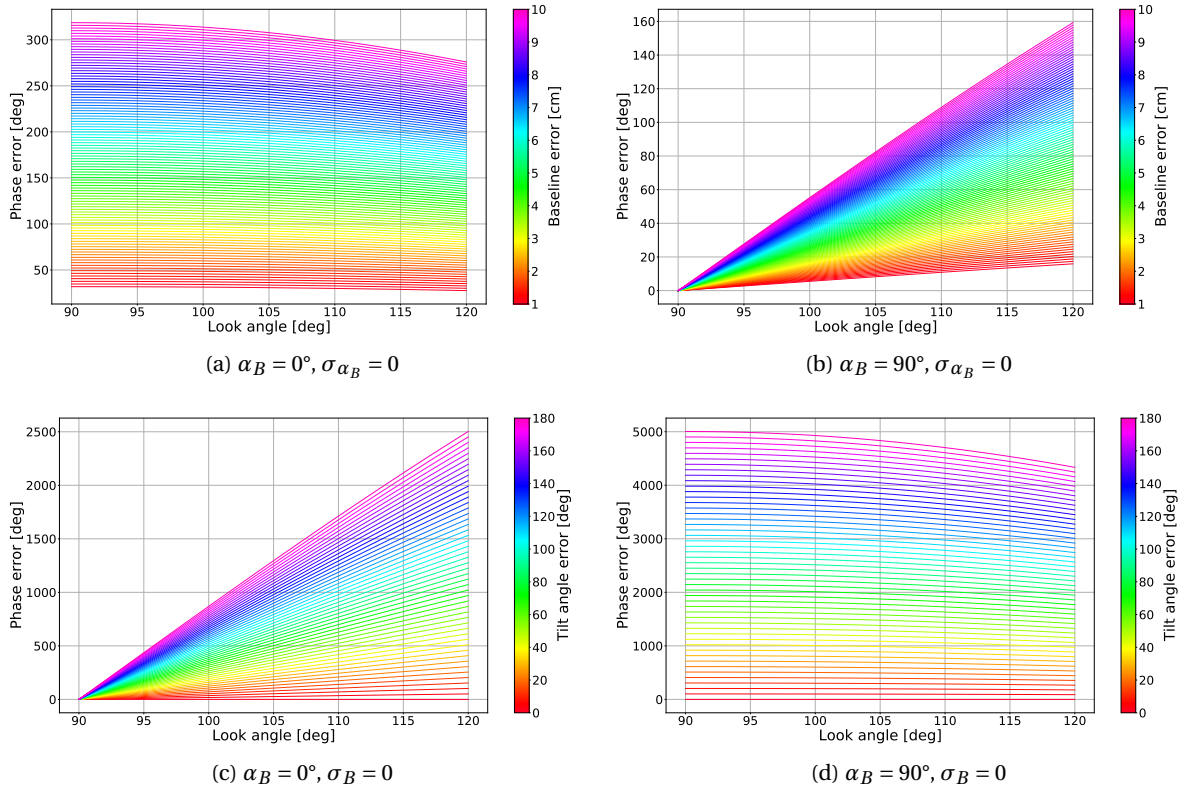
(d) $\alpha_B = 90°$, $\sigma_B = 0$

Figure 3.4: Absolute interferometric phase error vs. the look angle for different baseline length errors and baseline tilt angle errors. Range distance $r = 2000$ m. Nominal baseline $B = 0.5$ m. α_B is the nominal baseline tilt angle. σ_{α_B} is the baseline tilt angle error. σ_B is the baseline error.

$$\sigma_\varphi|_{\sigma_{\alpha_B}=0} \simeq \frac{4\pi}{\lambda} \left| \frac{B - r\sin(\theta - \alpha_B)}{\sqrt{r^2 + B^2 - 2rB\sin(\theta - \alpha_B)}} \right| \sigma_B$$

$$\sigma_\varphi|_{\sigma_B=0} \simeq \frac{4\pi}{\lambda} \left| \frac{Br\cos(\theta - \alpha_B)}{\sqrt{r^2 + B^2 - 2rB\sin(\theta - \alpha_B)}} \right| \sigma_{\alpha_B}$$

(3.10)

Eqs. (3.10) are plotted in Fig. 3.4 as a function of the look angle for different baseline errors and tilt angle errors. The nominal baseline is $B = 0.5$ m, while the nominal tilt angle α_B is either 0° or 90°. to simulate an horizontal baseline and a vertical baseline, respectively. Note that the tilt angle error σ_{α_B} is zero if the nominal baseline is zero but can lead to very large phase errors even for small baselines, depending on the look angle.

In practice, especially in DInSAR applications, the interferometric phase is always calculated with respect to a (stable) reference point located in the imaged area and therefore only the relative phase error is of interest. The latter is zero on the reference point and increases for points located away from the reference as the look angle and the baseline error vary, leading to potential errors up 50°–100°. Note that, in practice, the baseline error may vary along the azimuth as a consequence of the time-varying nature of the positioning errors, which is particularly relevant in the case of long integration times, causing differing phase trends [64].

Although the plots in Fig. 3.4 are reported for a fixed range distance ($r = 2000\,$m), due to the small nominal baseline, which is typical for car-borne SAR acquisitions, the variation of the phase error with the slant range is minimal and mostly occurs in close range. This can be shown by using the plane wave (or parallel waves) approximation [61], valid for $\delta r \ll r$ and $B \ll r$, for which Eq. (3.7) becomes:

$$\varphi_{\text{pwa}} \simeq -\frac{4\pi}{\lambda} B \sin\left(\theta - \alpha_B\right) \tag{3.11}$$

Using (3.11), the phase derivatives in (3.9) become:

$$\begin{aligned} \frac{\partial \varphi_{\text{pwa}}}{\partial B} &= -\frac{4\pi}{\lambda} \sin\left(\theta - \alpha_B\right) \\ \frac{\partial \varphi_{\text{pwa}}}{\partial \alpha_B} &= \frac{4\pi}{\lambda} B \cos\left(\theta - \alpha_B\right) \end{aligned} \tag{3.12}$$

showing that there is no direct dependence from the range distance of the phase sensitivity to baseline errors. Note, however, that the look angle θ varies with range due to the topographic height changes and to the side-looking geometry of the SAR [65]. In presence of strong topographic changes, large variations of look angles can occur, especially in close range, resulting in significant relative phase errors in function of the baseline errors.

To verify in which range of values (relevant for a car-borne acquisition scenario) the plane wave approximation holds, let us consider the approximation error ϵ_φ [61]:

$$\epsilon_\varphi = \varphi - \varphi_{\text{pwa}} = \frac{4\pi}{\lambda} \sqrt{r^2 + B^2 - 2rB\sin\left(\theta - \alpha_B\right)} - r + B\sin\left(\theta - \alpha_B\right) \tag{3.13}$$

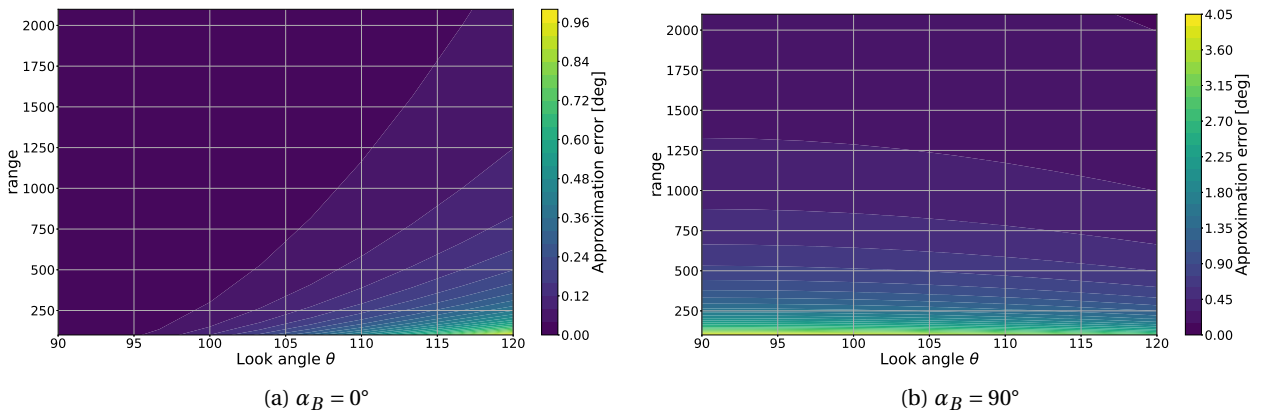(a) $\alpha_B = 0°$ (b) $\alpha_B = 90°$

Figure 3.5: Phase approximation error owed to the plane wave approximation (see Eq. (3.13)) with varying look angles and range distances (indicated in degrees and in meters, respectively), for two different values of the nominal baseline tilt angle α_B. Nominal baseline $B = 0.5\,$m.

Eq. (3.13) is plotted in Fig. 3.5 for a nominal baseline of $B = 0.5\,$m and shows that the approximation error ϵ_φ is below few degrees for range distances of 100 m and rapidly decreases for larger distances, thus indicating the validity of the plane wave approximation in most range values of interest given the small baseline length.

3.3 RESULTS

In this section, we present the results of the rail-based INS/GNSS and InSAR test measurements, high-lighting the positioning errors within the time-span of the synthetic aperture and between repeated SAR acquisitions assessed for different configurations: AGNES and local reference stations, PPK-only, and integrated INS/PPK data. Table 3.2 reports the nomenclature used in the plots for the different cases.
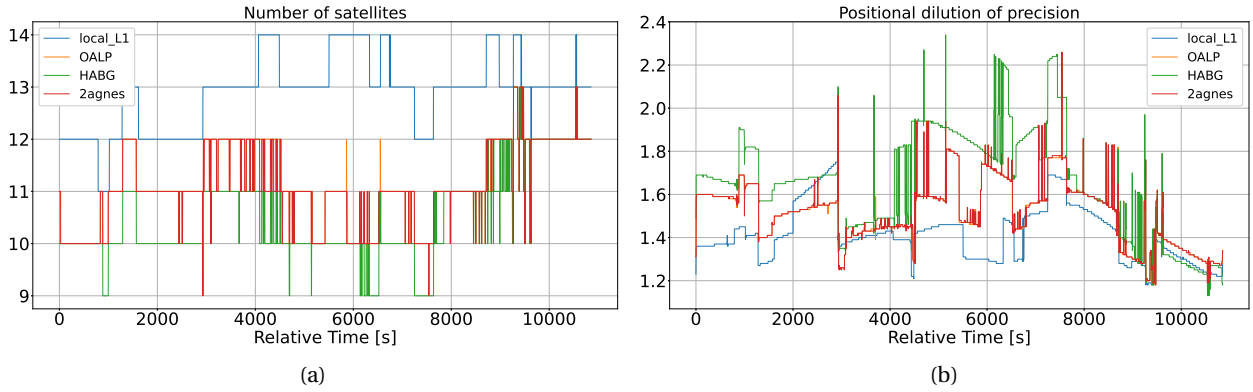

Figure 3.6: (a): number of GPS and GLONASS satellites visible at the same time from the rover and the indicated reference station (the local_L1L2 case is the same as local_L1, hence not shown). The number of satellites is above the recommended values in all cases, with the local reference station showing a slightly higher number. (b): positional dilution of precision (PDOP), which is an indication of the relative geometrical configuration between receivers and satellites. Lower values indicate better performance. All solutions present a good value for the PDOP with the local one showing better results.
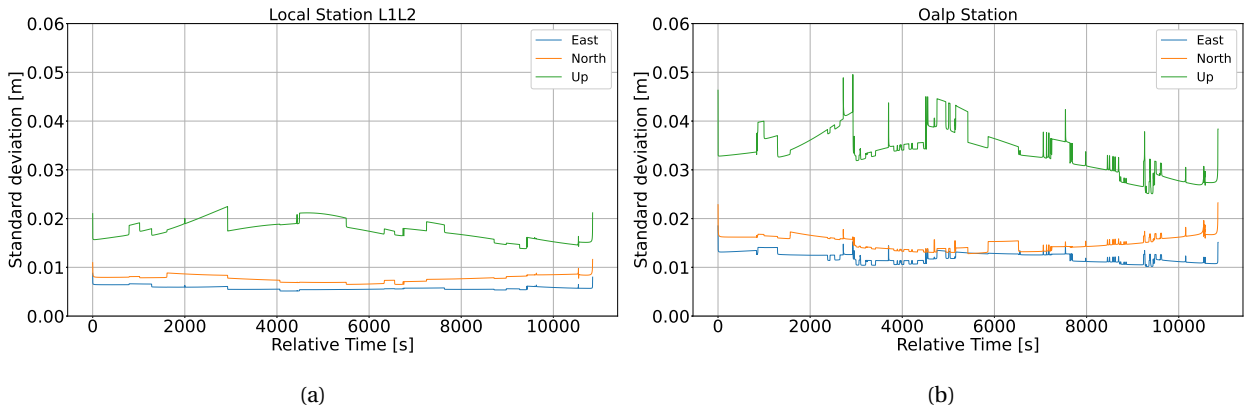
Figure 3.7: Estimated GNSS position standard deviation in East North Up coordinates of the dual-frequency PPK positioning solutions obtained using the local reference station ((a): local_L1L2) and a remote reference station of the permanent AGNES network ((b): OALP).

Fig. 3.6a shows the number of GPS and GLONASS satellites simultaneously visible from the rover moving along the rail and each reference station. For all solutions, the number of satellites is well above the minimum number required to perform differential GNSS processing (5 satellites for dual-constellation

3
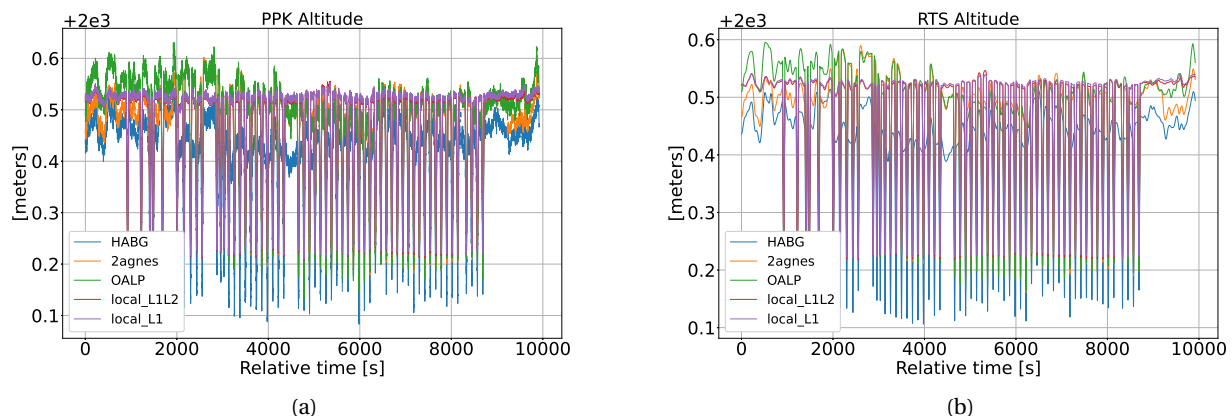
Figure 3.8: Altitude time-series (WGS84) of the repeated passes of the platform along the rail for a time span of about 3 hours, including standstill periods at the beginning and at the end. Positioning solutions obtained with the local and the AGNES reference stations (see Table 3.2) as well as PPK-only (a) and the integrated RTS (b) solutions are shown. The repeated passes of the platform along the rail are indicated by the altitude variation of about 30 cm with respect to the standstill position.

GNSS). Figure 3.6b reports the positional dilution of precision (PDOP), which is an indication of the relative geometrical configuration between ground receivers and satellites. The PDOP value is below 2.4 for each reference station indicating good satellites visibility [30, 47].

The estimated position standard deviation is shown in Fig. 3.7 for the dual-frequency PPK solutions obtained with the local reference station (local_L1L2) and the closest AGNES reference station (OALP), respectively, and is roughly two times for the latter compared to the former. The standard deviation of the vertical component is worse compared to the horizontal components, as it is usually the case for GNSS data [31].

Fig. 3.8 shows the time-series of the rover altitude of the PPK-only and the RTS positioning solutions obtained with the different GNSS reference stations, during a time interval of almost 3 hours. The repeated passes of the platform along the rail are indicated by the 30 cm altitude variations with respect to the standstill position (located at an altitude of about 2000.53 m). Standstill epochs are visible at the beginning and at the end of the measurements. The solutions obtained with the local reference station (both single-frequency and dual-frequency ones) show a better repeatability of the altitude over the multiple passes and the standstill periods. On the other hand, decimeter-level time-varying undulations are visible in the positioning solutions obtained with the remote AGNES reference stations.

Fig. 3.9 shows the boxplots of each PPK-only and the related RTS positioning solutions computed during the static epochs at the beginning and at the end of the campaign for a total time of 30 minutes (from relative time 0 s to 800 s and from about 9000 s to 10000 s in Fig. 3.8) when the platform stands still in the same position and, hence, any position variation can be directly recognised as error. The better accuracy of the positioning solutions obtained with the local reference station (both single-frequency and dual-frequency) compared to the ones obtained with the remote reference stations is clearly visible. The OALP solutions (both PPK and RTS) show a median value comparable to the local_L1L2 ones but
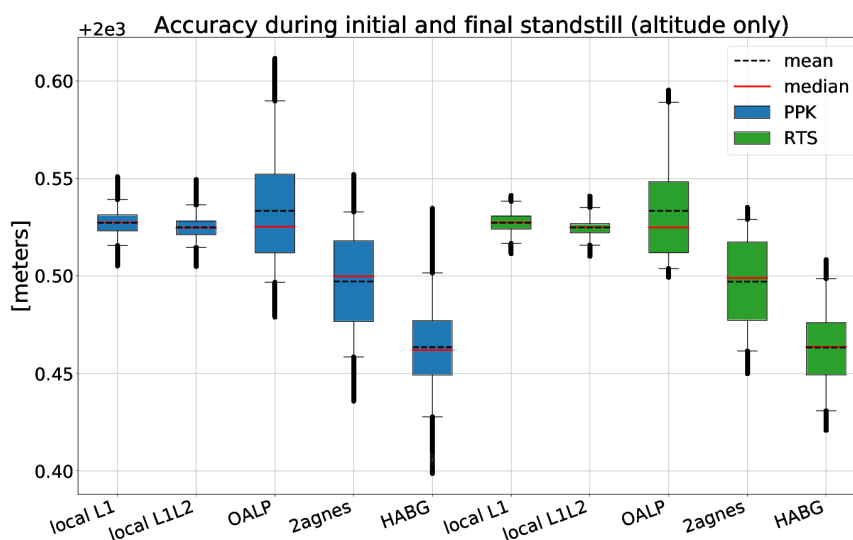
Figure 3.9: Accuracy of the geodetic altitude (WGS84) of all the PPK and RTS solutions (Table 3.2) during initial and final standstill for a total of 30 minutes of static acquisitions. The standstill position is at an altitude of 2000.53 m. The boxes indicate 50% of the values, the whiskers indicate 5% and 95% percentiles. The solutions obtained with the local reference station outperform the ones obtained with the AGNES reference stations.

a level of precision 6 times worse (with reference to the interquartile range indicated by the box). The solutions obtained with the HABG reference station present an offset of about 5 cm for the median altitude compared to the OALP ones, which reduces to about 2.5 cm for the solutions using both the OALP and the HAGB reference stations (labelled as 2agnes in the plots).

The positioning accuracy during the kinematic periods, relevant to the repeated passes of the radar along the rail, is visible in Figs. 3.10 and 3.11 reporting the deviations from the nominal trajectory. Both the single-frequency and the dual-frequency positioning solutions obtained with the local reference station show a positioning error about 4–5 times smaller than the (dual-frequency) ones obtained with the two AGNES reference stations, which also present an average offset of about 7 cm in the North component (visible in Fig. 3.10c and 3.10d). The HABG solution additionally shows an average altitude offset of about 8 cm.

The plots in Fig. 3.11 show the temporal variability of the altitude errors for the RTS local_L1 and the RTS OALP trajectories relevant to the repeat-pass radar acquisitions (i.e. during the forward movement of the platform). The lines are chronologically ordered and color-coded based on their acquisition time to highlight time-related error trends. In the case of the local reference station the pass-to-pass altitude error is mostly contained within a 1 cm interval with a maximum of 2.2 cm (Fig. 3.11a) while, in the case of the OALP AGNES reference station the error spreads over a range of 12 cm (Fig. 3.11b). During the 27 seconds of synthetic aperture time, the variation of the altitude error between the beginning and the end of the acquisitions is mostly sub-centimetre in the case of the local_L1 trajectory and around 1–1.5 cm in the case of the OALP trajectory, corresponding to a virtual inclination of the rail of less than 0.1 degrees.

The residual interferometric phase errors due to positioning errors are highlighted in Fig. 3.12 show-
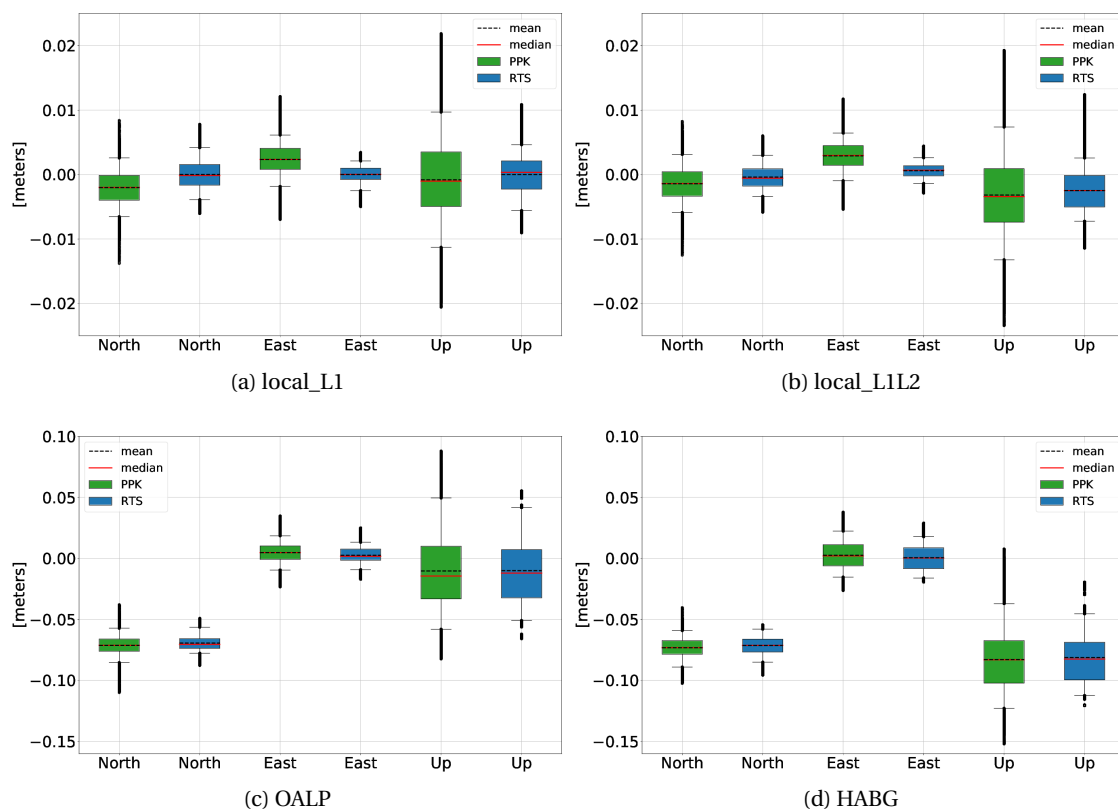
(a) local_L1

(b) local_L1L2

(c) OALP

(d) HABG

Figure 3.10: Accuracy of the PPK-only and the RTS (integrated INS/PPK) radar trajectories during the movement of the platform obtained with the local and the AGNES reference stations. The accuracy is indicated as the variation around the nominal trajectory. The boxes indicate 50% of the values, the whiskers indicate 5% and 95% percentiles. The coordinate system is the Cartesian East, North, Up with origin on the local reference GNSS receiver. Note that the range of values of the ordinate axis is 5 cm in Fig. 3.10a and 3.10b and 25 cm in Fig. 3.10c and 3.10d.

ing repeat-pass differential interferograms generated from acquisition pairs focused with the nominal quasi-linear trajectory and with the integrated INS/PPK trajectories obtained with the local reference station and with the OALP reference station (RTS local_L1 and RTS OALP, respectively). Three different temporal baselines are reported. The interferometric reference point is set on an exposed rock at a distance of about 2370 m from the rail midpoint (see Fig. 3.2). The colour map is limited to ±0.5 radians to enhance the visibility of the phase errors (out-of-range values are wrapped). In the case of the RTS local_L1 trajectories, the interferometric phase patterns are almost identical to the case of the nominal trajectory while different time-varying phase trends are visible in the case of the RTS OALP trajectories (Figs. 3.12g, 3.12h, and 3.12i).

The geocoded self-interferograms are reported in Fig. 3.13 and show the (differential) phase error caused by positioning errors, without the additional phase components related to the glacier flow and to the tropospheric phase gradient thanks to the zero temporal baseline (as explained in Section 3.2.3). The positioning errors of the RTS local_L1 trajectories mostly cause small scale phase noise (Figs. 3.13a, 3.13c, 3.13e) or a mild azimuth phase trend of less than 5°-10°. Conversely, the RTS OALP trajectories cause large phase trends affecting the entire mapped area, with phase errors up to 60°–90° with respect
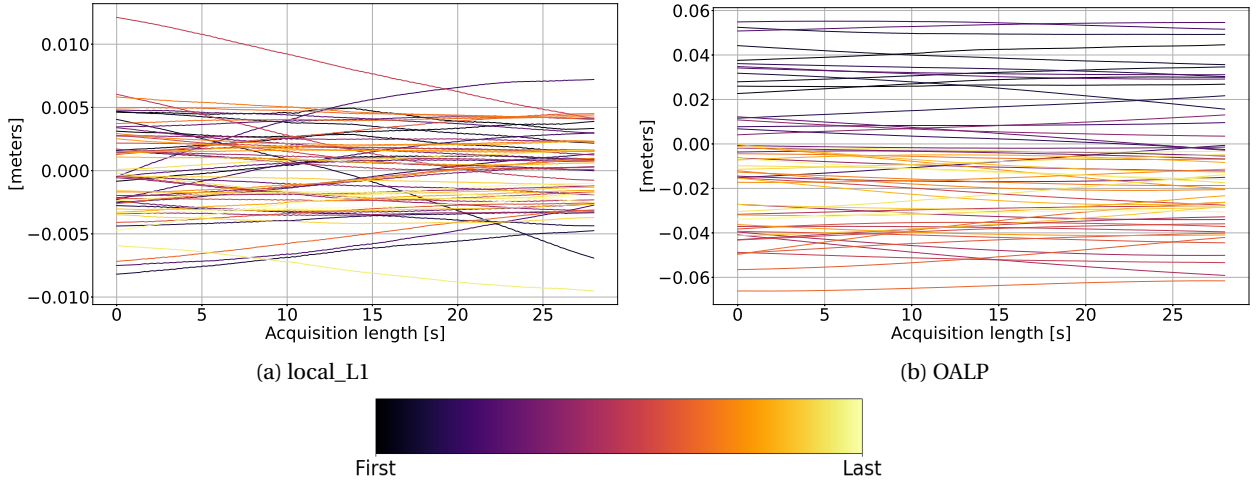
Figure 3.11: Deviation from the nominal trajectory (altitude only) of each individual repeat-pass trajectory (RTS solutions) obtained with the local reference station (local_L1) and the AGNES reference station (OALP). The trajectories are chronologically ordered according to their acquisition time and the error lines are sequentially color-coded (see colorbar). Note the different scale of the y-axis in the plots.

to the reference point, predominantly in azimuth (Figs. 3.13b, 3.13d, 3.13f).

3.4 DISCUSSION

The strong correlation between the long-term performance of the integrated INS/PPK positioning solutions and the temporal precision of the PPK-only ones (see Fig. 3.8) highlights the importance of accurate differential GNSS processing also when a high-performance INS is employed (as in the present test). In fact, the INS only provides position measurements relative to an initial point and therefore the uncompensated tropospheric path delays affecting the post-processed GNSS data play a major role on the long-term positioning accuracy of the integrated solution, ultimately affecting the repeat-pass spatial baseline error.

The trajectories obtained with the remote (AGNES) reference stations show large altitude undulations due to the uncompensated tropospheric path delays (Fig. 3.8), resulting in altitude offsets over repeated passes, as visible in Fig. 3.11b, which, in presence of a perpendicular baseline between the SAR acquisitions as in a car-borne or UAV-borne acquisition scenario, would lead to residual topographic errors. The correlation of the tropospheric effect on GNSS signals over short time intervals may lead to comparable errors affecting consecutive passes, as the partial concentration of lines with similar colors in Fig. 3.11b suggests. The better performance of the solutions involving the OALP reference station as compared to the HABG one is consistent with larger uncompensated tropospheric errors due to the considerable height difference of the HABG station from the rover (see Table 3.1). On the other hand, positioning offsets and error trends are substantially reduced by using the local reference station, since most of the tropospheric path delay is removed thanks to the short distance from the rover. Consequently, a more consistent repeatability of the estimated platform trajectories over multiple passes can

3

(a) Trajectories: nominal.
Acquisitions: 12:40:39–12:58:42

(b) Trajectories: nominal.
Acquisitions: 12:40:39–13:08:00

(c) Trajectories: nominal.
Acquisitions: 12:40:39–13:37:46

(d) Trajectories: RTS local_L1.
Acquisitions: 12:40:39–12:58:42

(e) Trajectories: RTS local_L1.
Acquisitions: 12:40:39–13:08:00

(f) Trajectories: RTS local_L1.
Acquisitions: 12:40:39–13:37:46

(g) Trajectories: RTS OALP.
Acquisitions: 12:40:39–12:58:42

(h) Trajectories: RTS OALP.
Acquisitions: 12:40:39–13:08:00

(i) Trajectories: RTS OALP.
Acquisitions: 12:40:39–13:37:46

−0.5 −0.4 −0.3 −0.2 −0.1 0.0 0.1 0.2 0.3 0.4 0.5
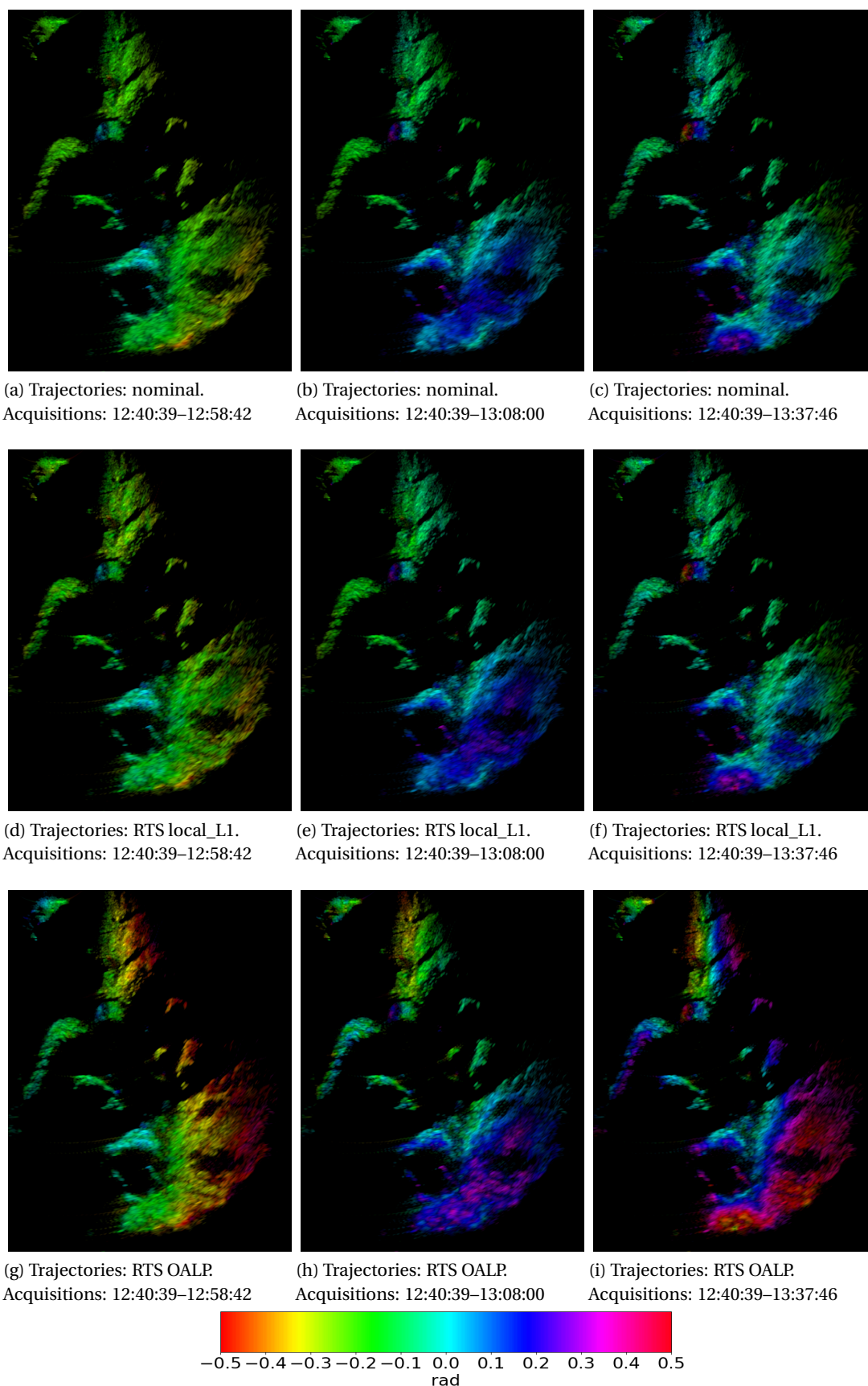rad

Figure 3.12: Repeat-pass DInSAR phase from image pairs focused with the nominal, the RTS local_L1, and the RTS OALP trajectories. Acquisition time indicated in the format HH:MM:SS. The images focused with the nominal and the local_L1 trajectories lead to comparable DInSAR phase while the images focused with the RTS OALP trajectories show additional phase undulations.

(a) Trajectory: RTS local_L1. Acquisition time: 12:40:39

(b) Trajectory: RTS OALP. Acquisition time: 12:40:39

(c) Trajectory: RTS local_L1. Acquisition time: 12:58:42

(d) Trajectory: RTS OALP. Acquisition time: 12:58:42

(e) Trajectory: RTS local_L1. Acquisition time: 13:37:46

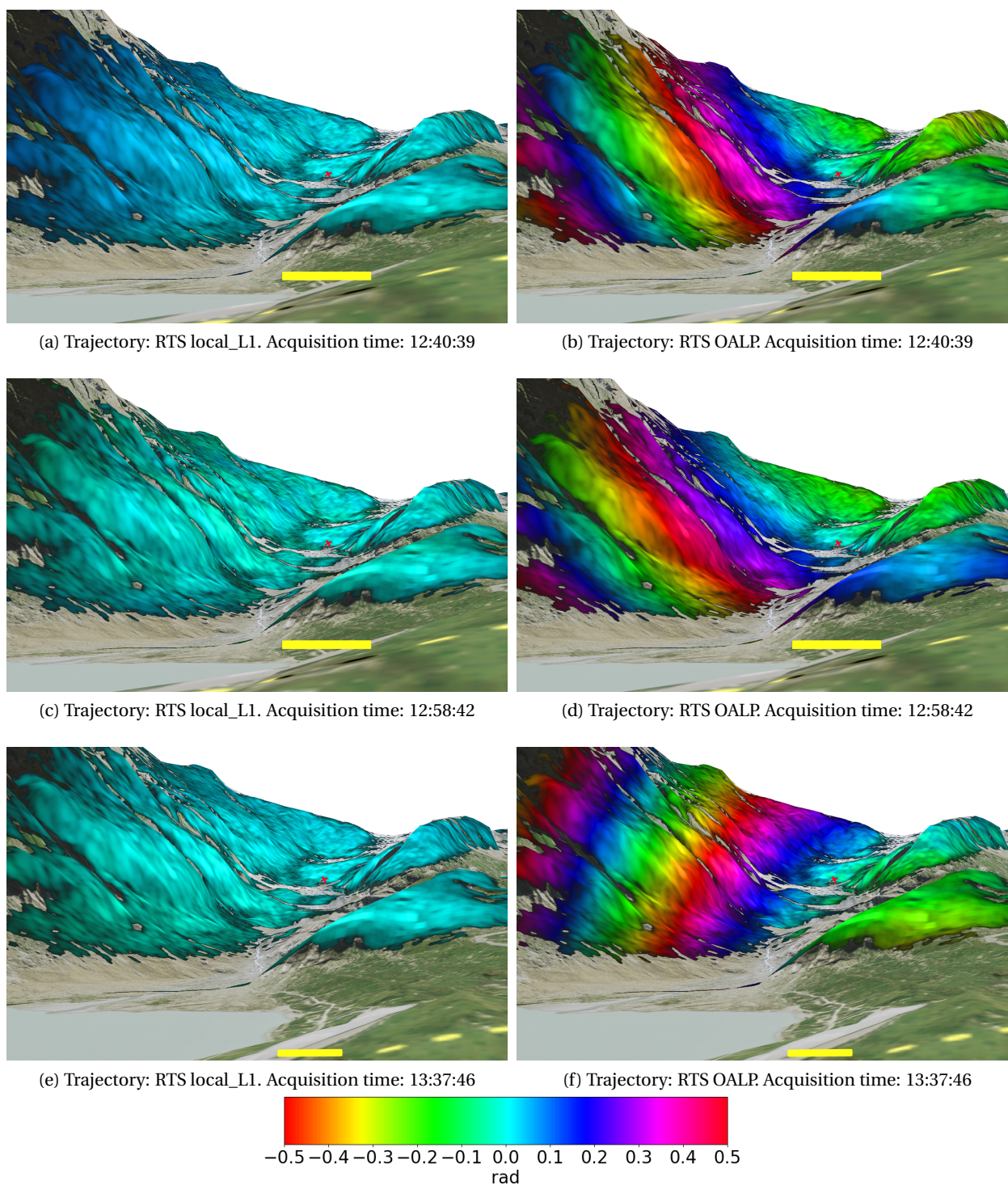(f) Trajectory: RTS OALP. Acquisition time: 13:37:46

Figure 3.13: Phase of the self-interferograms (both SLCs focused from the same raw data) for 3 different acquisitions. For each self-interferogram, the primary SLC is focused using the nominal trajectory and the secondary SLC is focused using the estimated radar trajectory obtained with the local reference station (RTS local_L1 trajectories) or with the OALP AGNES reference station (RTS OALP trajectories). The colour map is limited to ± 0.5 radians to enhance the visibility of the phase errors (out-of-range values are wrapped). The dotted yellow line indicates the direction of the rail. The filled yellow line is the average SAR trajectory along the rail (length of 10 meters). The red cross is the position of the interferometric reference point.

3

be achieved by using a local reference station, which is of considerable importance in the context of repeat-pass DInSAR applications.

Residual interferometric phase errors are visible in the differential interferograms as a consequence of the baseline errors caused by the uncertainty of the integrated INS/PPK trajectories. In the case of trajectories calculated with respect to the local reference station, the positioning errors account only for a fraction of the radar wavelength (about $\lambda/10$), consistent with the small-scale phase noise visible in the related self-interferograms.

Conversely, errors up to half wavelength are obtained with the remote reference station, causing the phase error trends visible in both the differential interferograms and in the self-interferograms. The phase trends are comparable to the ones resulting from a misalignment of the rail between different acquisitions, for example due to repositioning errors of the rail during different campaigns in discontinuous measurements mode [64, 66–68]. Larger phase errors are visible on the left flank of the valley where stronger look angle variations occur and where the distance from the interferometric reference point is larger.

In the rail-based configuration, the actual spatial baseline between the acquisitions is practically zero (besides small potential vibrations of the radar antennas) due to the constrained movement of the platform. Therefore, only negligible residual topographic phase variations are left in the differential interferograms as a consequence of baseline and DEM errors, consistently with the predominance of azimuth phase trends in the self-interferograms as compared to phase errors in range. On the other hand, in a car-borne repeat-pass acquisition scenario DEM errors should be taken into account. DEM offsets acts similarly to constant positioning errors and do not pose major problems in the interpretation of the interferograms due to the relative nature of the interferometric measurements [22, 64]. On the other hand, relative height errors between the resolution cells or lateral translations of the DEM add up to positioning errors and can determine varying phase errors along azimuth and range.

Finally, especially in the case of long temporal baselines, the tropospheric phase error also affect the differential interferograms and cannot be easily distinguished from uncompensated positioning-related phase errors. Tropospheric phase error are caused by local gradients of the refractive index, which is height dependent and is a function of temperature, pressure, and humidity content of the air and therefore particularly relevant in the case of steep slopes [61]. As a rough estimate, the tropospheric path delays affecting ground-based radar measurements can be in the order of mm/km or cm/km in range [69, 70] which, at L-band, correspond to phase variations between 3°/km and 30°/km or more, and therefore of comparable order of magnitude with respect to phase trends caused by positioning errors.

3.5 CONCLUSIONS

In this work, trajectory errors experienced between repeated SAR acquisitions and within the time-span of a synthetic aperture with long integration time measured with a navigation-grade INS/GNSS system were analysed. The analysis was carried out in a controlled rail-based setup with different INS/GNSS configurations. The analysis highlighted the positioning performance and the related differential inter-

ferometric performance arising from the use of GNSS reference stations at different distances from the radar platform.

The results showed that the residual positioning errors obtained by relying on the (remote) reference stations of the permanent GNSS network can be substantial, thus causing non-negligible residual phase error trends. A significant reduction of the phase errors can be achieved by using a reference station located close to the radar platform, which allows to effectively remove most of the tropospheric disturbance affecting the GNSS signals and to achieve good trajectory repeatability over multiple passes. This last aspect is particularly relevant in the context of repeat-pass DInSAR acquisitions from agile platforms as the aim is to achieve the higher possible sensitivity to the deformation signal of interest and, hence, low phase error variance.

Strong platform dynamics and attitude variations could further worsen the positioning positioning errors and should be analysed in a future work. Moreover, longer synthetic aperture times, which can be in the order of a few minutes in car-borne SAR acquisitions, should be considered in future analyses to better assess the positioning performance within the time span of the synthetic aperture.

REFERENCES

[1] H. A. Zebker and R. M. Goldstein, "Topographic mapping from interferometric synthetic aperture radar observations," *Journal of Geophysical Research: Solid Earth*, vol. 91, no. B5, pp. 4993–4999, 1986.

[2] A. K. Gabriel, R. M. Goldstein, and H. A. Zebker, "Mapping small elevation changes over large areas: differential radar interferometry," *Journal of Geophysical Research*, vol. 94, no. B7, pp. 9183–9191, 1989.

[3] R. Bamler and P. Hartl, "Synthetic aperture radar interferometry," *Inverse Problems*, vol. 14, pp. 1–54, Aug 1998.

[4] G. Fornaro, E. Sansosti, R. Lanari, and M. Tesauro, "Role of processing geometry in SAR raw data focusing," *IEEE Transactions on Aerospace and Electronic Systems*, vol. 38, pp. 441–454, Apr 2002.

[5] D. R. Stevens, I. G. Cumming, and A. L. Gray, "Options for airborne interferometric SAR motion compensation," *IEEE Transactions on Geoscience and Remote Sensing*, vol. 33, no. 2, pp. 409–420, 1995.

[6] O. Frey, C. Magnard, M. Rüegg, and E. Meier, "Focusing of airborne synthetic aperture radar data from highly nonlinear flight tracks," *IEEE Transactions on Geoscience and Remote Sensing*, vol. 47, pp. 1844–1858, Jun 2009.

[7] S. Perna, V. Zamparelli, A. Pauciullo, and G. Fornaro, "Azimuth-to-frequency mapping in airborne SAR data corrupted by uncompensated motion errors," *IEEE Geoscience and Remote Sensing Letters*, vol. 10, no. 6, pp. 1493–1497, 2013.

[8] D. Blacknell, A. Freeman, S. Quegan, I. A. Ward, I. P. Finley, C. J. Oliver, R. G. White, and J. W. Wood, "Geometric accuracy in airborne SAR images," *IEEE Transactions on Aerospace and Electronic Systems*, vol. 25, pp. 241–258, Mar 1989.

[9] S. Buckreuss, "Motion errors in an airborne synthetic aperture radar system," *European Transactions on Telecommunications*, vol. 2, no. 6, pp. 655–664, 1991.

[10] G. Fornaro, "Trajectory deviations in airborne SAR: analysis and compensation," *IEEE Transactions on Aerospace and Electronic Systems*, vol. 35, pp. 997–1009, jul 1999.

[11] G. Fornaro, G. Franceschetti, and S. Perna, "Motion compensation errors: Effects on the accuracy of airborne SAR images," *IEEE Transactions on Aerospace and Electronic Systems*, vol. 41, no. 4, pp. 1338–1352, 2005.

[12] S. Buckreuss, "Motion compensation for airborne SAR based on inertial data, RDM and GPS," in *1994 IEEE International Geoscience and Remote Sensing Symposium*, vol. 4, pp. 1971–1973, IEEE, 1994.

[13] J. L. Weston and D. H. Titterton, "Modern inertial navigation technology and its application," *Electronics Communication Engineering Journal*, vol. 12, pp. 49–64, Apr 2000.

[14] D. Titterton and J. L. Weston, *Strapdown Inertial Navigation Technology*. Radar, Sonar and Navigation, Institution of Engineering and Technology, 2004.

[15] A. Reigber and K. Papathanassiou, "Correction of residual motion errors in airborne repeat-pass interferometry," in *2001 IEEE International Geoscience and Remote Sensing Symposium*, vol. 7, pp. 3077–3079, IEEE, 2001.

[16] A. Reigber, P. Prats, and J. Mallorqui, "Refined Estimation of Time-Varying Baseline Errors in Airborne SAR Interferometry," *IEEE Geoscience and Remote Sensing Letters*, vol. 3, pp. 145–149, Jan 2006.

[17] P. Prats, A. Reigber, J. J. Mallorqui, and A. Broquetas, "Efficient detection and correction of residual motion errors in airborne SAR interferometry," in *2004 IEEE International Geoscience and Remote Sensing Symposium*, vol. 2, pp. 992–995, Sep. 2004.

[18] N. Cao, H. Lee, E. Zaugg, R. Shrestha, W. E. Carter, C. Glennie, Z. Lu, and H. Yu, "Estimation of residual motion errors in airborne SAR interferometry based on time-domain backprojection and multisquint techniques," *IEEE Transactions on Geoscience and Remote Sensing*, vol. 56, pp. 2397–2407, Apr 2018.

[19] R. S. Goodman, S. Tummala, and W. G. Carrara, "Issues in ultra-wideband, widebeam SAR image formation," in *Record of 1995 IEEE Radar Conference*, pp. 479–485, May.

[20] S. N. Madsen, "Motion compensation for ultra wide band SAR," in *2001 IEEE International Geoscience and Remote Sensing Symposium*, vol. 3, pp. 1–3, 2001.

[21] A. Reigber, E. Alivizatos, A. Potsis, and A. Moreira, "Extended wavenumber-domain synthetic aperture radar focusing with integrated motion compensation," *IEE Proceedings - Radar, Sonar and Navigation*, vol. 153, no. 3, pp. 301–310, 2006.

[22] M. I. Duersch and D. G. Long, "Analysis of time-domain back-projection for stripmap SAR," *International Journal of Remote Sensing*, vol. 36, no. 8, pp. 2010–2036, 2015.

[23] ISO (International Organisation for Standardisation), *ISO 5725-1: 1994 - Accuracy (trueness and precision) of measurement methods and results-Part 1: General principles and definitions*, 1994.

[24] D. Lu, D. Spiegel, U. Becker, B. Cai, J. Wang, J. Liu, and X. Liu, "Repeatability test method of GNSS for safe train localisation in real and simulated environments," in *2016 IEEE/ION Position, Location and Navigation Symposium (PLANS)*, pp. 687–692, Apr 2016.

[25] R. Coscione, I. Hajnsek, and O. Frey, "Trajectory uncertainty in repeat-pass SAR interferometry: A case study," in *2019 IEEE International Geoscience and Remote Sensing Symposium*, pp. 338–341, Jul 2019.

[26] R. E. Kalman, "A New Approach to Linear Filtering and Prediction Problems," *Journal of Basic Engineering*, vol. 82, no. 1, p. 35, 1960.

[27] P. Georgiadou and A. Kleusberg, "On the effect of ionospheric delay on geodetic relative GPS positioning," *Journal of Geodesy*, vol. 13, no. 1, pp. 1–8, 1988.

[28] H. Nahavandchi and A. Soltanpour, "Local ionospheric modelling of GPS code and carrier phase observations," *Survey Review*, vol. 40, no. 309, pp. 271–284, 2008.

[29] T. Hobiger and N. Jakowski, *Atmospheric Signal Propagation*, pp. 165–193. Springer International Publishing, 2017.

[30] B. Hofmann-Wellenhof, H. Lichtenegger, and E. Wasle, *GNSS — Global Navigation Satellite Systems: GPS, GLONASS, Galileo, and more.* Springer Vienna, 2008.

[31] Y. Feng and J. Wang, "GPS RTK performance characteristics and analysis," *Journal of Global Positioning Systems*, vol. 7, no. 1, pp. 1–8, 2008.

[32] C. Rajasekhar, V. B. S. S. I. Dutt, and G. S. Rao, "Role of optimum satellite-receiver geometry in the accuracy of GPS navigation solution - an investigation," in *2015 International Conference on Communications and Signal Processing (ICCSP)*, pp. 1185–1189, Apr 2015.

[33] R. A. Snay and T. Soler, *Continuously Operating Reference Station (CORS): History, Applications, and Future Enhancements*, ch. Chapter 1, pp. 1–10.

[34] C. Bruyninx, Z. Altamimi, C. Boucher, E. Brockmann, A. Caporali, W. Gurtner, H. Habrich, H. Hornik, J. Ihde, A. Kenyeres, J. Mäkinen, G. Stangl, H. van der Marel, J. Simek, W. Söhne, J. Torres, and G. Weber, *The European Reference Frame: Maintenance and Products*, pp. 131–136. Berlin, Heidelberg: Springer Berlin Heidelberg, 2009.

[35] E. Brockmann, S. Grünig, D. Ineichen, and S. Schaer, "Monitoring the automated GPS network of Switzerland AGNES," *Report on the Symposium of the IAG Subcommission for Europe (EUREF)*, vol. 28, p. 100, 2006.

[36] A. Potsis, A. Reigber, J. Mittermayer, A. Moreira, and N. Uzunoglou, "Sub-aperture algorithm for motion compensation improvement in wide-beam SAR data processing," *Electronics Letters*, vol. 37, no. 23, pp. 1405–1407, 2001.

[37] A. Reigber and R. Scheiber, "Airborne differential SAR interferometry: First results at L-band," *IEEE Transactions on Geoscience and Remote Sensing*, vol. 41, no. 6 PART II, pp. 1516–1520, 2003.

[38] K. A. C. de Macedo and R. Scheiber, "Precise topography- and aperture-dependent motion compensation for airborne SAR," *IEEE Geoscience and Remote Sensing Letters*, vol. 2, no. 2, pp. 172–176, 2005.

[39] P. Prats, A. Reigber, and J. J. Mallorqui, "Topography-dependent motion compensation for repeat-pass interferometric SAR systems," *IEEE Geoscience and Remote Sensing Letters*, vol. 2, pp. 206–210, Apr 2005.

[40] P. Prats, K. A. C. de Macedo, A. Reigber, R. Scheiber, and J. J. Mallorqui, "Comparison of topography- and aperture-dependent motion compensation algorithms for airborne SAR," *IEEE Geoscience and Remote Sensing Letters*, vol. 4, no. 3, pp. 349–353, 2007.

[41] H. M. J. Cantalloube and C. E. Nahum, "Autofocusing of (inverse) synthetic aperture radar for motion compensation," *Aerospace and Electronics*, 1996.

[42] P. Decroix, X. Neyt, and M. Acheroy, "Trade-off between motion measurement accuracy and autofocus capabilities in airborne SAR motion compensation," in *2nd Microwave and Radar Week in Poland - International Radar Symposium, IRS 2006, Proceedings*, 2006.

[43] K. A. C. de Macedo, R. Scheiber, and A. Moreira, "An autofocus approach for residual motion errors with application to airborne repeat-pass SAR interferometry," *IEEE Transactions on Geoscience and Remote Sensing*, vol. 46, pp. 3151–3162, Oct 2008.

[44] R. Coscione, I. Hajnsek, and O. Frey, "An experimental car-borne SAR system: Measurement setup and positioning error analysis," in *2018 IEEE International Geoscience and Remote Sensing Symposium*, pp. 6364–6367, 2018.

[45] O. Frey, C. L. Werner, I. Hajnsek, and R. Coscione, "A car-borne SAR system for interferometric measurements: Development status and system enhancements," in *2018 IEEE International Geoscience and Remote Sensing Symposium*, pp. 6508–6511, 2018.

[46] O. Frey, C. Werner, and R. Coscione, "Car-borne and UAV-borne mobile mapping of surface displacements with a compact repeat-pass interferometric SAR system at L-band," in *2019 IEEE International Geoscience and Remote Sensing Symposium*, pp. 274–277, Jul 2019.

[47] P. D. Groves, *Principles of GNSS, inertial, and multisensor integrated navigation systems.* GNSS technology and applications series, Boston: Artech House, 2nd ed. ed., 2013.

[48] H. E. Rauch, C. T. Striebel, and F. Tung, "Maximum likelihood estimates of linear dynamic systems," *AIAA Journal*, vol. 3, pp. 1445–1450, Aug 1965.

[49] E. L. Hinüber, C. Reimer, T. Schneider, and M. Stock, "INS/GNSS integration for aerobatic flight applications and aircraft motion surveying," *Sensors (Switzerland)*, vol. 17, p. 941, Apr 2017.

[50] C. M. Silva, D. B. Alves, E. M. Souza, and P. T. Setti Junior, "Ionospheric scintillation impact on ambiguity resolution using ADOP in closed form," *Advances in Space Research*, vol. 64, pp. 921–932, Aug 2019.

[51] A. E.-S. El-Rabbany, *The effect of physical correlations on the ambiguity resolution and accuracy estimation in GPS differential positioning.* PhD thesis, Department of Geodesy and Geomatics Engineering Technical Report No. 170, 1994.

[52] C. Miller, K. O. Keefe, and Y. Gao, "Time correlation in GNSS positioning over short baselines," *Journal of Surveying Engineering*, vol. 138, no. 1, pp. 17–24, 2012.

[53] O. Frey, C. Magnard, M. Rüegg, and E. Meier, "Non-linear SAR data processing by time-domain back-projection," *Synthetic Aperture Radar (EUSAR)*, pp. 1–4, 2008.

[54] O. Frey, C. L. Werner, and U. Wegmüller, "GPU-based parallelized time-domain back-projection processing for agile SAR platforms," in *2014 IEEE International Geoscience and Remote Sensing Symposium*, pp. 1132–1135, 2014.

[55] O. Frey, C. L. Werner, and U. Wegmüller, "GPU-based parallelized time-domain back-projection processing for agile SAR platforms," in *2014 IEEE International Geoscience and Remote Sensing Symposium*, pp. 1132–1135, 2014.

[56] O. Frey, E. H. Meier, and D. R. Nüesch, "Processing SAR data of rugged terrain by time-domain back-projection," in *SAR Image Analysis, Modeling, and Techniques VII* (F. Posa, ed.), vol. 5980, pp. 71 – 79, International Society for Optics and Photonics, SPIE, Oct 2005.

[57] A. Ribalta, "Time-domain reconstruction algorithms for FMCW-SAR," *IEEE Geoscience and Remote Sensing Letters*, vol. 8, pp. 396–400, May 2011.

[58] G. Nico, D. Leva, G. Antonello, and D. Tarchi, "Ground-based SAR interferometry for terrain mapping: theory and sensitivity analysis," *IEEE Transactions on Geoscience and Remote Sensing*, vol. 42, pp. 1344–1350, June 2004.

[59] R. Caduff, F. Schlunegger, A. Kos, and A. Wiesmann, "A review of terrestrial radar interferometry for measuring surface change in the geosciences," *Earth Surface Processes and Landforms*, vol. 40, no. 2, pp. 208–228, 2015.

[60] S. Placidi, A. Meta, L. Testa, and S. Rödelsperger, "Monitoring structures with FastGBSAR," in *2015 IEEE Radar Conference*, pp. 435–439, Oct 2015.

[61] R. F. Hanssen, *Radar Interferometry: Data Interpretation and Error Analysis*. Remote Sensing and Digital Image Processing, Springer, 2001.

[62] P. A. Rosen, S. Hensley, I. R. Joughin, F. K. Li, S. N. Madsen, E. Rodriguez, and R. M. Goldstein, "Synthetic aperture radar interferometry," *Proceedings of the IEEE*, vol. 88, no. 3, pp. 333–382, 2000.

[63] H. Ku, "Notes on the use of propagation of error formulas," *Journal of Research of the National Bureau of Standards, Section C: Engineering and Instrumentation*, vol. 70C, p. 263, Oct 2012.

[64] H. Bähr and R. F. Hanssen, "Reliable estimation of orbit errors in spaceborne SAR interferometry," *Journal of Geodesy*, vol. 86, pp. 1147–1164, May 2012.

[65] A. Pepe and F. Caló, "A review of interferometric synthetic aperture radar (insar) multi-track approaches for the retrieval of earth's surface displacements," *Applied Sciences*, vol. 7, no. 12, 2017.

[66] Z. Wang, Z. Li, and J. Mills, "Modelling of instrument repositioning errors in discontinuous multi-campaign ground-based SAR (MC-GBSAR) deformation monitoring," *ISPRS Journal of Photogrammetry and Remote Sensing*, vol. 157, pp. 26–40, 2019.

[67] C. Hu, J. Zhu, Y. Deng, W. Tian, and P. Yin, "Repositioning error compensation in discontinuous ground-based SAR monitoring," *Remote Sensing*, vol. 13, p. 2461, Jun 2021.

[68] O. Monserrat, M. Crosetto, and G. Luzi, "A review of ground-based SAR interferometry for deformation measurement," *ISPRS Journal of Photogrammetry and Remote Sensing*, vol. 93, pp. 40–48, 2014.

[69] L. Iannini and A. Monti Guarnieri, "Atmospheric phase screen in ground-based radar: Statistics and compensation," *IEEE Geoscience and Remote Sensing Letters*, vol. 8, pp. 537–541, May 2011.

[70] R. Iglesias, X. Fabregas, A. Aguasca, J. J. Mallorqui, C. Lopez-Martinez, J. A. Gili, and J. Corominas, "Atmospheric phase screen compensation in ground-based SAR with a multiple-regression model over mountainous regions," *IEEE Transactions on Geoscience and Remote Sensing*, vol. 52, pp. 2436–2449, May 2014.

4

TEMPORAL ANALYSIS OF THE CAR-BORNE INTERFEROMETRIC PERFORMANCE IN NATURAL AREAS

4.1 INTRODUCTION

In repeat-pass interferometric applications [1, 2], the ability to retrieve meaningful geophysical information of the imaged area from the analysis of the temporal evolution of the interferometric measurements is limited by the coherence achievable in the time span between the acquisitions. Coherence loss (decorrelation) can be caused by changes within the resolution cells, at the level of the radar wavelength, of the scattering mechanisms [3].

Vegetated areas are particularly prone to temporal decorrelation [4, 5]. Low-frequency microwave radar bands, such as L-band or lower, provide robustness towards small movements in the resolution cell and, hence, generally higher coherence also in vegetated or partially vegetated areas [3, 6, 7]. While natural morphological changes (e.g. vegetation growth) and anthropogenic intervention lead to decorrelation over long time spans [5, 7, 8], over short time intervals, local weather conditions such as wind, moisture, and temperature changes can drive large part of the coherence variations in vegetated areas [9–13].

To understand the radar response under different weather conditions, it is important to quantitatively assess, for specific classes of land cover, the backscattering and the coherence changes over time intervals calibrated to the expected weather changes. Particularly in mountainous regions, local weather conditions can change quite drastically spatially and temporally over time scales of minutes, hours, or days. It is therefore crucial to obtain backscatter and interferometric time-series with high temporal resolutions.

However, availability of such time-series at the radar frequencies suitable for monitoring vegetated regions, such as L-band or P-band, is limited. Spaceborne SAR systems have temporal baselines of at least a few days or weeks and can therefore only provide insights on the medium/long-term temporal decorrelation effects. Airborne SAR systems can provide the required temporal sampling, although the high cost per flight makes it burdensome to obtain acquisitions with high temporal resolution over multiple days [11, 14]. A noteworthy temporal decorrelation analysis in forested areas was presented

in [10] where, based on the data from three airborne campaigns (BioSAR 2007, TempoSAR 2008 and TempoSAR 2009), the influence of wind and rain on the polarimetric-interferometric performance for the estimation of forest height was discussed. In an empirical experiment performed with the UAVSAR [12], rainfalls were identified as possible drivers for the interferometric decorrelation in forested areas. Tower-based scatterometer experiments at L- and P-band have been presented in [15, 16] where the dependence of the interferometric coherence on the vegetation water content and the wind speed variance was reported.

However, to the authors' knowledge, there is no available analysis of the medium/short-term repeat-pass interferometric performance achieved from ground-based SAR systems at L-band.

The goal of the present work is to provide a quantitative assessment of the temporal changes of the radar measurements performed with the L-band car-borne SAR system [17–19] over time intervals of minutes, hours, and days, with a focus on vegetated areas. Repeat-pass DInSAR acquisitions were performed in a mountainous region in Northeastern Switzerland. The temporal evolution of the radar backscattering and of the differential interferometric coherence and phase are analysed in different natural land covers and compared against local weather measurements (wind speed, rainfalls, relative air humidity, and temperature).

The high temporal sampling of the car-borne repeat-pass acquisitions allows to analyse coherence changes on different time scales and to observe transient weather-related effects that would be hardly visible with coarse temporal resolutions.

4.2 DATA AND METHODS

Experimental setup and radar data   From November 5, 2018, to November 20, 2018, we performed a series of SAR acquisitions by driving the car-borne radar system along a roughly straight road distant 2–3 km from the target area. The car-borne SAR system (Fig. 2.1) comprises one transmitting and three receiving dual-polarization antennas (using either H or V polarization). The radar is a frequency-modulated continuous-wave (FMCW) system operating at L-band (wavelength 22.6 cm) with a bandwidth of 100 MHz, corresponding to a range resolution of 1.5 m (single look). The synthetic aperture length is about 250 m, corresponding to an azimuth resolution in the regions of interest of about 1–1.4 m (single look).

A navigation-grade INS/GNSS system (iMAR iNAV-RQH-10018) was rigidly mounted on the car for accurate trajectory measurements. A portable GNSS reference station (Fig. 2.2) was located in the area to allow for high-precision carrier-phase differential GNSS processing in support of the trajectory estimation.

The dataset is composed of 32 HH polarized acquisitions relevant to Nov. 5–8 and Nov. 19–20, and 39 VV polarized acquisitions relevant to Nov. 14–15 and Nov. 19–20. All acquisitions have a chirp length of 2 ms.

(a) Photograph of the target area taken on Nov. 14, 2018. The forested areas are comprised of deciduous trees and coniferous trees with a larger proportion of the latter.
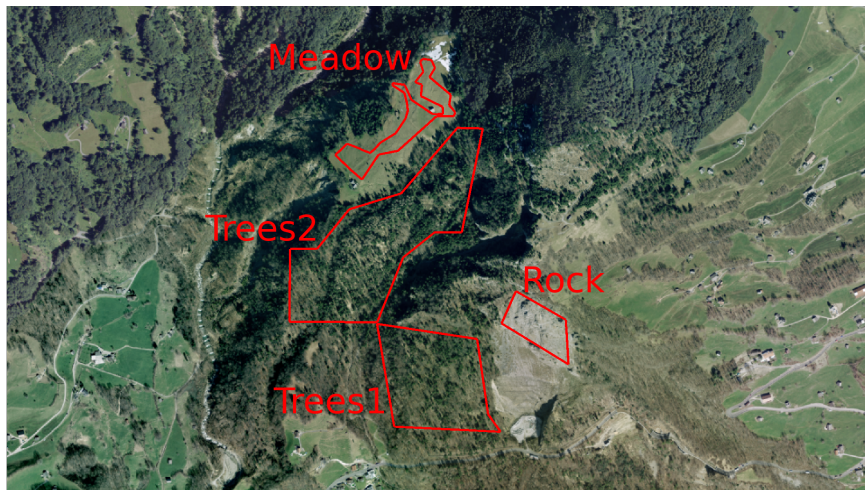
(b) Aerial view of the target area (©swisstopo geodata). The four regions of interest (one rocky area, two forested areas, and one meadow area) are indicated by the red polygons. The range distance of each region of interest from the radar mid position is 2.6–2.7 km for "rock", 2.2–2.5 km for "trees1" , 2.3–3.0 km for "trees2", and 2.8–3.1 km for "meadow". Look angles, measured from the nadir, vary between 93° and 103° from near-range to far-range.

(c) Close-up view of the rock area (©swisstopo geodata). Scattered vegetation in the area is visible.

Figure 4.1: Optical images of the target area.

4

Study area   The study area is located in Northeastern Switzerland, in the Canton of St. Gallen. It is a mountainous region mainly covered by vegetation and characterised by rough topography (Fig. 4.1).

Four regions of interest (ROI) each characterised by a relatively homogeneous land cover were selected to conduct the time-series analyses (Fig. 4.1b): a portion of the rocky area not affected by shadow or layover, two separate groups of trees (trees1 and trees2), and a meadow area. Sparse vegetated spots are also present in the rocky area, as it can be observed in Fig. 4.1c. The forested areas are comprised of deciduous trees and coniferous trees with a larger proportion of the latter. The range distance of each region of interest from the radar mid position is 2.6–2.7 km for the rock, 2.2–2.5 km for the trees1 area, 2.3–3.0 km for trees2 area, and 2.8–3.1 km for the meadow one.

Weather data   Weather parameters were measured by different stations of the MeteoSchweiz Swiss-MetNet [20] located in the vicinity of the target area. Wind speed was measured by the Schänis station, located about 4-5 km away from the ROIs. Temperature, dew point, and relative air humidity were measured by the Gäsi station, located about 1-2 km away from the ROIs. Finally, rainfalls were measured in terms of precipitation rate by the Gäsi station and in terms of average precipitation in a 10 minutes interval by the Weesen station and the Filzbach station (1-2 km and 2-3 km distance from the ROIs, respectively). The data has a sampling rate of 10 minutes.

Radar Processing   Radar focusing was performed using a time domain back-projection approach [21, 22], which, for each transmitted and received echo, takes into account position, velocity and attitude of the radar platform as measured by the integrated INS/GNSS system. Focusing was performed directly in map coordinates using a SwissALTI3D digital elevation model (DEM) with a posting of 25 cm provided by the Swiss federal office of topography (swisstopo).

By focusing in map coordinates, the phase contribution due to the topography is removed with a precision that depends on the DEM and the trajectory data [23]. Henceforth, interferometric combination of TDBP-focused images directly results in differential interferogram.

Backscattering analysis   As the platform moves along the synthetic aperture, the radar collects the complex backscattered echoes that are then summed together in the time domain focusing approach on a pixel-by-pixel basis. The spatial sampling of the synthetic antenna is defined by the platform speed, the integration time, and the radar pulse repetition frequency (PRF), which for FMCW systems depends on the chirp length.

Since the integration time is fixed but the platform speeds can have small variations during each pass, the number of echoes contributing to the image formation differs from acquisition to acquisition, thus affecting the backscatter intensity of each pixel. Lower speeds imply a larger number of echoes and hence higher backscatter. To take into account such effect in the analysis of the backscatter time-series, the intensity of each acquisition has been normalised to the number of echoes used for the image formation.

Coherence analysis   Given two complex SAR returns $\tilde{s}_1$ and $\tilde{s}_2$, for each image pixel k the normalised complex correlation is defined as:

$$\tilde{\Gamma}(k) = \frac{\mathbb{E}\left\{\tilde{s}_1(k) \cdot \tilde{s}_2^*(k)\right\}}{\sqrt{\mathbb{E}\left\{|\tilde{s}_1(k)|^2\right\}\mathbb{E}\left\{|\tilde{s}_2(k)|^2\right\}}} \tag{4.1}$$

where $\mathbb{E}$ is the ensemble average. In practice, the ensemble average is replaced by the spatial average implemented via a moving window for each pixel [24, 25]:

$$\tilde{\gamma}(k) = \frac{\sum_{i=1}^{N_L} \tilde{s}_{1i}(k) \cdot \tilde{s}_{2i}^*(k)}{\sqrt{\sum_{i=1}^{N_L} |\tilde{s}_{1i}(k)|^2 \sum_{i=1}^{N_L} |\tilde{s}_{2i}(k)|^2}} \tag{4.2}$$

where $\tilde{s}_{1i}(k)$ and $\tilde{s}_{2i}(k)$ indicate the values of the signals in a generic pixel i inside the averaging window of dimension N_L around the pixel k.

From Eq. (4.2) the interferometric coherence and phase can be calculated as:

$$\gamma = |\tilde{\gamma}| \tag{4.3}$$

$$\varphi = \arctan \frac{\Im(\tilde{\gamma})}{\Re(\tilde{\gamma})} \tag{4.4}$$

where $\Im$ and $\Re$ indicate the imaginary and the real part, respectively.

(a) Phase   (b) Coherence
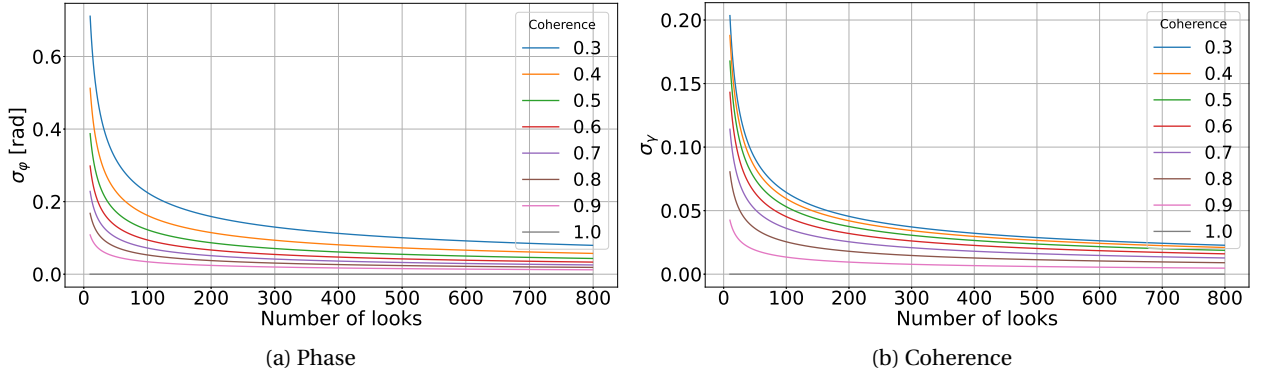
Figure 4.2: Phase and coherence standard deviation vs. number of looks for different coherence values

To set the number of looks, we refer to the Cramer–Rao lower bound of the estimated phase and coherence standard deviations (σ_φ and σ_γ, respectively) in function of the actual coherence and the number of looks [26]:

$$\sigma_\varphi = \frac{1}{\sqrt{2N_L}}\sqrt{\frac{(1 - |\tilde{\Gamma}|^2)}{|\tilde{\Gamma}|^2}} \tag{4.5}$$

$$\sigma_\gamma = \frac{1}{\sqrt{2N_L}}(1 - |\tilde{\Gamma}|^2) \tag{4.6}$$

Eq. (4.5) and (4.6) are plotted in Fig. 4.2 against the number of looks for different coherence values. Considering a threshold for the phase standard deviation of 0.1 rad (for coherence above 0.4), we set a multilooking window dimension of about 20m × 40m (range × azimuth in the slant plane) resulting in a number of looks between 400 and 600. Correspondingly, the estimated coherence standard deviation is below 0.03 and the coherence bias given by [27, part C, Eq. (1.15)]

$$\mathbb{E}(\gamma) = \sqrt{\frac{\pi}{4N_L}} \tag{4.7}$$

(valid for $|\tilde{\Gamma}|$=0) is below 0.04. Considering that the imaged ROIs are characterised by the presence of natural distributed scatterers, we deem the dimension of the multilooking window to be a good compromise between the goodness of the second-order statistics and the spatial resolution.

The coherence can be factorised as

$$\gamma = \gamma_{\text{geo}} \cdot \gamma_{\text{vol}} \cdot \gamma_{\text{DEM}} \cdot \gamma_{\text{temp}} \cdot \gamma_{\text{noise}} \tag{4.8}$$

where γ_{geo} is the geometric coherence , γ_{vol} is the volume coherence, γ_{temp} is the temporal coherence, and γ_{noise} is the coherence due to noise.

As the DEM does not take into account the presence of the trees but only the terrain height, interferometric topographic errors may arise in presence of perpendicular spatial baselines between the acquisitions. The coherence loss caused by DEM errors can be obtained from [28]

$$\gamma_{DEM} = \exp\left\{-\frac{1}{2}\left(2\pi\frac{\sigma_z}{h_a}\right)^2\right\} \tag{4.9}$$

where σ_z is the DEM error and h_a is the ambiguity height that depends on the radar wavelength λ, the look angle θ, the slant range r, and the perpendicular baseline $B_\perp$ [6]:

$$h_a = \frac{\lambda r \sin(\theta)}{2B_\perp} \tag{4.10}$$

In our case, all SAR acquisitions were performed while driving on the same road and therefore are mostly separated by horizontal baselines. The maximum horizontal baseline as measured by the INS/GNSS system is about 1 meter. With look angles ranging approximately between 93° and 103° from near-range to far-range, the maximum perpendicular baseline is in the order of 20 cm, resulting in ambiguity heights above 1.2 km.

In the hypothesis that the scattering centres within the resolution cells are uncorrelated and uniformly distributed, the geometrical coherence factor is equal to [3]

$$\gamma_{\text{geo}} = 1 - \frac{2\delta_y \cdot B \cdot \cos^2(\theta)}{\lambda r} \tag{4.11}$$

where δ_y is the ground range resolution, B is the spatial baseline, and r is the slant range distance between the radar sensor and the target. Accordingly, with spatial baselines spanning a maximum of

1 meter horizontally, the geometrical coherence achievable in the ROIs is $\gamma_{\text{geo}} > 0.99$. Therefore, the decorrelation due to the geometric difference of the two acquisitions can be safely neglected, besides in areas affected by strong foreshortening where the worsening of the ground resolution can cause decorrelation. This can occur for example in some parts of the rock ROI. However, since the variation of the spatial baselines between different acquisitions is small (sub-meter), the coherence variation over time is also small and therefore has a small impact on the temporal analysis.

Thermal noise of the interferometric channels affect the coherence in function of the signal to noise ratio:

$$\gamma_{\text{noise}} = \frac{1}{\sqrt{1 + \frac{1}{\text{SNR}_1}} \sqrt{1 + \frac{1}{\text{SNR}_2}}} \tag{4.12}$$

where SNR_i is the signal to noise ratio of the i-th channel. The estimated SNR in the present analysis is above 30 dB for each channel in the worst case–that is in the meadow ROI, which has a shallow look angle and hence lower backscattered intensity–and the backscattering variations over time are in the order of a few decibel at most, as shown in the results section 4.3.

The most important coherence factors in a repeat-pass interferometric acquisition setup are volume and temporal coherence. A generic model for the temporal decorrelation has been presented in [29]. In the hypotheses that within the resolution cell the distribution of the scatterers is homogeneous along range and azimuth and that their movements are independent and identically distributed, the temporal coherence can be expressed as [29]:

$$\gamma_{\text{temp}} = \frac{\iint \rho(z) \exp\left\{-j\frac{4\pi}{\lambda} d_r\right\} p_r(d_r, z) \mathrm{d}z \, \mathrm{d}d_r}{\int \rho(z) \mathrm{d}z} \tag{4.13}$$

where $\rho(z)$ is the average backscatter density, z is the vertical coordinate inside the resolution cell, d_r is the displacement of the scatterers along the line of sight, $p_r(d_r, z)$ is the probability distribution function of the scatterers displacement. If we assume that the movement of the scatterers follows a zero-mean Gaussian distribution with variance $\sigma_r^2(z)$ along the line of sight, then from Eq. (4.13) it follows [29]

$$\gamma_{\text{temp}} = \frac{\int \rho(z) \exp\left\{-\frac{1}{2}\left(\frac{4\pi}{\lambda}\right)^2 \sigma_r^2(z)\right\} \mathrm{d}z}{\int \rho(z) \mathrm{d}z} \tag{4.14}$$

which, with the additional assumption that the scatterers are uniformly distributed along z, leads to the commonly used exponential model for the temporal coherence [3, 29]

$$\gamma_{\text{temp}} = \exp\left\{-\frac{1}{2}\left(\frac{4\pi}{\lambda}\right)^2 \sigma_r^2\right\} \tag{4.15}$$

The scatterers variance can be modelled as the sum of two terms: a quasi-instantaneous term related to the effect of quick variations within the resolution cell (e.g. due to wind speed) and a time dependent

component related to long-term effects (e.g. vegetation growth) [7]:

$$\sigma_r^2 = \sigma_{r,\text{short}}^2 + \varsigma_{r,\text{long}}^2 \cdot t \tag{4.16}$$

Note that $[\sigma_r^2] = m^2$ (the dimension of the scatterers variance is square metres) and $[\varsigma_{r,\text{long}}^2] = m^2/s$. By substituting Eq. (4.16) in Eq. (4.15) it yields:

$$\gamma_{\text{temp}}(t) = \gamma_{\text{temp,short}} \cdot e^{-t/\tau} \tag{4.17}$$

where

$$\gamma_{\text{temp,short}} = \exp\left\{-\frac{1}{2}\left(\frac{4\pi}{\lambda}\right)^2 \sigma_{r,\text{short}}^2\right\} \tag{4.18}$$

and

$$\tau = \frac{2}{\varsigma_{r,\text{long}}^2}\left(\frac{\lambda}{4\pi}\right)^2 \tag{4.19}$$

The analysis conducted in this work is mainly focused on the short-term coherence. To reduce the impact of the long-term effects, we analysed interferograms calculated using various primary acquisitions in order to have a range of interferometric pairs with short temporal baselines over the entire time-series.

Volume coherence is caused by the penetration of the radar signal into the medium and is an important factor in forested areas. A simple model for the volume decorrelation has been reported in [30]:

$$\gamma_{\text{vol}} = \frac{1}{\sqrt{1 + \left(\frac{2\pi l_p \sqrt{\epsilon_r} B_\perp}{r\lambda\tan\theta}\right)^2}} \tag{4.20}$$

where ϵ_r is the real part of the dielectric constant and l_p indicates the penetration length inside the medium, defined as the length at which the signal power decreases $1/e$ of its value at the medium's surface. The values of l_p and ϵ_r are largely affected by the forest density and by changes in the vegetation water content [31, 32]. Nevertheless, Eq. (4.20) highlights that the volume coherence is 1 (no decorrelation) in case of zero perpendicular baseline and therefore we can expect a low sensitivity to volume decorrelation effects.

For the analysis of the temporal variation of the coherence, we calculated the average interferometric coherence (magnitude) inside each ROI and the associated standard deviation, which gives an indication of the coherence variations within the ROIs. The same approach was used for the interferometric phase.

4.3 Results

The results of the SAR/DInSAR temporal analysis are herein presented. First, the auxiliary weather data of the near-by weather stations are presented in order to set the *a priori* knowledge of the temporal variations of wind, temperature, relative air humidity, and precipitation in the time interval relevant to the

SAR acquisitions. The weather parameters are then used to find patterns with the temporal variations of the SAR observables (backscattering, coherence, and phase) along the time series.

VV- and HH-polarized backscattering time-series are shown in Section 4.3.2. An overview of the coherence achieved in the imaged area is provided by the coherence maps shown in Section 4.3.3, while the time-series of the average interferometric coherence (magnitude) and phase in the ROIs is reported in Section 4.3.4. Finally the empirical cumulative distribution function of the coherence in each ROI is reported in Section 4.3.5.

4.3.1 Auxiliary weather data

The measurements of the weather parameters provided by the different stations of the SwissMetNet network over the period of interest (Nov. 5 to Nov. 20, 2018) are plotted in Figs. 4.3, 4.4, and 4.5.

Compared to the other days of the acquisitions period, a higher wind speed was measured on Nov. 6, with peaks of average wind speed up to 3.3 m/s measured in an interval in which radar acquisitions were performed (see Fig. 4.11c).

Rainfalls were detected on Nov. 13, partially on Nov. 14, and on Nov. 19.

The relative air humidity often reaches saturation (100 %) during the nights as a consequence of the air temperature cooling down to the dew point temperature. High values of relative air humidity indicate moist air and, at saturation, formation of dew on surfaces and vegetation canopies can occur [33]. The amount of water vapour in the air is a function of temperature and pressure, with less water vapour corresponding to lower temperatures. At temperatures below 0°C, frost can form.

The measurements report a high level of relative air humidity during most periods of interest (that is close to or during the radar acquisitions). The lowest relative air humidity values were measured on Nov. 6, when the relative air humidity was between 30% and 60%. On Nov. 7 the relative air humidity shows a steady decrease from 100% to 60% between 08:00 and 17:00. A high level of relative air humidity was also measured on Nov. 8 (between 72% and 84%), Nov. 14 (between 96% and 100%), Nov. 15 (between 87% and 100%), Nov. 19 (between 75% and 96%), and Nov. 20 (between 80% and 100%).

4.3.2 Backscattering

Fig. 4.6 shows the time-series of the (spatial) average backscatter intensity from each ROI. As the radar channels are not radiometrically calibrated, the backscatter cannot be directly linked to the normalised radar cross section. Therefore, only the relative values with respect to the mean temporal backscatter intensity of each ROI are reported. The acquisitions are HH polarized in Fig. 4.6a and VV polarized in Fig. 4.6b. A multilooking of 20m × 40m (range × azimuth) was applied before spatial averaging within the ROI.

Larger backscatter variations can be noted throughout Nov. 6, with average peak-to-peak values of 3.5 dB for the meadow ROI, 0.7 dB for the trees2 ROI, 0.6 dB for the trees1 ROI, and 0.3 dB for the rocky one. The backscatter variations over time seem to correlate with the average wind speed, with larger variations in correspondence of the stronger wind interval (between 11:00 and 15:00). It is worth highlighting
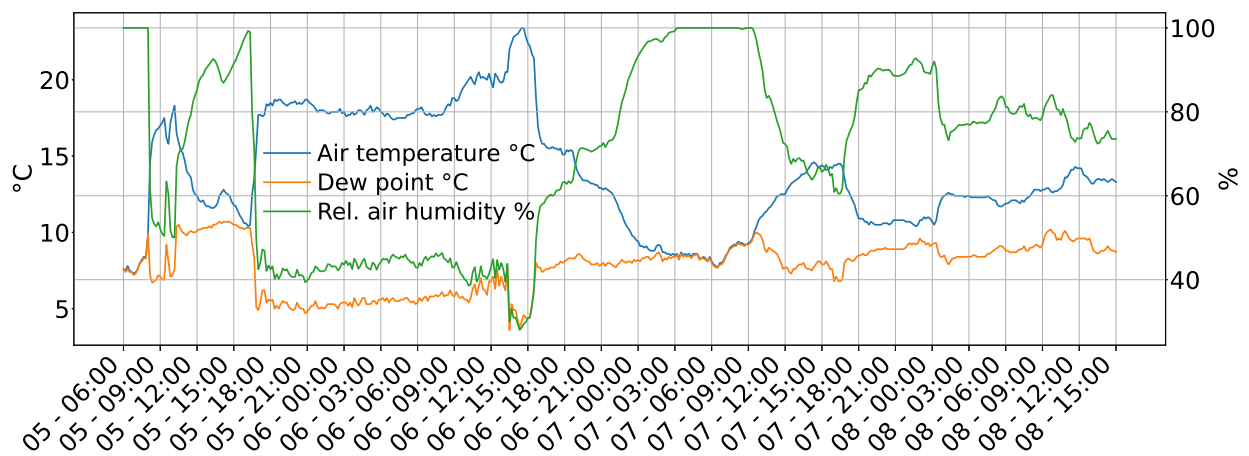
(a) Temperature, dew point, and relative air humidity
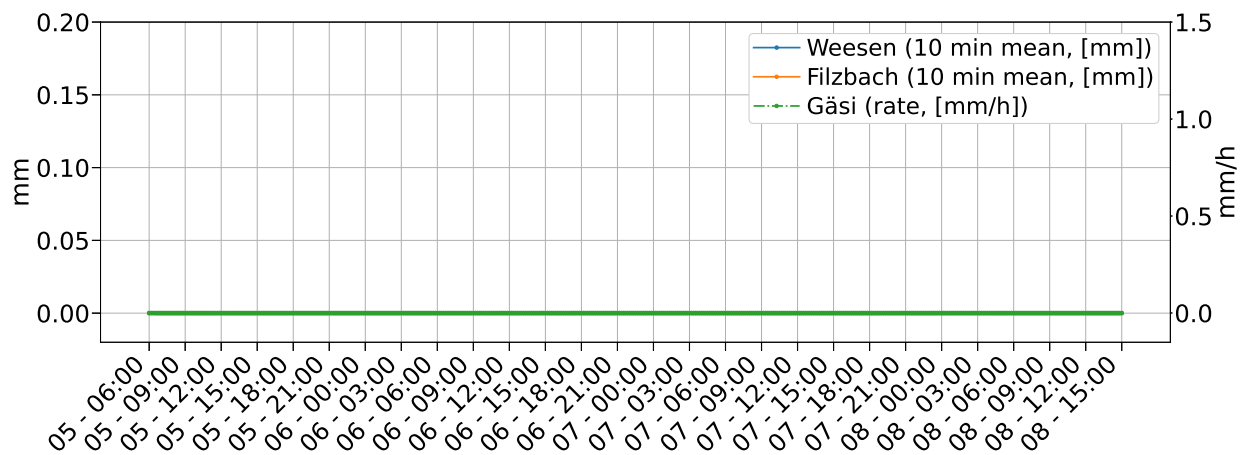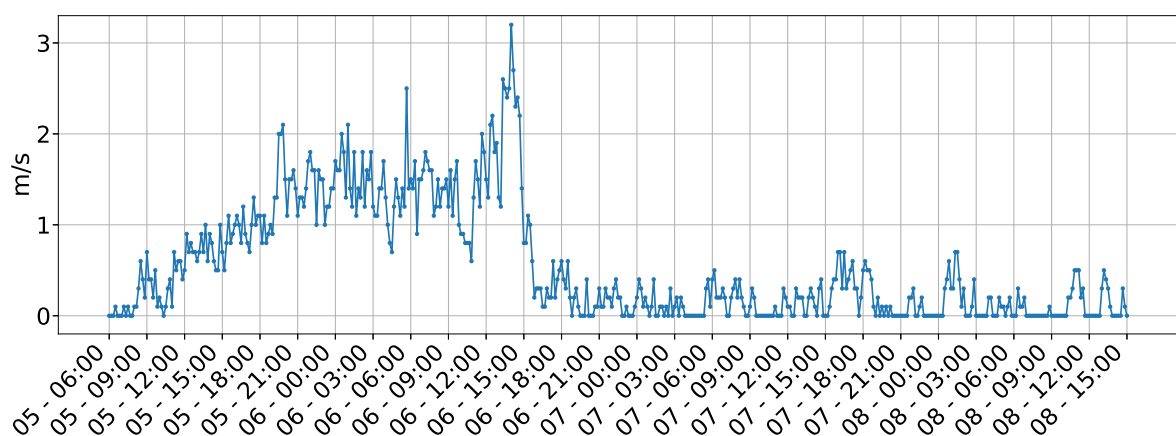
(b) Precipitation

(c) Wind speed

Figure 4.3: Weather data relevant to Nov. 5–8, 2018.
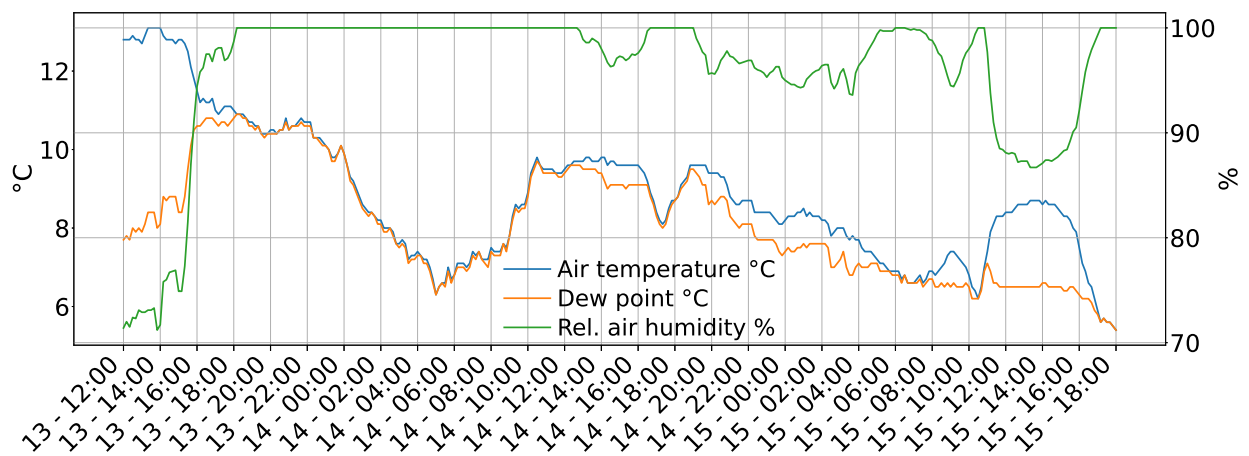
(a) Temperature, dew point, and relative air humidity
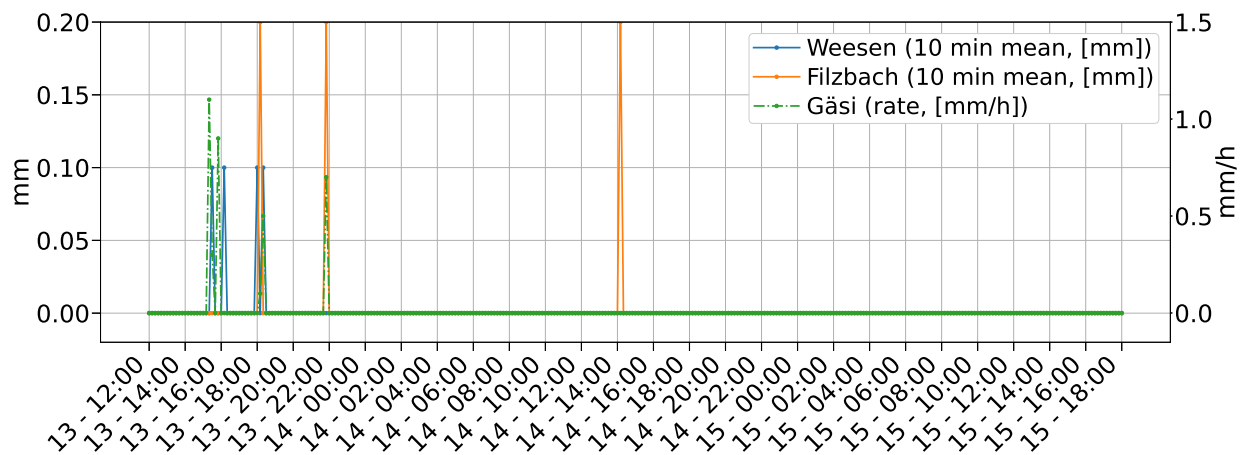
(b) Precipitation
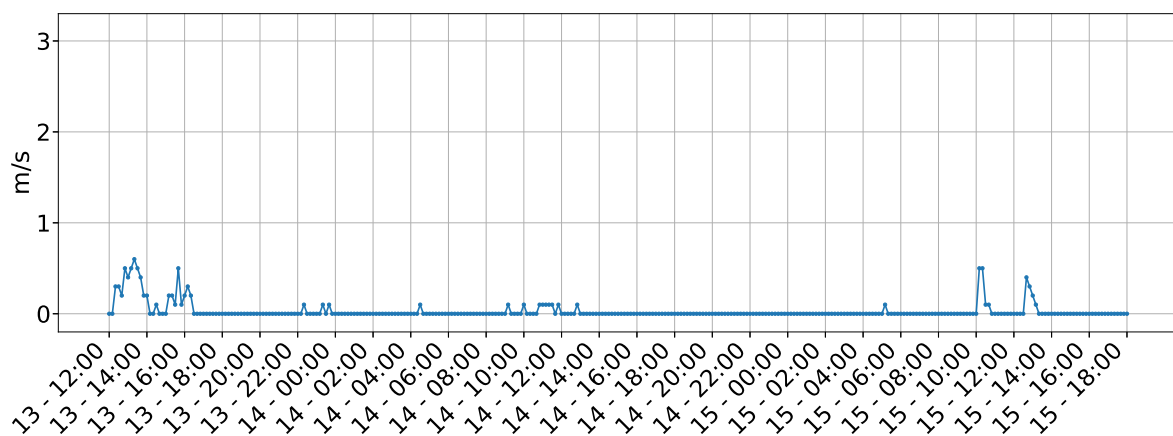
(c) Wind speed

Figure 4.4: Weather data relevant to Nov. 13–15, 2018.

(a) Temperature, dew point, and relative air humidity

(b) Precipitation

(c) Wind speed
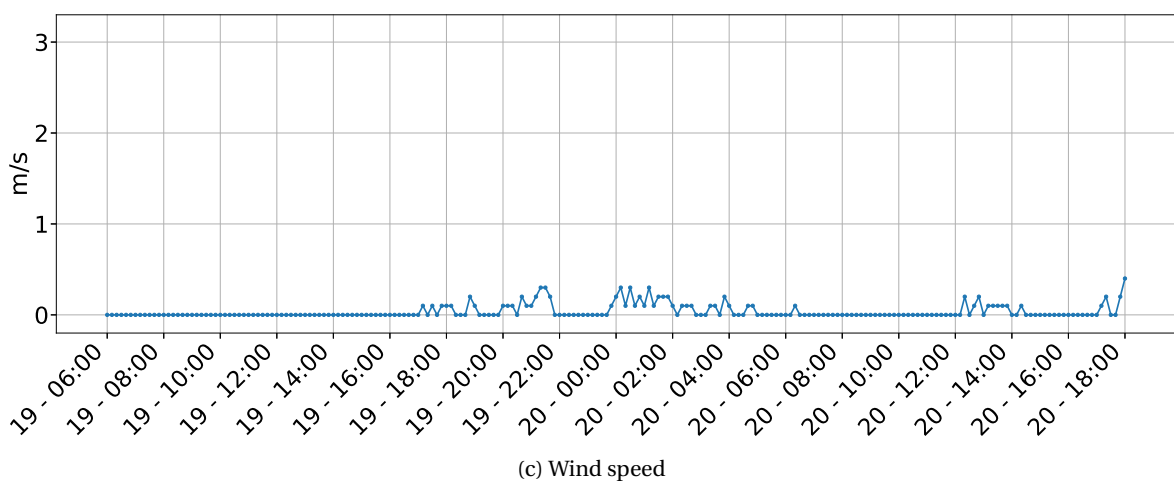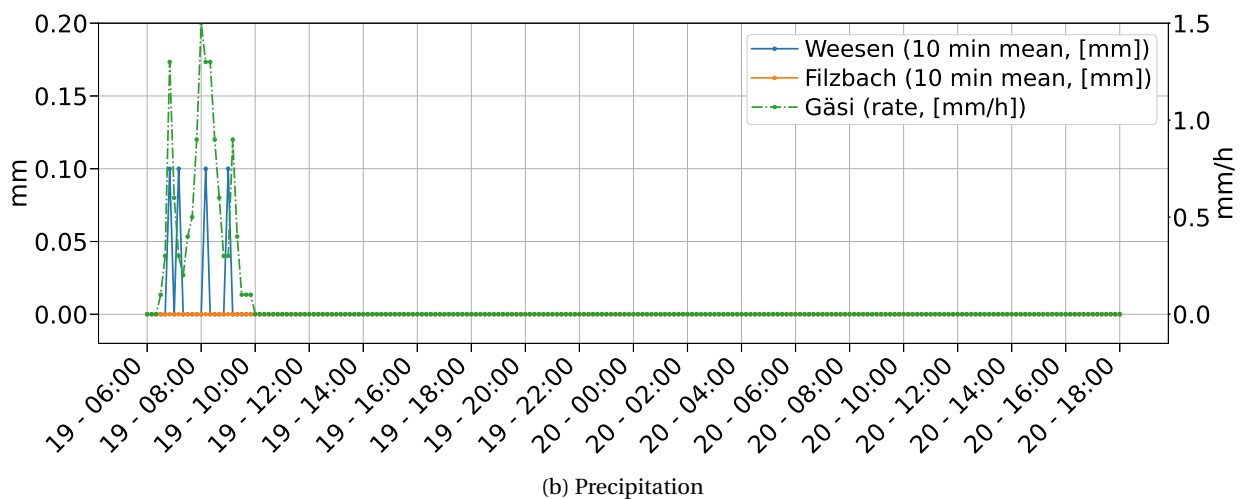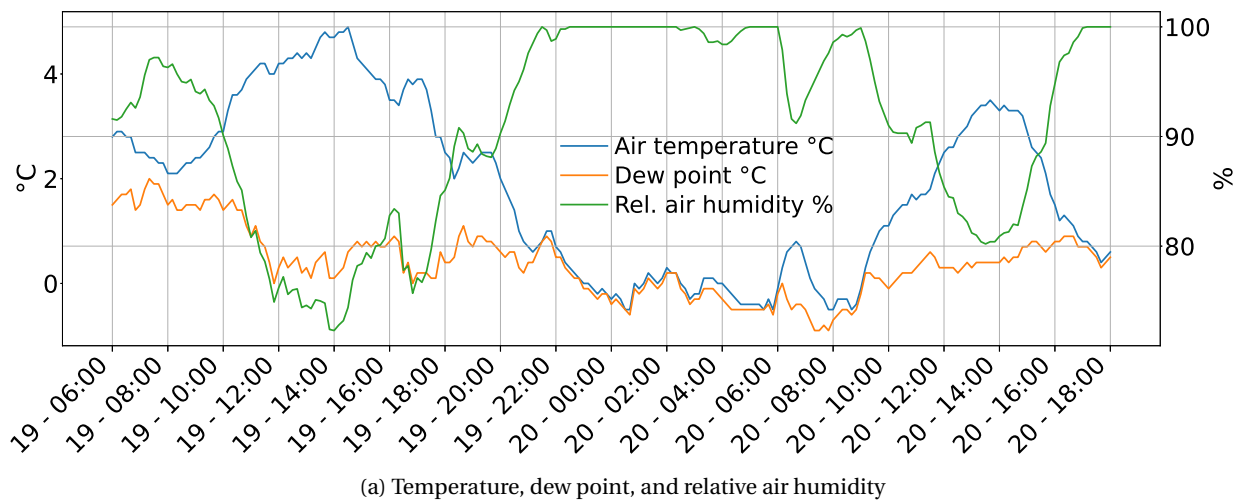
Figure 4.5: Weather data relevant to Nov. 19–20, 2018.
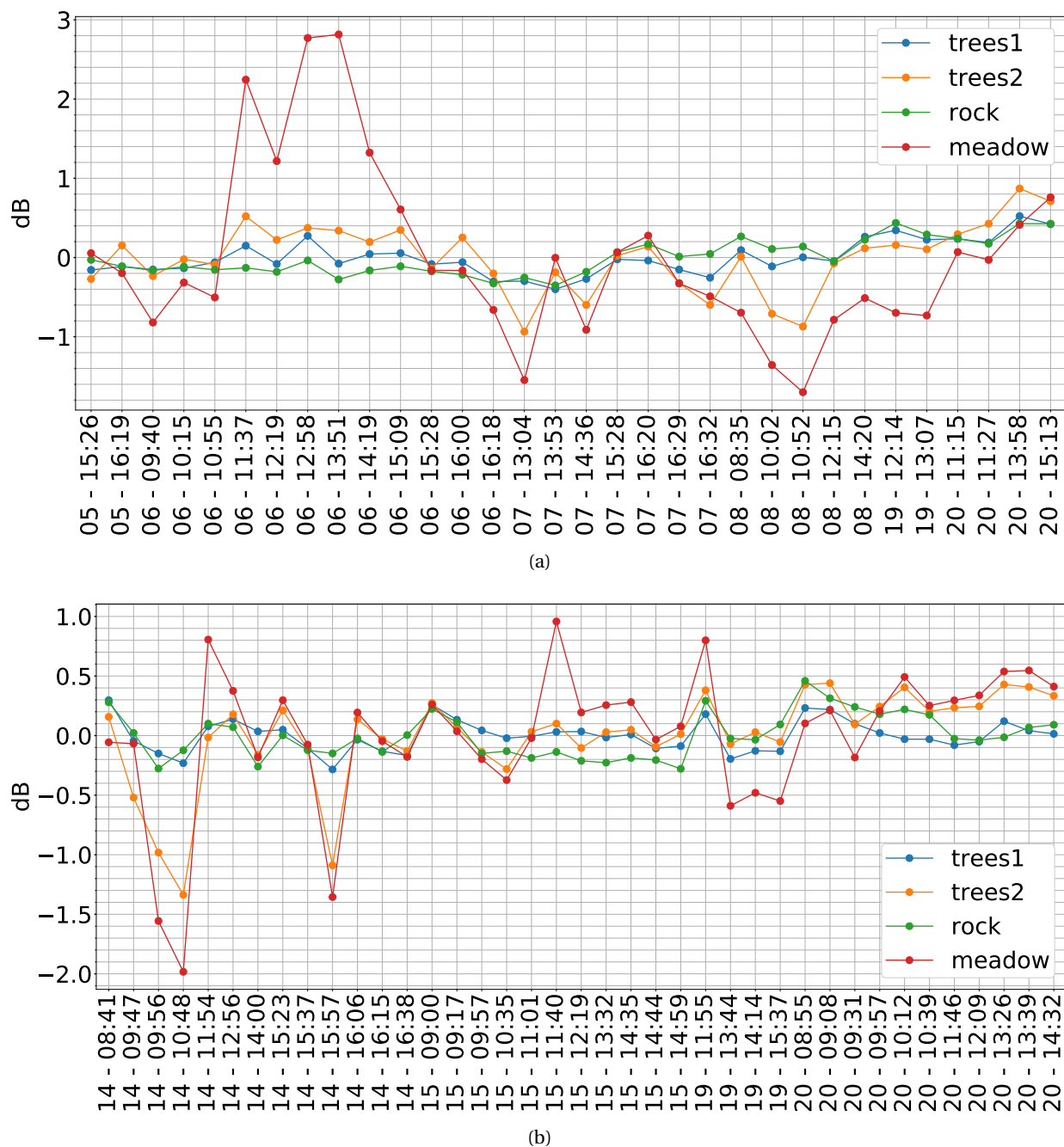
Figure 4.6: Relative average backscatter time-series of L-band car-borne SAR acquisitions of four different land covers. For each ROI, the variation with respect to the temporal mean of the spatially averaged backscatter intensity is plotted. A multilook of 20m × 40m is applied. (a): 32 HH polarized acquisitions from Nov. 5 to Nov. 20. (b): 39 VV polarized acquisitions from Nov. 14 to Nov. 20.

that small vegetated spots are also present in the rocky area, as it can be observed in the optical image in Fig. 4.1c.

From Nov. 7 until Nov. 20, a trend towards a higher relative average backscatter can be noted in the rocky and the trees1 ROIs resulting in an increase of the relative average backscatter value of 0.67 dB and 0.75 dB, respectively (from Nov. 7 at 13:04 to Nov. 20 at 15:13). A less regular but still clear trend is also noticeable in the trees2 and the meadow areas, for which the peak-to-peak variation in the same time span (Nov. 7–Nov. 20) is about 1.7 dB and 2.3 dB, respectively. A more regular backscatter increase for the trees2 and the meadow areas is visible from Nov. 8 (at 10:52) to Nov. 20.

Similar observations can be done for the relative average backscatter of the VV acquisitions in the time span Nov. 14–20. The meadow area shows the larger variability over time compared to the other ROIs, followed by the adjacent trees2 area, particularly on Nov. 14. The trees1 and the rocky ROIs show more contained backscatter variations.

A clear backscatter increase affecting all ROIs can be noted in the transition from Nov. 15 to Nov. 19 and more markedly from Nov. 19 to Nov. 20.

4.3.3 Coherence maps mosaic

The results related to the interferometric coherence are now presented. In the following, for the sake of simplicity, the expression "the interferogram of <date>" will be used to intend "the interferogram with secondary acquisition acquired at date <date>". The primary acquisition of the interferometric pair will be explicitly reported when necessary to avoid ambiguity.

Fig. 4.7 shows a set of interferometric coherence maps relevant to the HH-polarized acquisitions with a maximum temporal baseline of 15 days (from Nov. 5 to Nov. 20) while Fig. 4.8 shows the coherence maps relevant to the VV-polarized acquisitions with a maximum temporal baseline of 6 days from Nov. 14 to Nov. 20. The brightness of each coherence map is modulated by the spatially multilooked and temporally averaged radar backscatter intensity image. The temporal average of a set of SAR images has the advantage of improving the radiometric resolution without worsening the spatial resolution.

In large parts of the imaged area the coherence remains visibly high for the entire 15-days period, especially on rocky and urban areas. Vegetated and partially vegetated areas also retain a good level of coherence but are subject to larger temporal and spatial coherence variations.

Large coherence variations can be observed in the interferograms of Nov. 6 (Fig. 4.7) in the vegetated areas, for which major coherence losses are then followed by coherence gain even within the same day. This is visible, for example, by comparing the coherence maps with secondaries between 11:37:02 and 15:28:48 with the ones at 16:00:21 and 16:18:16.

In both the HH and the VV polarized interferograms, decorrelation patterns can be observed in the interferograms of Nov. 19. The decorrelation is visible for the 1 day and the 14 days temporal baseline (Figs. 4.8 and 4.7, respectively), particularly in the upper-left part of the imaged area.

Figure 4.7: Interferometric coherence maps. Primary acquisition: Nov. 05, 2018, 15:26:11. Polarization HH. The acquisition times of the secondaries are reported on top of each map in the format yyyym-mdd_hhmmss. The brightness is modulated by the spatially multilooked and temporally averaged radar backscatter intensity image.
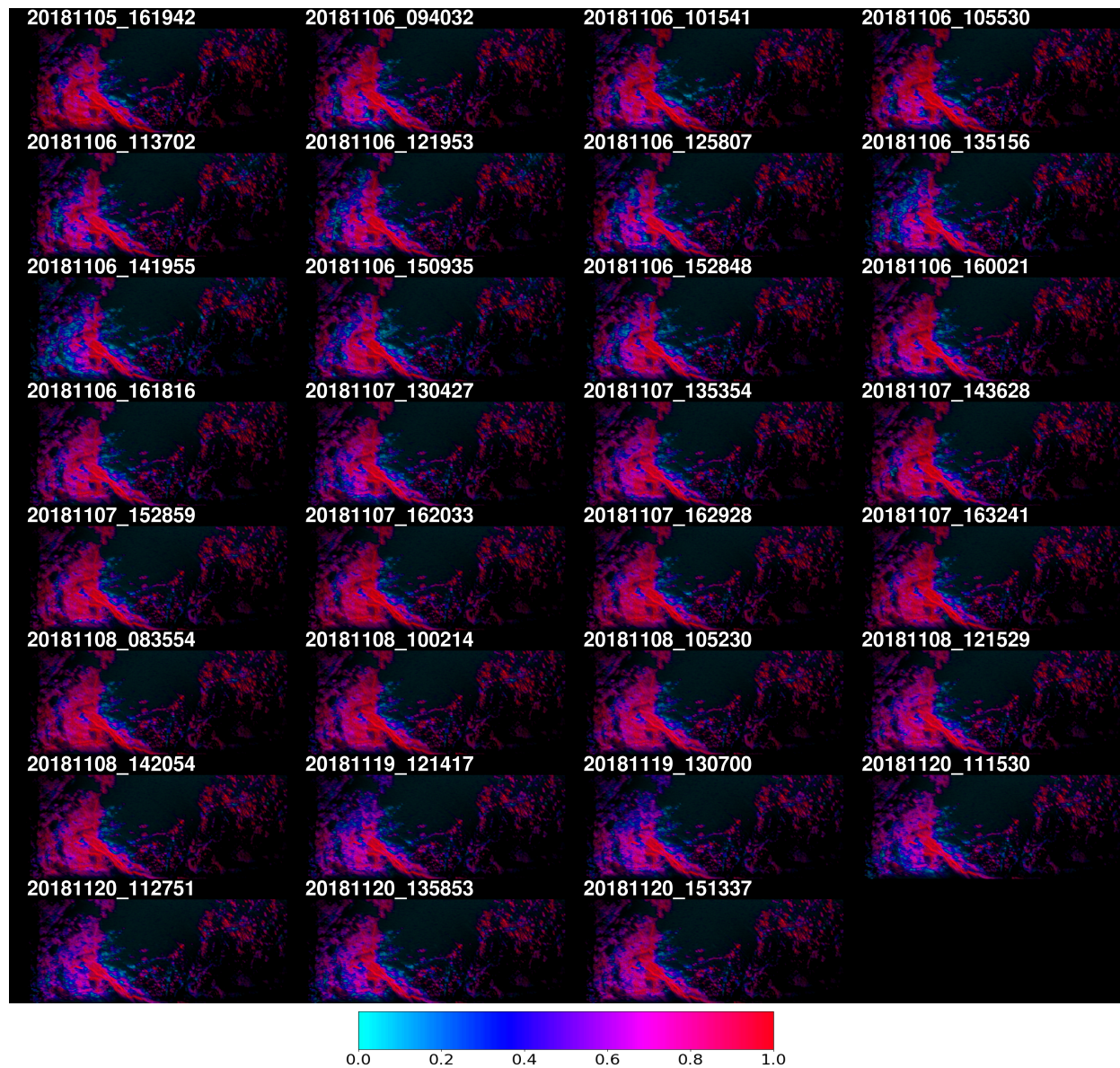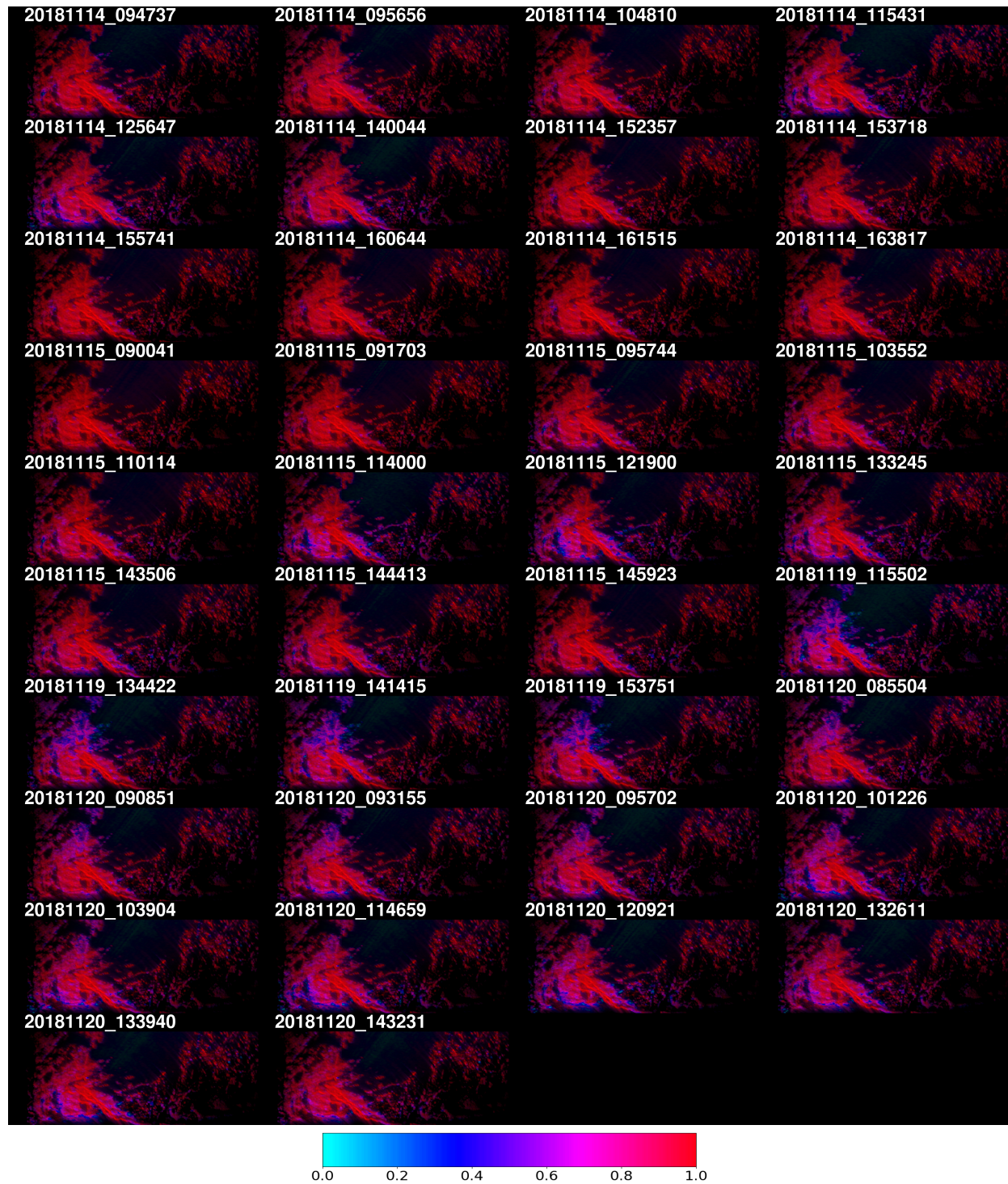
Figure 4.8: Coherence maps. Primary acquisition: Nov. 14, 2018, at 08:41:36. VV polarization. The acquisition times of the secondaries are reported on top of each map in the format yyyymmdd_hhmmss. The brightness is modulated by the spatially and temporally multilooked radar backscatter intensity image.

4.3.4 Interferometric coherence and phase time-series

Fig. 4.9 shows the average interferometric coherence and phase calculated in the 4 ROIs. For each time-series, a single common primary acquisition was used to form the differential interferograms. Day and time of the secondary acquisitions are reported on the abscissa axes. The vertical error bars extend over a 2σ interval, where σ is the standard deviation indicating the spatial variation within each area. Larger values of the standard deviation indicate larger differences between the two acquisitions within the same area.

In all time-series the rocky ROI shows an average coherence above 0.9 for most interferograms, with minor oscillations and small standard deviations. Two outliers can be noted, namely the interferograms of Nov. 6 at 12:58 and the one of Nov. 8 at 10:52. The average phase is roughly stable around 0 with standard deviation below 0.1 rad for the entire time-series even for the temporal baseline of 14 days (Figs. 4.9b and 4.9h), with the exclusion of the first two interferograms of Nov. 5 showing a maximum deviation from zero of about 0.4 rad with standard deviation of 0.25 rad (cf. 4.9e).

In the vegetated ROIs (trees1, trees2, and meadow) the coherence is generally smaller than in the rocky area and the standard deviation is about 4–6 times larger. For a temporal baseline of about two weeks, the coherence reaches values around 0.65–0.8 in the two forested ROIs and 0.5–0.55 in the meadow one (see for example the interferograms of Nov. 7 in Fig. 4.9g). Higher coherence values can be observed in the VV-polarized case (Figs. 4.10) where, with temporal baselines of 6 days, the coherence is between 0.8 and 0.9 in the vegetated areas. Also in this case, the coherence is slightly lower in the meadow area, although the difference with the other areas is less marked.

In function of the primary acquisition used for the interferometric time-series, coherence and phase values vary, which is expected as the interferometric measurements reflect relative changes between the primary and the secondary acquisitions. Nevertheless, recurring patterns can be observed in all time-series. Particularly noticeable are the transient decorrelation patterns of the interferograms of Nov. 6 and Nov. 19, visible in each time-series.

November 6 The interferograms of Nov. 6 show a U-shaped decorrelation pattern in the meadow and in the trees2 areas, where the coherence drops by about 30%–40% in a time span of less than one hour (from 10:55 to 11:37), further decreases until 14:19, and then gradually increases again up to about the initial level at 16:00–16:18. In the same time span, the trees1 ROI shows a less regular decorrelation trend and a generally higher average coherence. Nevertheless, sharp coherence variations are observable until 15:09 also in the trees1 area.

As in the case of the backscatter, the decorrelation pattern in the vegetated areas appears correlated with the average wind speed measured on Nov. 6, which has lower values in the morning until 11:00 and in the afternoon after 15:30, and stronger values between 13:30 and 14:30 (above 3 m/s on average). This is better visible in Fig. 4.11 showing the wind data along with the coherence and the phase time-series limited to the Nov. 6 interferograms created using a primary acquired on the same day during a period of low wind speed (below 0.5 m/s), as done in Figs. 4.9a and 4.9b.

(a) Coherence. Primary: Nov. 6, 2018, at 16:18:16

(b) Phase. Primary: Nov. 6, 2018, at 16:18:16

(c) Coherence. Primary: Nov. 7, 2018, at 15:28:59

(d) Phase. Primary: Nov. 7, 2018, at 15:28:59

(e) Coherence. Primary: Nov. 8, 2018, at 12:15:29

(f) Phase. Primary: Nov. 8, 2018, at 12:15:29

(g) Coherence. Primary: Nov. 20, 2018, at 15:13:37

(h) Phase. Primary: Nov. 20, 2018, at 15:13:37

Figure 4.9: Time series of average differential interferometric coherence and phase in different land covers, from Nov. 5 to Nov. 20, using four different primaries (indicated in the caption below the figures). Acquisitions polarization is HH. The abscissa axes indicate the day and time of the secondary acquisitions (in the format day-HH:mm). The error bars extend over a 2σ interval, where σ is the (coherence or phase) standard deviation calculated in each ROI. For all ROIs the level of coherence is mostly above 0.5 with worse results in the meadow area. Decorrelation patterns triggered by higher wind speed on Nov. 6 and by a rainfall on Nov. 19 are visible.

(a) Coherence. Primary: Nov. 14, 2018, at 08:41:36

(b) Phase. Primary: Nov. 14, 2018, at 08:41:36

(c) Coherence. Primary: Nov. 20, 2018, at 14:32:31

(d) Phase. Primary: Nov. 20, 2018, at 14:32:31

(e) Coherence vs. temperature. Primary: Nov. 14 at 08:41:36.

(f) Coherence vs. relative air humidity. Primary: Nov. 14 at 08:41:36

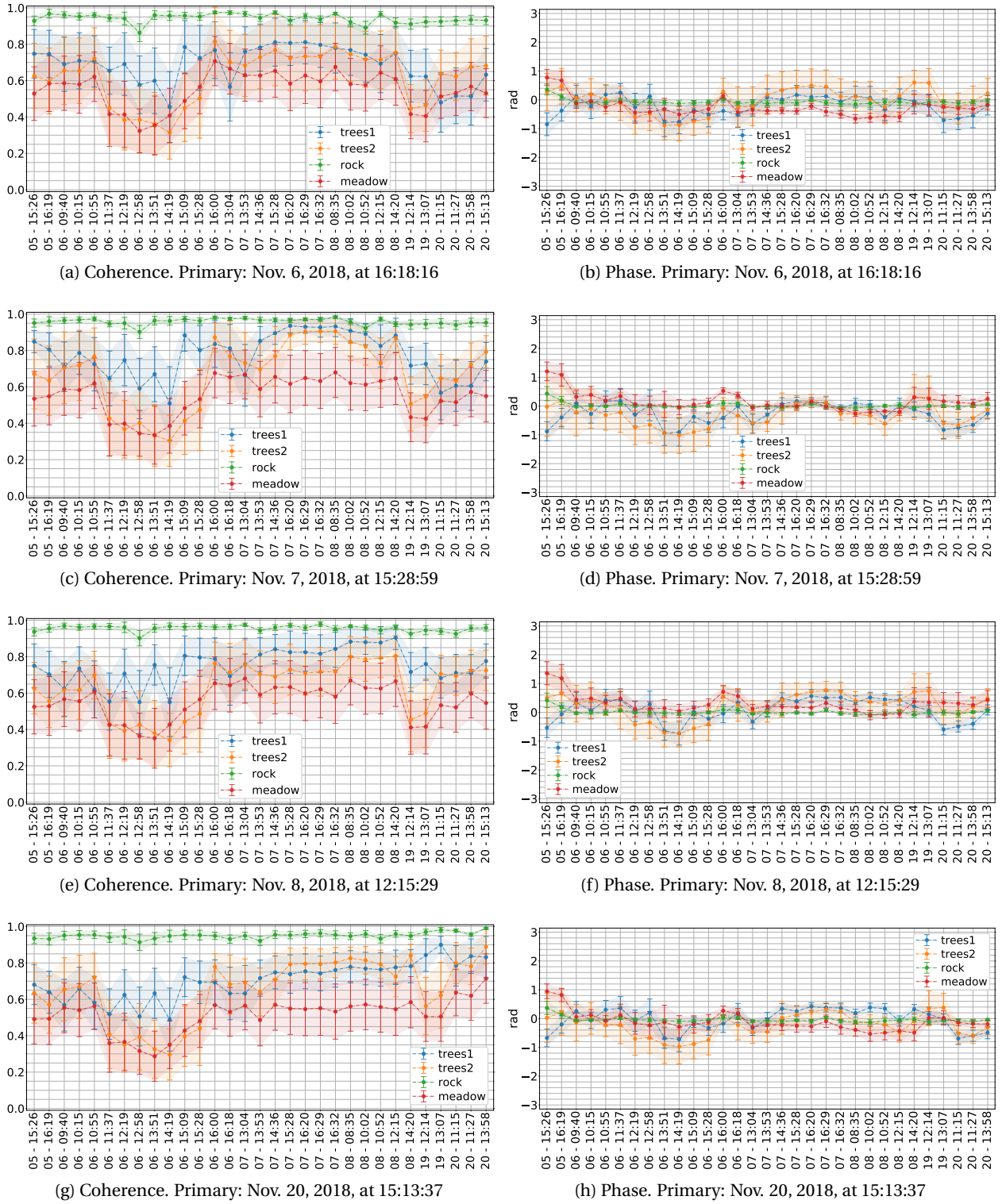Figure 4.10: (a)–(d): Time series of average differential interferometric coherence and phase in different land covers, from Nov. 14 to Nov. 20, using two different primaries. Acquisitions polarization is VV. The abscissa axes indicate the day and time of the secondary acquisitions (day-HH:mm). The error bars extend over a 2σ interval, where σ is the standard deviation in each ROI. Decorrelation patterns due to the effect of the rain on Nov. 19 are visible. Rainfalls were measured also on Nov. 13 and, at one of the weather stations, on Nov. 14 around 14:00 (see Figs. 4.4 and 4.5). (e)–(f) scatter plots of coherence values against temperature and relative air humidity, calculated using all the secondary VV-pol acquisitions of Nov. 2018. A regression line is added for reference. The shaded bands indicate a 95% confidence interval and the parameter r is the Pearson correlation coefficient.

(a) Coherence

(b) Phase

(c) Wind speed

(d) Temperature, dew point and relative air humidity
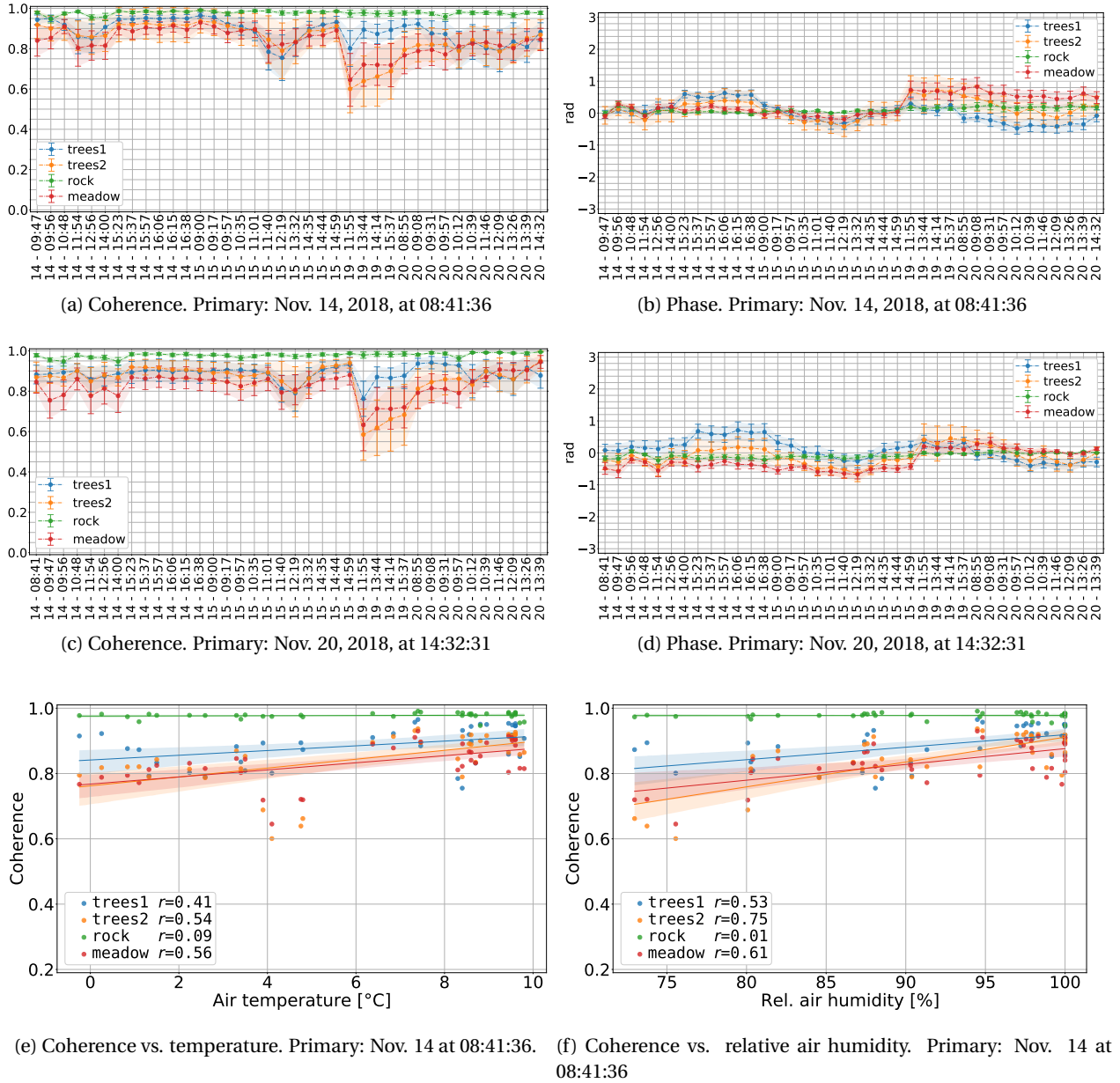
(e) Coherence vs. wind speed

(f) Coherence vs. relative air humidity
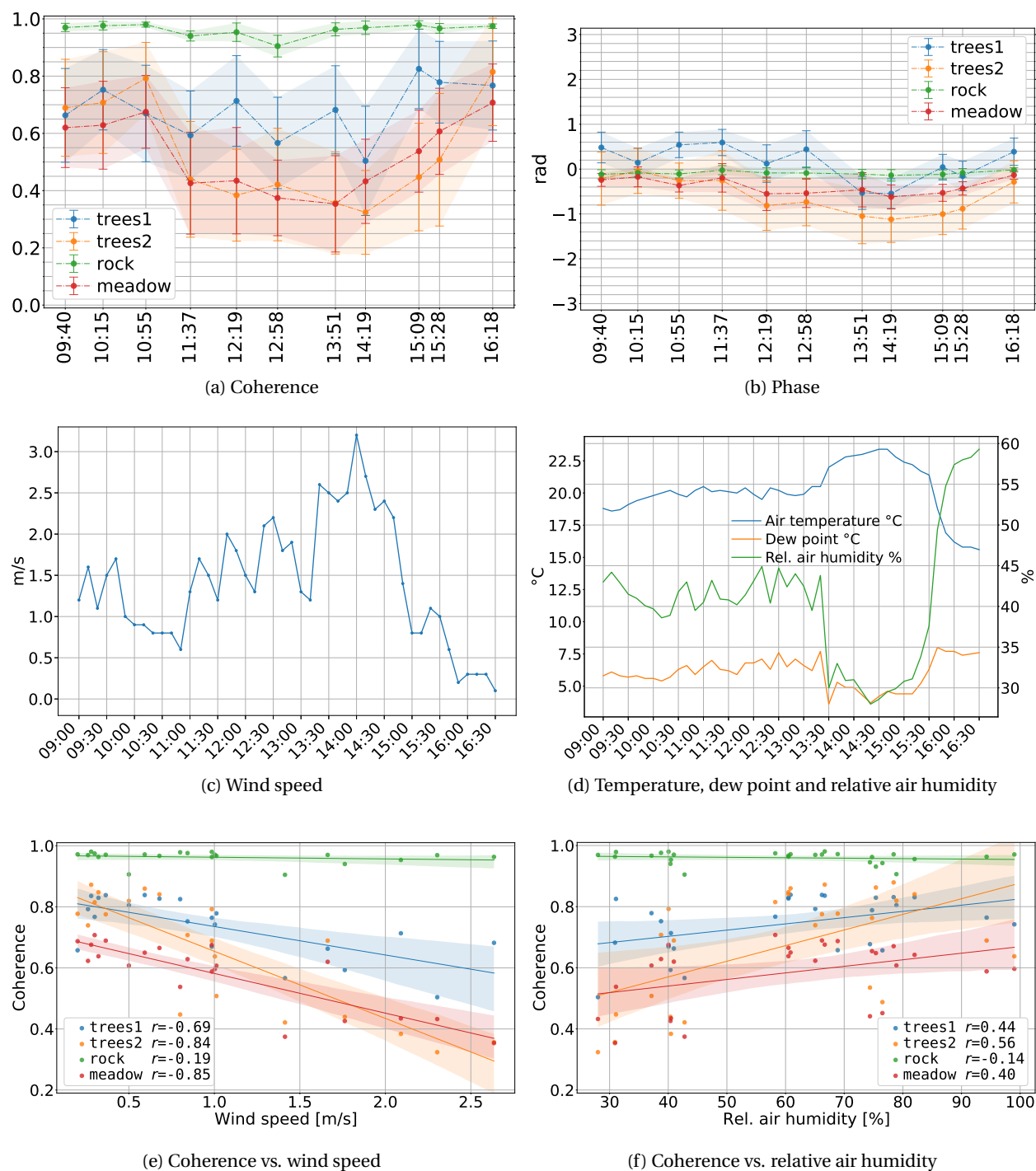
Figure 4.11: (a)–(b): Time series of average differential interferometric coherence and phase in different land covers for the acquisitions on Nov. 6, during higher wind speeds intervals. Primary acquisition: Nov. 6, 2018, at 16:00. Secondary acquisitions spanning about 6.5 hours (time reported on the abscissa). Polarization HH. The error bars extend over a 2σ interval, where σ is the standard deviation within each ROI. (c)–(d): weather data relevant to Nov. 6. (e)–(f) scatter plots of coherence values against wind speed and relative air humidity, calculated using all the secondary HH-pol acquisitions of Nov. 2018. A regression line is added for reference. The shaded bands indicate a 95% confidence interval and the parameter r is the Pearson correlation coefficient. A negative correlation between coherence and wind speed is visible in the vegetated areas. In (f) the larger spread of data points does not suggest a clear linear relation between the coherence in the vegetated areas and the relative air humidity. In the rocky area the data points are better aligned and indicate almost no correlation.

Figs. 4.11e and 4.11f show the scatter plots of the coherence against the wind speed and the relative air humidity, respectively. The coherence shows a negative correlation with the wind speed in all three vegetated areas, while almost no correlation is visible in the rocky one. The relation between coherence and relative air humidity is less apparent. The larger spread of data points does not suggest a clear linear relation between the coherence in the vegetated areas and the humidity. In the rocky area, the data points align along the linear regression line with slope around zero, indicating almost no correlation. A stronger correlation between coherence and relative air humidity can be observed in Fig. 4.10e for the vegetated areas, where it must be noted that the level of relative air humidity measured in correspondence of the primary acquisition used for the computation of the interferometric coherence was high (100%).

(a) Coherence. Primary: Nov. 06, 2018, at 14:19:55

(b) Phase. Primary: Nov. 06, 2018, at 14:19:55

(c) Coherence. Primary: Nov. 19, 2018, at 13:44:22

(d) Phase. Primary: Nov. 19, 2018, at 13:44:22
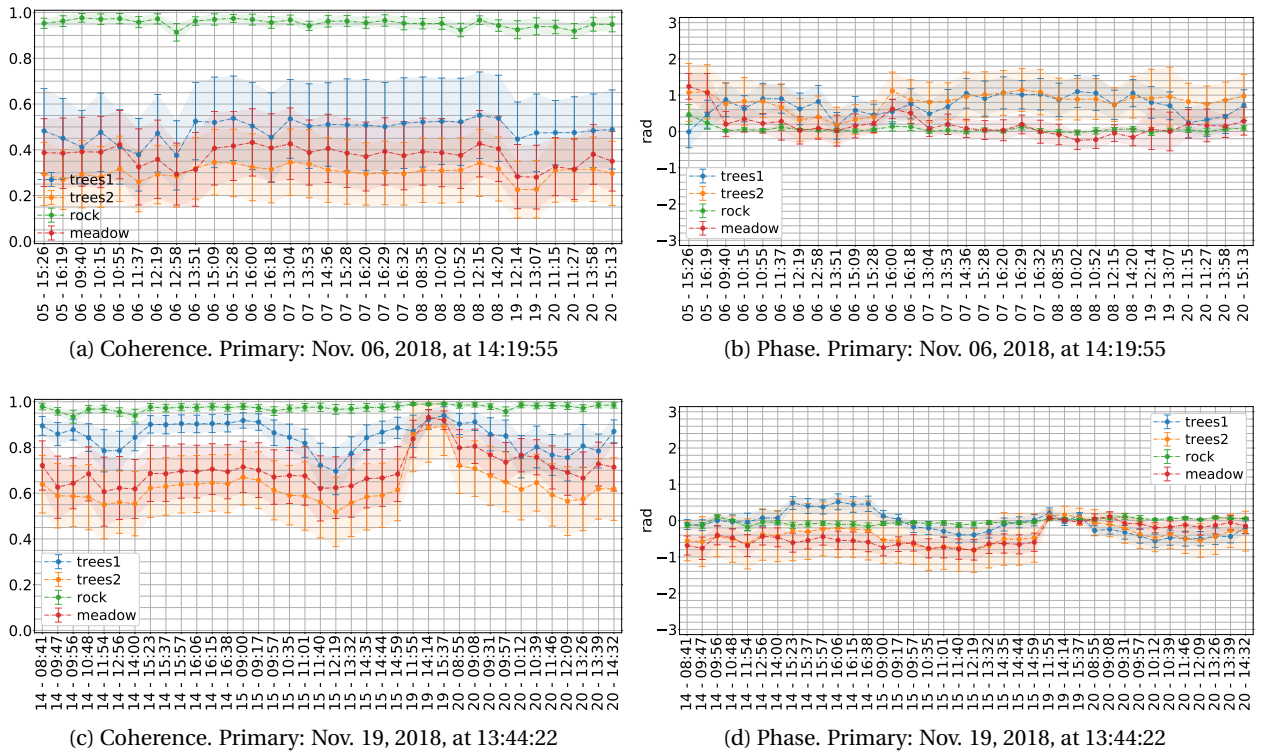
Figure 4.12: Time series of average differential interferometric coherence and phase in different land covers. (a) and (b): (HH polarized) primary acquired on Nov. 06, 2018, at 14:19:55, during a period of relatively higher wind speed as compared to the other days. Similar results achieved using any acquisition between 11:00 and 15:00 of Nov. 6 as primary. (c) and (d): (VV polarized acquisitions) primary acquired on Nov. 19, 2018, at 13:44:22, about 3 hours after a rainfall.

The average phase of the interferograms of Nov. 6 shows a persistent deviation from zero over time during higher wind speed intervals, also for the trees1 area that retains a higher coherence. The phase deviations tend to fade out during calm wind periods, assuming similar values in the afternoon as in the morning (compare the average phase for the secondaries at 09:40 and at 16:18 of Nov. 6 in Fig. 4.11b). The phase deviation is less prominent on the meadow, with a peak-to-peak deviation in the order of 0.5 rad compared to the 1 rad or more (depending on the primary) of the trees1 and trees2 areas.

The time-series in Fig. 4.12a and 4.12b use a SAR image acquired during higher wind speed as primary

(Nov. 6 at 14:19). Although only two hours separate this primary from the one used in Fig. 4.9a (for which the primary is at 16:18), in this case only the rocky area retains high coherence (average around 0.9 with a low standard deviation). For the vegetated areas, the average coherence is much lower compared to the other time-series of Fig. 4.9, even for interferometric pairs with short temporal baseline (e.g. for the secondaries at 13:51 and 15:09). Amongst the vegetated ROIs, the highest average coherence is achieved in the trees1 area, with a temporal mean of 0.48. The average coherence remains below 0.35 for the entire 15-days period in the trees2 ROI and is slightly higher in the meadow ROI (between 0.35 and 0.45). Similar results were obtained with primaries acquired within the time interval 11:37–13:51 of Nov. 6, corresponding to the period of higher wind speed.

Large phase variations can be observed in Fig. 4.12b throughout the time-series in all areas but the rocky one, particularly for increasing temporal baselines.

November 7-8   In different time-series, a progressively increasing coherence for the first interferograms of Nov. 7 (between 13:04–16:20) can be observed in the trees1 area, with both increasing and decreasing temporal baselines, while a coherence decrease on Nov. 8 can be observed in most time-series. A similar pattern can be observed also in the trees2 area in all time-series but the one with primary on Nov. 8. In both forested areas the level of coherence is mostly above 0.7 on average, with higher coherence relevant to baselines shorter than one day, i.e. in the interferograms with both primary and secondary on Nov. 7 or Nov. 8. The meadow area generally shows lower average coherence and larger standard deviation during both days. Small coherence variations (less than 0.5) can be observed also in the interferograms with 3 minutes difference in the temporal baseline (e.g. the ones at 16:29 and 16:32 on Nov. 7), but are less prominent when the primary is in the same day (Fig. 4.9c).

Using the primary of Nov. 20 (Fig. 4.9h) the phase standard deviation of the forested areas in the interferograms of Nov. 7 and Nov. 8 (12–13 days temporal baseline) is comparable or smaller than the one in the interferograms with the primary on Nov. 7 or Nov. 8 (between a few hours and up to 1 day temporal baseline) or with primary on Nov. 6 (Fig. 4.9b).

November 14-15   Coherence variations are visible on Nov. 14 until 15:23, whereas thereafter the coherence is rather stable in all areas. The varying correlation can be observed in the case of temporal baselines of a few hours in Fig. 4.10a (primary at 08:41 of Nov. 14) as well as in the case of the 6 days temporal baseline in Fig. 4.10c (primary at 14:32 of Nov. 20). Larger variations are visible in the meadow area, with a maximum coherence loss of 12% compared to the 6% loss in the two forested areas. Small coherence variations (below 3%) are also visible in the rocky area in the same time interval (from 8:41 to 14:00) and a small standard deviation increase is visible in correspondence of the interferograms at 09:56 and at 14:00, but the average coherence remains above 0.95. In the vegetated areas, the average coherence is around 0.8–0.85 during the decorrelating period and around 0.9–0.95 after 14:00 when the coherence stabilises, with slightly lower values obtained with the 6 days temporal baseline.

The phase time-series shows a clear signal in the trees1 area in the interferograms of Nov. 14 between 15:23 and 16:38 despite the high and stable coherence. The average phase deviation in the trees1 area is about 0.2–0.4 rad for the case with 6–7 hours of temporal baselines (Fig. 4.10b) and 0.6 rad in the

case of the 6 days temporal baseline (Fig. 4.10d). A smaller but still apparent phase deviation is also visible in the trees2 area during the same period and an increase of the standard deviation is visible in the longer temporal baseline case. Although no rain was visually observed in the target area during the acquisitions, one of the weather stations (Filzbach) measured a short rainfall on Nov. 14 around 14:10, which could be linked to such fading phase deviation.

During the time interval with unstable coherence (08:41–14:00) phase variations up to ±0.2 rad are visible in all areas including the rocky one. As shown in the weather data in Fig. 4.4 rainfalls affected the area the day before the acquisitions (Nov. 13) and to some extent on Nov. 14 (around 14:10). The difference in the measurement from the various stations suggests a spatial variability of the rainfalls in the area of interest. The high level of relative air humidity, at saturation or close to saturation throughout Nov. 14, indicates a high level of moist air. It is worth pointing out that, especially in consideration of the height variations of the imaged area, the actual values of temperature and relative air humidity in the ROIs might differ from those of the measurement stations.

The interferograms of Nov. 15 show a transient decorrelation pattern in all three vegetated areas, especially between 11:00 and 14:35, characterised by roughly 40%–50% increase of the standard deviation. Approximately in the same time span, the relative air humidity drops from 100% to below 90% (see Fig. 4.4a) A slightly smaller decorrelation is visible in the interferograms of Nov. 15 with the temporal baselines of about 5 days (Fig. 4.10d) as compared to case with temporal baseline of 1.5 days (Fig. 4.10b).

November 19-20 As mentioned in Section 4.3.1, a rainfall was reported during the morning of Nov. 19 one hour before the start of the acquisitions, as visible in Fig. 4.5. On Nov. 20 no rainfall but a high level of relative air humidity was reported from the weather measurement stations. With temperatures touching negative values during the night and the early morning of Nov. 20, frost formed in some parts of the target area, as visually confirmed by the whitish appearance during the first hours of Nov. 20.

The decorrelation observed in the coherence maps in the interferograms of Nov. 19 is discernible in the time-series of both HH-polarized and VV-polarized interferograms shown in Figs. 4.9 and 4.10, independently from the primary used. Only in the case of Fig. 4.9g, characterised by a short temporal baseline, the correlation increases in one of the forested areas (trees1) in the two HH-polarized interferograms of Nov. 19.

For the VV-polarized interferograms of Fig. 4.10 the coherence reaches its minimum on Nov. 19 at 11:55 in all vegetated areas. Despite the longer temporal baseline, in Fig. 4.10c (in which the temporal baseline increases from right to left) the trees2, the meadow, and partially the trees1 areas have higher coherence in the interferometric pairs Nov. 20–15 (primary–secondary) than in the Nov. 20–19 and, to some extent, in the Nov. 20–20 ones.

The decorrelation in the Nov. 19 interferograms appears stronger when the secondary acquisition is temporally closer to the end of the rainfall event (i.e. at 12:14 for the HH interferograms and at 11:55 for the VV interferograms). The coherence in the rocky ROI appears fairly constant, especially for the VV interferograms, while small coherence variations (less than 0.05) with an increase of the standard deviation can be observed for the HH interferograms.

An increase of the average phase can be noticed in correspondence of the transitions from Nov. 8 to Nov. 19 (HH interferograms) and from Nov. 15 to Nov. 19 (VV interferograms). A rather apparent phase standard deviation increase can be observed in the trees2 and the meadow ROIs in both polarizations in all interferograms of Nov. 19.

Interestingly, the interferograms formed using a SAR image acquired after the rainfall as primary of the interferometric stack, shows a very high coherence (above 0.8–0.9) and an almost zero phase on short temporal baselines, that is for the acquisitions on the same day (Nov. 19).

4.3.5 Coherence CDF

To better analyse the distribution of coherence values, Fig. 4.13 shows the empirical cumulative distribution function (CDF) of the coherence within the four ROIs (meadow, trees1, trees2, and rock) for the HH polarized interferograms with temporal baselines ranging from less than one hour to 15 days.

In the rocky ROI (Fig. 4.13d), the CDF curves approach the ideal distribution (close to $\gamma = 1$), with 94% percent of the data points having coherence above 0.85 in the worst case amongst all interferograms.

A larger coherence variability can be observed in the vegetated areas. In the trees2 ROI (Fig. 4.13c), the interferograms of Nov. 19 and some of the interferograms of Nov. 6 (violet and orange curves, respectively) show overall less coherence. In particular, the curves relevant to Nov. 6 appear split in two groups: during the time interval of higher wind speed (curves E, F, G, H, I, J, K), between 43% and 77% of the points have $\gamma < 0.4$ ($P(\gamma \leq 0.4) \in [0.43, 0.77]$) and a median coherence value between 0.27 and 0.45; during the time interval of lower wind speed (curves B, C, D, L, M), about 13% of the points have coherence $\gamma < 0.4$ and a median coherence value between 0.67 and 0.78. The interferograms with secondary on Nov. 19 have around 40% of the points with $\gamma < 0.4$ and a median coherence around 0.45. The other curves in Fig. 4.13c (excluding violet and orange ones) show less than 20% of the points with $\gamma < 0.4$ and a median value between 0.56 and 0.79.

In the trees1 ROI (Fig. 4.13b) the spreading of the curves relevant to the interferograms of Nov. 6 is also apparent, although less pronounced than in the trees2 ROI. Overall, between 0% and 33% of data points in the trees1 ROI have $\gamma < 0.4$, depending on the secondary acquisition, and the median coherence is between 0.5 and 0.87. The interferograms of Nov. 20, having longer temporal baselines, show generally lower coherence. It can be also noted that the interferograms of Nov. 19 retain better coherence than in the trees2 ROI, with a percentage of less than 1.5% of points with $\gamma < 0.4$ and a median coherence around 0.68. Interestingly, the interferograms of Nov. 7, although achieving the best coherence performance overall (together with the interferogram of Nov. 5), show a roughly inverse pattern with the temporal baseline, with higher coherence relevant to longer temporal baselines.

In the meadow ROI between 13% and 67% of data points have $\gamma < 0.4$ and the median coherence value ranges between 0.32 and 0.63. As for the trees2 ROI, the interferograms showing the worst coherence are the ones with secondary on Nov. 19 and partially on Nov. 6.

(a) Meadow.

(b) Trees

(c) Trees2

(d) Rock

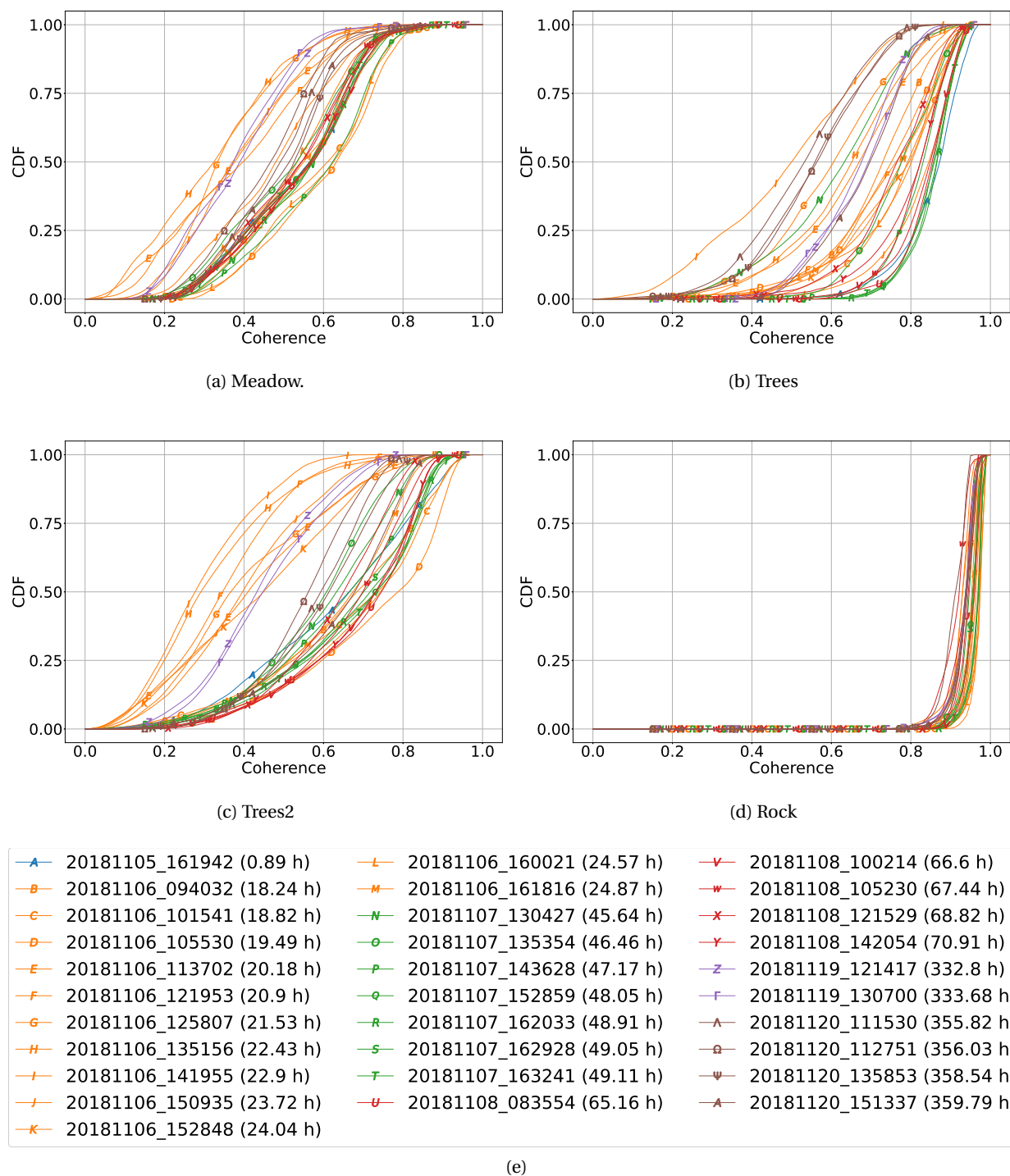|		
A 20181105_161942 (0.89 h)	L 20181106_160021 (24.57 h)	V 20181108_100214 (66.6 h)
B 20181106_094032 (18.24 h)	M 20181106_161816 (24.87 h)	W 20181108_105230 (67.44 h)
C 20181106_101541 (18.82 h)	N 20181107_130427 (45.64 h)	X 20181108_121529 (68.82 h)
D 20181106_105530 (19.49 h)	O 20181107_135354 (46.46 h)	Y 20181108_142054 (70.91 h)
E 20181106_113702 (20.18 h)	P 20181107_143628 (47.17 h)	Z 20181119_121417 (332.8 h)
F 20181106_121953 (20.9 h)	Q 20181107_152859 (48.05 h)	F 20181119_130700 (333.68 h)
G 20181106_125807 (21.53 h)	R 20181107_162033 (48.91 h)	A 20181120_111530 (355.82 h)
H 20181106_135156 (22.43 h)	S 20181107_162928 (49.05 h)	O 20181120_112751 (356.03 h)
I 20181106_141955 (22.9 h)	T 20181107_163241 (49.11 h)	W 20181120_135853 (358.54 h)
J 20181106_150935 (23.72 h)	U 20181108_083554 (65.16 h)	A 20181120_151337 (359.79 h)
K 20181106_152848 (24.04 h)		

(e)

Figure 4.13: Coherence cumulative distribution function of interferograms with temporal baselines spanning 15 days. Primary acquisition Nov. 5, 2018, at 15:26:11. The legend reports the date and time of the secondary acquisition in the format yyyymmdd_hhmmss and the temporal baseline in parentheses. The multilooking window is 20m × 40m. The coherence values in the rocky area approach the ideal distribution, while larger variations are visible in the vegetated areas particularly with secondary acquisitions on Nov. 6 (during windy periods) and on Nov. 19 (after a rainfall).

4.4 DISCUSSION

Interferometric coherence and phase fluctuations stem from changes of the physical properties of the imaged targets occurring between the SAR acquisitions. From the results of the interferometric temporal analysis it emerges that within the relatively short time span of two weeks, spatially-varying weather-related conditions can drive the coherence behaviour in vegetated areas to a greater extent than the temporal baseline increase. In fact, the physical properties of the imaged targets are largely influenced by the local weather conditions. Especially in mountainous regions, the latter can change quite drastically over short time spans [34, 35] and therefore impact the SAR observables and the interferometric performance. Coherence and phase variations can be observed both temporally, even for temporal baselines of less than a few hours, and spatially within each ROI each characterised by a relatively homogeneous land cover.

As a consequence of the varying weather-related environmental conditions, even selecting same-length temporal baselines at different times, significant correlation and phase changes can be observed. For example, for a temporal baseline of 5 days, a larger decorrelation is observable in the interferograms Nov. 14–19 (primary–secondary) in Fig. 4.10a than in the interferograms of Nov. 20–15 in Fig. 4.10c.

Since the coherence is a measure of the degree of mutual similarity between the primary and the secondary acquisitions, changes of the physical properties of the imaged scene occurring between the acquisitions and, specifically, the choice of the (common) primary acquisition used for the interferometric time-series, have an impact on the interferometric performance. This is well illustrated in the plots in Fig. 4.9, Fig. 4.10, and Fig. 4.12, where the time-series created using different primaries generally show different phase and coherence variations. Nevertheless, the presence of comparable coherence and phase patterns in different time-series is an indication of phenomena directly affecting the secondary acquisitions. In such cases, in absence of known acquisition errors such as sharp manoeuvres of the radar platform or processing errors, a relation between weather and interferometric changes could be possible.

Two main decorrelation patterns are clearly visible in the time-series and in the CDF plots shown in Section 4.3. Those patterns can be related to the increase of wind speed during the SAR acquisitions and to the occurrence of rainfalls.

Effect of wind speed   The weather data reveals the higher wind speed measured on Nov. 6 compared to the other days of the period of interest. Although the weather station does not provide the wind speed values at the exact time and location of the SAR acquisitions, the data give a good indication of the general trend in the region. Depending on the structural parameters of the trees such as height, diameter, and stiffness [36], wind can induce significant swaying of tree branches and twigs, of the canopy leaves, and of the meadow blades, causing differences in the SAR acquisitions that can lead to interferometric decorrelation [13].

The decorrelation and the phase variations measured on Nov. 6 in the meadow and the forested areas, clearly visible in the plots of the empirical CDF (Fig. 4.13) and in the coherence time-series for different primaries (Fig. 4.9), appear well correlated with the wind speed variations of Nov. 6 (Fig. 4.11c), with

larger decorrelation (and phase variations) measured in correspondence of higher wind speed. In line with the findings in [10], a wind speed above 1.5 m/s appears to be already sufficient to cause large decorrelation in the vegetated areas. On the other hand, the rocky area only shows minor temporal and spatial coherence and phase variations, as also indicated by the small standard deviation reported in the time series and the small spread of the coherence CDF curves. The small coherence drop visible in the interferograms of Nov. 6 at 12:58 only entails a small increase of the phase standard deviation and is likely linked to the presence of scattered vegetation on the rock as visible in Fig. 4.1c.

Interestingly, the increase of wind speed also entails a persistent average phase deviation from zero in the vegetated areas (Fig. 4.11b). The average phase values tend to be roughly the same before and after the higher wind speed period, suggesting a readjustment of the tree canopies and of the vegetation after the wind loses its strength. As within each area the phase values of many resolution cells are averaged, random target movements are mostly averaged out. The resulting phase deviation might therefore indicate a bundle vegetation movement, on average, in a preferred direction as a consequence of the wind loading during the higher wind speed interval. Especially in the case of Fig. 4.11b, the short temporal baselines between the acquisitions and the closeness of the vegetated ROIs to the interferometric reference point, which is set on a stable point on the rock, allow to exclude that such phase deviation is caused by troposphere-induced path delays, since the latter are generally spatially and temporally correlated.

Primary acquisition affected by stronger wind   By using a primary acquired during the time interval of higher wind speed a large coherence loss in the vegetated areas can be observed for the entire two-weeks period even for acquisition pairs with short temporal baselines (e.g. in the interferograms with secondary acquisitions at 13:51 and 15:09 in Fig. 4.12a).

In the case of spaceborne or airborne acquisitions, because of the wide area mapping, it is often the case that different vegetated areas located kilometres apart are imaged. If one or more of such vegetated areas are affected by relatively high wind speed at the time of the primary acquisition, the coherence on those areas would be negatively affected for the entire interferometric stack. However, because of the usually low temporal sampling of spaceborne and airborne systems, avoiding primary acquisitions affected by unfavourable wind conditions in one or more areas of interest could contrast, for example, with the requirement of minimising the maximum temporal baseline of the single-primary interferometric stack. Analysing the interferometric stack using different primaries could be a viable way to aim for coherence improvements in specific vegetated areas of interest.

Effect of rain and moisture   Dielectric changes due to variations of vegetation (or soil) water content are important drivers of coherence variations [2, 10, 37]. The presence of water in a medium changes its dielectric constant and hence its scattering properties, thus influencing the phase and the intensity of the backscattered electromagnetic waves [32, 38].

During a rainfall, the rain is partially intercepted by the tree canopies and partially falls on the soil through the canopies or by gliding over the tree trunk [39, 40]. The amount of water retained by the

tree canopies depends on many factors, most notably on the canopy density, on the mean leaf area, and, in general, on the the tree species [40, 41].

The fading decorrelation signal measured on Nov. 19 in the vegetated areas (trees1, trees2, and meadow) is likely triggered by the rainfall that affected the region about one hour before performing the first SAR acquisition, as visible in the weather data in Fig. 4.5. Such decorrelation pattern is observable in different time-series, that is using different primaries and temporal baselines, thus confirming that the (secondary) acquisitions of Nov. 19, particularly the one temporally closer to the end of the rainfall, are responsible for the coherence loss.

Thanks to their relatively long wavelength, L-band radar signals have the ability to penetrate through the tree canopies and partially into the soil, depending on the dielectric constant of the medium. The increase of vegetation water content following a rainfall or the formation of moisture can sensibly change the penetration depth and, therefore, the path of the radar signal inside the medium, thus contributing to volume decorrelation [8, 32].

As it can be observed in the time-series in Figs. 4.9 and 4.10, in two of the vegetated areas (meadow and trees2), after the rainfall of Nov. 19 the coherence slowly recovers throughout Nov. 20, which is characterised by a high level of relative air humidity and low temperatures. The results indicate that coherence and phase variations can persist even the day following the rainfall event, likely as a consequence of the water retained by the vegetation. The latter is a function of the amount of precipitation, of the temperature, and also of the relative air humidity, since high levels of relative air humidity limit the vegetation evapotranspiration processes, thus increasing the likelihood of moisture persisting in the vegetation [33]. Such results are in agreement with the ones reported in [42], showing decorrelation likely induced by a rainfall lasting (at least) several hours after the end of the precipitation.

Remarkably, the interferograms formed with both SAR images acquired after the rainfall (see interferograms of Nov. 19 in Fig. 4.12c and 4.12d) show a high level of coherence and an almost zero interferometric phase, suggesting that comparable scattering mechanisms occur in the two acquisitions as a consequence of the similar level of moisture in the vegetation.

Interferometric phase deviations up to 0.6 rad can be observed after the rainfall of Nov. 19, corresponding to a range difference in the line of sight of about 1 cm. However, a precise interpretation of the phase signal in vegetated areas is rather challenging due to the random multiple reflections occurring in the canopies and to the constructive and destructive interference of the backscattered waves. It is also worth noting that the DEM used in the processing does not account for the presence of the trees and therefore phase errors in the forested areas may arise in presence of spatial baselines between the acquisitions, although such effect is expected to be minimal in the present analysis thanks to the very small baselines between the acquisition.

Precipitation events were also measured on Nov. 13 (one day before the radar acquisitions) and for large part of Nov. 14 the relative air humidity was at saturation, conditions that can determine to the formation of moisture on the targets. Therefore, the coherence variations observable in the morning of Nov. 14 (Fig. 4.10a and 4.10c) are possibly caused by changes in the moisture level in the imaged areas.

Nevertheless, while the effect of rainfalls on the interferometric performance can be evident, the in-

fluence of the relative air humidity is more subtle since the latter cannot be directly translated into information about the vegetation water content without an in-depth analysis of the local condensation and evapotranspiration processes, which ideally entails also the knowledge of the leaves temperature [33]. Furthermore, relative air humidity and temperature changes do not trigger immediate effects on the physical properties of the scatterers as, on the contrary, rainfalls and wind speed variations do.

The backscatter increase visible in all areas in Fig. 4.6b in the transition from Nov. 14 to Nov. 15, from Nov. 15 to Nov. 19, and from Nov. 19 to Nov. 20 is also consistent with the increase of the water content in the target area, in accordance with the positive correlation between the radar backscatter and the vegetation water content or the soil moisture reported by different studies [9, 38, 43–45]. In the time-series in Fig. 4.6a, this phenomenon is less apparent. However, it must be noted that the acquisitions of Nov. 7 start from 13:04 and therefore there was enough time for the dew formed overnight to evaporate, particularly in consideration of the steady temperature increase reported throughout the morning, while the weather measurements relevant to Nov. 8 do not show saturation of the relative air humidity during the night before the acquisitions. It is worth highlighting that while the backscatter increases also in the rocky area, the coherence variations in the same time-frames are rather contained and mostly attributable to the sparse vegetation over the rock.

Another pattern that can be observed in the interferometric time series is the generally lower interferometric coherence achieved around noon, which could be linked to the higher solar radiation triggering phenomena such as the evaporation of the dew accumulated overnight [46]. This result is consistent with the findings of the scatterometer experiment presented in [15] where acquisitions at noon generally show lower coherence.

Influence of polarization and acquisition geometry   The overall lower coherence measured in the meadow area is possibly influenced by the large incidence angle implying lower SNR and larger temporal variability of the backscatter as compared to the other areas. On the other hand, the trees of the forested areas offer a larger radar cross section from the car-borne acquisition geometry. Nevertheless, particularly in the meadow area, a generally higher coherence with the VV-polarized acquisitions as compared to the HH-polarized ones can be observed even for short temporal baselines. Such effect cannot be explained by a mismatch of the intrinsic performance of the two polarimetric channels (e.g. due to different noise levels), since the coherence achieved in the more stable rocky area is roughly comparable in the two cases (mostly above 0.95 on average). A higher coherence in VV interferograms than in HH ones in an area covered by meadow was also observed in [47] with airborne acquisitions. Such pattern should be further investigated to assess if comparable results can be achieved in different scenarios, seasons, and incidence angles.

4.5 CONCLUSIONS

The temporal analysis of the L-band car-borne SAR data presented herein showed the variability of the SAR observables over short and medium temporal baselines, highlighting spatially- and temporally-

varying backscattering and interferometric fluctuations as a consequence of the weather-related environmental conditions.

Different areas showed different interferometric performance in function of the land cover class. The average coherence in the rocky area appeared stable and high with limited spatial and temporal fluctuations, and the average phase remained roughly stable around zero, while larger variations were observed in the vegetated areas. Specifically, substantial variations were observed in the events of moderate wind and rainfalls causing evident fading decorrelation patterns.

Moisture changes also appeared to be responsible for interferometric variations. As a consequence of low temperatures and high relative air humidity reached at night, usually at saturation, dew is likely to form on surfaces and vegetation canopies and can persists until early morning, when the raise of temperatures after sunrise favours evaporation [46]. The presence of moisture is not problematic per se, but its variation in the time span between the acquisitions can lead to interferometric changes. Therefore, SAR acquisitions performed during time intervals of high relative humidity (say above 90%–95%) may lead to coherence and phase variations when interferometrically combined with acquisitions performed during low humidity intervals. Large variations of air humidity are more likely to occur during daytime. It is worth noting that higher temperatures imply higher absolute air humidity given the same relative humidity, and, hence, larger interferometric fluctuations may result.

The generally lower interferometric coherence observed for the acquisitions around noon is consistent with the expected higher weather dynamics triggered by the solar radiation, detrimental for interferometric acquisitions. However, this pattern needs further investigation to understand its range of validity in terms of, for example, temperature and humidity levels.

Due to such variability of the interferometric signals, deformation monitoring in vegetated areas is a challenging task. The dynamic behaviour of the natural environment pose a limit to the precision of the differential interferometric technique, particularly due to the presence of phase biases. Nevertheless, in consideration of the overall high level of coherence achieved with temporal baselines up to two weeks in the areas covered by vegetation, the analyses confirm the suitability of the system to perform interferometric measurements in natural areas. Such results indicate the possibility to apply, for example, coherence change detection techniques for deformation monitoring. Furthermore, differently from weather-related decorrelation and phase changes, which appear to be fading, deformation events would give rise to permanent decorrelation and phase offsets that would therefore be visible along the time-series. Potentially, tomographic acquisitions from UAV would also benefit from the high coherence achieved at L-band, for example for the retrieval of forest height profiles [19, 37].

Further extending the temporal analysis of the SAR observables to nighttime acquisitions would allow to observe potential diurnal/nocturnal coherence cycles, as reported in [15], and to verify if the (expected) more stable environmental conditions, particularly in terms of vegetation and soil water content, result in more stable interferometric performance [4, 48]. For this purpose, the rail-based L-band SAR setup represent a valuable asset, since it allows to perform continuous acquisitions over extended periods of time with fine and regular temporal sampling in an automatic fashion (i.e. without the presence of a radar operator). Nevertheless, such advantage comes at the cost of lower azimuth resolution due to the

limited synthetic antenna length achievable with the rail, which also implies a worse suppression of the sidelobes leading to a larger mutual interference of nearby areas.

REFERENCES

[1] A. K. Gabriel, R. M. Goldstein, and H. A. Zebker, "Mapping small elevation changes over large areas: differential radar interferometry," *Journal of Geophysical Research*, vol. 94, no. B7, pp. 9183–9191, 1989.

[2] D. Massonnet and K. L. Feigl, "Radar interferometry and its application to changes in the Earth's surface," *Reviews of Geophysics*, vol. 36, no. 4, pp. 441–500, 1998.

[3] H. A. Zebker and J. Villasenor, "Decorrelation in interferometric radar echoes," *IEEE Transactions on Geoscience and Remote Sensing*, vol. 30, pp. 950–959, Sep 1992.

[4] A. Monti-Guarnieri, M. Manzoni, D. Giudici, A. Recchia, and S. Tebaldini, "Vegetated target decorrelation in SAR and interferometry: Models, simulation, and performance evaluation," *Remote Sensing*, vol. 12, no. 16, 2020.

[5] M. Wei and D. T. Sandwell, "Decorrelation of L-band and C-band interferometry over vegetated areas in california," *IEEE Transactions on Geoscience and Remote Sensing*, vol. 48, pp. 2942–2952, Jul 2010.

[6] P. A. Rosen, S. Hensley, I. R. Joughin, F. K. Li, S. N. Madsen, E. Rodriguez, and R. M. Goldstein, "Synthetic aperture radar interferometry," *Proceedings of the IEEE*, vol. 88, no. 3, pp. 333–382, 2000.

[7] Y. Morishita and R. F. Hanssen, "Temporal decorrelation in L-, C-, and X-band satellite radar interferometry for pasture on drained peat soils," *IEEE Transactions on Geoscience and Remote Sensing*, vol. 53, pp. 1096–1104, Feb 2015.

[8] J. O. Hagberg, L. M. Ulander, and J. Askne, "Repeat-pass SAR interferometry over forested terrain," *IEEE Transactions on Geoscience and Remote Sensing*, vol. 33, pp. 331–340, Mar 1995.

[9] F. T. Ulaby, B. Brisco, and C. Dobson, "Improved spatial mapping of rainfall events with spaceborne SAR imagery," *IEEE Transactions on Geoscience and Remote Sensing*, vol. GE-21, pp. 118–121, Jan 1983.

[10] S. Lee, F. Kugler, K. P. Papathanassiou, and I. Hajnsek, "Quantification of temporal decorrelation effects at L-band for polarimetric SAR interferometry applications," *IEEE Journal of Selected Topics in Applied Earth Observations and Remote Sensing*, vol. 6, pp. 1351–1367, June 2013.

[11] P. Prats, A. Reigber, J. J. Mallorqui, R. Scheiber, and A. Moreira, "Estimation of the temporal evolution of the deformation using airborne differential SAR interferometry," *IEEE Transactions on Geoscience and Remote Sensing*, vol. 46, no. 4, pp. 1065–1078, 2008.

[12] M. Simard, S. Hensley, M. Lavalle, R. Dubayah, N. Pinto, and M. Hofton, "An empirical assessment of temporal decorrelation using the uninhabited aerial vehicle synthetic aperture radar over forested landscapes," *Remote Sensing*, vol. 4, no. 4, pp. 975–986, 2012.

[13] M. Lort, A. Aguasca, C. López-Martínez, and X. Fabregas, "Impact of wind-induced scatterers motion on GB-SAR imaging," *IEEE Journal of Selected Topics in Applied Earth Observations and Remote Sensing*, vol. 11, pp. 3757–3768, Oct 2018.

[14] W. Li, E. Chen, Z. Li, W. Zhang, and H. Li, "Temporal decorrelation on airborne repeat pass P-, L-band T-SAR in boreal forest," in *2016 IEEE International Geoscience and Remote Sensing Symposium (IGARSS)*, pp. 5–8, Jul 2016.

[15] A. Hamadi, L. Villard, P. Borderies, C. Albinet, T. Koleck, and T. Le Toan, "Comparative analysis of temporal decorrelation at P-band and low L-band frequencies using a tower-based scatterometer over a tropical forest," *IEEE Geoscience and Remote Sensing Letters*, vol. 14, pp. 1918–1922, Nov 2017.

[16] S. E. I. Essebtey, L. Villard, P. Borderies, T. Koleck, B. Burban, and T. Le Toan, "Comparative study of temporal decorrelation at P, L and C-bands: First insights from the Tropiscat-2 experiment," in *2020 Mediterranean and Middle-East Geoscience and Remote Sensing Symposium (M2GARSS)*, pp. 246–249, Mar 2020.

[17] R. Coscione, I. Hajnsek, and O. Frey, "An experimental car-borne SAR system: Measurement setup and positioning error analysis," in *2018 IEEE International Geoscience and Remote Sensing Symposium*, pp. 6364–6367, 2018.

[18] O. Frey, C. L. Werner, I. Hajnsek, and R. Coscione, "A car-borne SAR system for interferometric measurements: Development status and system enhancements," in *2018 IEEE International Geoscience and Remote Sensing Symposium*, pp. 6508–6511, 2018.

[19] O. Frey, C. Werner, and R. Coscione, "Car-borne and UAV-borne mobile mapping of surface displacements with a compact repeat-pass interferometric SAR system at L-band," in *2019 IEEE International Geoscience and Remote Sensing Symposium*, pp. 274–277, Jul 2019.

[20] S. Suter, T. Konzelmann, C. Mühlhäuser, M. Begert, and A. Heimo, "SwissMetNet–the new automatic meteorological network of Switzerland: transition from old to new network, data management and first results," vol. 24, 01 2006.

[21] O. Frey, E. Meier, and D. Nüesch, "A study on integrated SAR processing and geocoding by means of time-domain backprojection," in *Proc. Int. Radar Symp.*, 2005.

[22] O. Frey, E. H. Meier, and D. R. Nüesch, "Processing SAR data of rugged terrain by time-domain backprojection," in *SAR Image Analysis, Modeling, and Techniques VII* (F. Posa, ed.), vol. 5980, pp. 71 – 79, International Society for Optics and Photonics, SPIE, Oct 2005.

[23] M. I. Duersch and D. G. Long, "Analysis of time-domain back-projection for stripmap SAR," *International Journal of Remote Sensing*, vol. 36, no. 8, pp. 2010–2036, 2015.

[24] R. Touzi, A. Lopes, J. Bruniquel, and P. W. Vachon, "Coherence estimation for SAR imagery," *IEEE Transactions on Geoscience and Remote Sensing*, vol. 37, pp. 135–149, Jan 1999.

[25] H. A. Zebker and K. Chen, "Accurate estimation of correlation in InSAR observations," *IEEE Geoscience and Remote Sensing Letters*, vol. 2, no. 2, pp. 124–127, 2005.

[26] E. Rodriguez and J. Martin, "Theory and design of interferometric synthetic aperture radars," *IEE Proceedings F Radar and Signal Processing*, vol. 139, pp. 147–159, Apr 1992.

[27] A. Ferretti, A. Monti-Guarnieri, C. Prati, F. Rocca, and D. Massonnet, "InSAR principles - guidelines for SAR interferometry processing and interpretation," *ESA Training Manual*, vol. 19, 01 2007.

[28] M. Manzoni, M. E. Molinari, and A. Monti-Guarnieri, "Multitemporal InSAR coherence analysis and methods for sand mitigation," *Remote Sensing*, vol. 13, no. 7, 2021.

[29] M. Lavalle, M. Simard, and S. Hensley, "A temporal decorrelation model for polarimetric radar interferometers," *IEEE Transactions on Geoscience and Remote Sensing*, vol. 50, pp. 2880–2888, Jul 2012.

[30] E. Weber Hoen and H. Zebker, "Penetration depths inferred from interferometric volume decorrelation observed over the Greenland ice sheet," *IEEE Transactions on Geoscience and Remote Sensing*, vol. 38, pp. 2571–2583, Nov 2000.

[31] M. A. El-rayes and F. T. Ulaby, "Microwave dielectric spectrum of vegetation-Part I: Experimental observations," *IEEE Transactions on Geoscience and Remote Sensing*, vol. GE-25, pp. 541–549, Sep. 1987.

[32] F. T. Ulaby and M. A. El-rayes, "Microwave dielectric spectrum of vegetation - Part II: Dual-dispersion model," *IEEE Transactions on Geoscience and Remote Sensing*, vol. GE-25, pp. 550–557, Sep. 1987.

[33] V. Novák, *Evapotranspiration: A Component of the Water Cycle*, pp. 1–13. Dordrecht: Springer Netherlands, 2012.

[34] C. D. Whiteman, *Mountain Meteorology: Fundamentals and Applications*. New York: Oxford University Press, 2000.

[35] M. Beniston, "Mountain weather and climate: A general overview and a focus on climatic change in the Alps," *Hydrobiologia*, vol. 562, pp. 3–16, Jun 2006.

[36] J. Moore, B. Gardiner, and D. Sellier, *Tree Mechanics and Wind Loading*, pp. 79–106. Springer International Publishing, 2018.

[37] M. Pardini, K. P. Papathanassiou, and F. Lombardini, "Impact of dielectric changes on L-band 3-D SAR reflectivity profiles of forest volumes," *IEEE Transactions on Geoscience and Remote Sensing*, vol. 56, pp. 7324–7337, Dec 2018.

[38] R. Lucas, J. Armston, R. Fairfax, R. Fensham, A. Accad, J. Carreiras, J. Kelley, P. Bunting, D. Clewley, S. Bray, D. Metcalfe, J. Dwyer, M. Bowen, T. Eyre, M. Laidlaw, and M. Shimada, "An evaluation of the ALOS PALSAR L-band backscatter—above ground biomass relationship Queensland, Australia: Impacts of surface moisture condition and vegetation structure," *IEEE Journal of Selected Topics in Applied Earth Observations and Remote Sensing*, vol. 3, pp. 576–593, Dec 2010.

[39] X. Shi, C. Du, X. Guo, and W. Shi, "Heterogeneity of water-retention capacity of forest and its influencing factors based on meta-analysis in the Beijing-Tianjin-Hebei region," *Journal of Geographical Sciences*, vol. 31, pp. 69–90, 2021.

[40] D. E. Klimenko, E. S. Cherepanova, and A. A. Khomyleva, "Spatial modeling of maximum capacity values of irrecoverable rainfall retention by forests in a small watershed," *Forests*, vol. 11, no. 6, 2020.

[41] K. Venkatraman and N. Ashwath, "Canopy rainfall intercepted by nineteen tree species grown on a phytocapped landfill," *International Journal of Waste Resources*, vol. 06, no. 01, 2016.

[42] A. R. Monteith and L. M. H. Ulander, "A tower-based radar study of temporal coherence of a boreal forest at p-, l-, and c-bands and linear cross polarization," *IEEE Transactions on Geoscience and Remote Sensing*, pp. 1–15, 2021.

[43] P. C. Dubois, J. van Zyl, and T. Engman, "Measuring soil moisture with imaging radars," *IEEE Transactions on Geoscience and Remote Sensing*, vol. 33, no. 4, pp. 915–926, 1995.

[44] M. C. Dobson and F. T. Ulaby, "Preliminaly evaluation of the SIR-B response to soil moisture, surface roughness, and crop canopy cover," *IEEE Transactions on Geoscience and Remote Sensing*, vol. GE-24, pp. 517–526, Jul 1986.

[45] F. T. Ulaby, P. C. Dubois, and J. van Zyl, "Radar mapping of surface soil moisture," *Journal of Hydrology*, vol. 184, no. 1, pp. 57–84, 1996. Soil Moisture Theories and Observations.

[46] S. Hanisch, C. Lohrey, and A. Buerkert, "Dewfall and its ecological significance in semi-arid coastal south-western Madagascar," *Journal of Arid Environments*, vol. 121, pp. 24–31, Oct 2015.

[47] A. Reigber and R. Scheiber, "Airborne differential SAR interferometry: First results at L-band," *IEEE Transactions on Geoscience and Remote Sensing*, vol. 41, no. 6 PART II, pp. 1516–1520, 2003.

[48] R. F. Hanssen, *Radar Interferometry: Data Interpretation and Error Analysis*. Remote Sensing and Digital Image Processing, Springer, 2001.

5

CONCLUSIONS

The purpose of this chapter is to summarise the main findings of the investigations reported in this dissertation by addressing the research questions raised in Chapter 1.

Positioning performance The investigation presented in Chapter 3 aimed at performing a quantitative analysis of the positioning accuracy achievable with the INS/GNSS system employed on board of the car-borne SAR system and to assess the impact of the positioning errors on the repeat-pass DInSAR phase for different configurations of GNSS reference stations. The positioning errors were analysed in a controlled repeat-pass SAR and positioning measurement setup, with the L-band SAR system and the navigation-grade INS/GNSS system mounted in a rail-based configuration ensuring an almost perfect repeatability of the platform over multiple passes.

- **How much does the positioning error change in function of the distance of the radar platform from the GNSS reference station?**

- **How much does the positioning error change within the time span of the synthetic aperture and from pass to pass?**

To answer those questions the positioning accuracy of the PPK-only and of the loosely-coupled INS/PPK positioning solutions were analysed by employing a portable GNSS receiver mounted in the vicinity of the SAR platform (local reference station) and the two closest reference stations of the permanent network of GNSS receivers in Switzerland (AGNES). The remote reference stations were located at a distance of about 20 km from the radar platform, with an height difference between the stations of about 1 km.

In positioning approaches based on the use of INS/GNSS systems, the performance of the final positioning solutions–i.e. after integration of the INS and the post-processed GNSS measurements to reduce the INS accumulation error–are largely influenced by the accuracy of the GNSS measurements. Uncompensated tropospheric path delays affecting the post-processed GNSS positions play a major role on the long-term positioning accuracy of the integrated solution and, consequently, on the interferometric repeat-pass spatial baseline error.

Although all the different GNSS configurations achieved good potential performance based on the number of satellites visible from the rover and the reference stations (more than 2 times the minimum number required to perform differential GNSS) and the good positional dilution of precision, the final positioning performance were largely different. Even during static measurements, that is with the GNSS rover standing still in the same position throughout the measurements, the level of precision of the platform position achieved with the local reference station was about 4–6 times better than in the case of the remote reference stations. Furthermore, in the case of the remote reference station with the larger height difference from the radar platform, an altitude offset of few centimeters with respect to the actual platform position was observed, likely due to larger uncompensated tropospheric path delays of the GNSS signals.

Regarding the positioning performance relevant to repeat-pass InSAR/DInSAR acquisitions, the pass-to-pass error achieved in the altitude component (which is generally the worst case in terms of precision) of the radar platform position was 5 to 10 times better in the configuration employing the local reference station as compared to the case of the remote reference stations. Furthermore, while the horizontal components achieved a higher level of precision compared to the altitude, they also showed an offset, with respect to the nominal position, when using the remote reference stations. Within the time-span of the synthetic aperture (27 seconds in the test), the variation of the altitude error between the beginning and the end of the acquisitions was below 0.5–1 cm in the case of the local reference station and around 1–1.5 cm in the case of the remote reference stations, corresponding to a maximum apparent rail rotation, compared to the actual rail inclination, of less than 0.1 degrees in the vertical plane.

Therefore, while the altitude variations within the synthetic aperture time did not appear to be critical (at L-band) even in the case of the remote reference stations, the pass-to-pass error reached values corresponding to about half radar wavelength with the remote reference stations, while the errors amounted to a small fraction of the radar wavelength ($\lambda/20$–$\lambda/10$) in the case of the local reference station.

- **What is the variation of positioning-related interferometric (DInSAR) phase errors in the typical acquisition geometry of the car-borne SAR?**

- **Is the use of a GNSS reference station deployed in the vicinity of the radar platform required to achieve the desired positioning accuracy or are the available reference stations of the permanent GNSS network sufficient?**

To assess the impact of the time-varying positioning errors on the differential interferometric phase, a non-standard interferometric product, referred as self-interferogram in Chapter 3, was employed. A self-interferogram entails the use of acquisition pairs relevant to the same raw data but focused with different trajectories (the nominal sensor trajectory and the INS/PPK trajectory, respectively). Such expedient allowed to observe the phase patterns owed to the errors of the different INS/PPK positioning solutions with respect to the nominal sensor trajectory while removing any phase contribution caused by the atmospheric phase gradient affecting the radar data.

The results showed mostly small scale phase noise in the case of sensor trajectories obtained with the local GNSS reference station with possibly smooth azimuth trends of less than 5°–10°. On the other hand, large phase trends (up to 60°–90°) appeared in the case of radar data focused with sensor trajectories obtained with the remote reference station. Such phase trends are comparable to the case that a repositioning error of the rail is introduced as a consequence of the disassembling and reassembling of the system during different campaigns, resulting in a misalignment between the acquisitions.

Based on the results herein summarised, it can be concluded that when the sensor trajectories are obtained via a INS/GNSS-based approach, the use of a GNSS reference station located in the vicinity of the SAR platform is a critical requirement to achieve a high positioning accuracy and to minimise interferometric phase errors. Although from an operational point of view the use of a local reference station implies an additional burden in terms of measurement setup, it also reduces the need to resort to interferometric phase error estimation techniques based for example on autofocus and/or on the exploitation of ground control points, which may be challenging especially in natural scenarios where point-like scatterers are generally scarce and the deployment of corner reflectors may be unfeasible.

Interferometric performance   In Chapter 4, an empirical investigation of the temporal evolution of the SAR data observables relevant to repeat-pass acquisitions was performed. The aim of such investigation was to assess the interferometric performance of the L-band car-borne SAR system in a real acquisition scenario characterised by the presence of natural features. In particular, the objective was to observe the short-term temporal evolution of the interferometric coherence and its link to weather changes.

- **What is the level of interferometric coherence achievable with the car-borne SAR system in a natural environment characterised by the presence of vegetation?**

- **How does the coherence change depending on the land cover class and as a function of time?**

- **Do longer temporal baselines, within the relatively short time span of 15 days, entail lower coherence?**

The analysis of the repeat-pass differential interferometric SAR measurements performed with the car-borne SAR system in a natural scenario revealed an overall high level of coherence achieved within short and medium temporal baselines (up to 15 days).

The highest level of coherence (mostly above 0.95) was achieved in a sparsely vegetated rocky area, with minimal temporal and spatial variations and a high interferometric phase stability achieved over repeated acquisitions with increasing temporal baselines. Incidentally, such results indicate the good quality of radar and positioning data acquisition and of the entire processing chain.

The coherence in vegetated areas (forests and meadow) reached levels above 0.8 and up to 0.9 in the case of VV-polarized interferograms with a temporal baseline up to 6 days. In the same areas, HH-polarized interferograms reached coherence levels between 0.6 and 0.9 on short temporal baselines (up to one

day) and between 0.5 and 0.8 with temporal baselines of 13–15 days. Lower coherence was generally observed in the meadow area, possibly due to acquisition geometry entailing larger incidence angles leading to lower SNR. The generally higher coherence achieved in the VV-polarized interferograms as compared to the HH-polarized ones, particularly in the meadow area, should be further investigated to assess if comparable results can be obtained in different scenarios and for different ranges of incidence angles.

With the longer temporal baselines (6 days for the VV acquisitions and 15 days for the HH ones), the achieved level of coherence was not distinctly smaller than the short-term coherence. This outcome appeared evident, and to some extent expected, in the sparsely vegetated rocky area, which reported a roughly constant coherence, as highlighted above. In the vegetated areas, which exhibited larger fluctuations over time, the coherence achieved with temporal baselines of about few hours was, to some degree comparable to the coherence achieved over longer temporal baselines. Such results are likely to be different over longer time spans, i.e. with temporal baselines in the order of months, where morphological vegetation changes, due for example to vegetation growth or abscission, would likely lead to some coherence loss.

- **Can interferometric phase and coherence variations be linked to weather-related changes in the imaged areas such as humidity, rainfall, and wind?**

- **Do such weather-related interferometric changes appear as fading signals?**

The different interferometric time-series analysed in Chapter 4 showed short-term and medium-term fluctuations (i.e. with temporal baselines spanning from minutes to days) in function of local environmental factors. In vegetated areas, the interferometric phase and coherence were characterised by varying patterns markedly driven by local weather-related changes, while the sparsely vegetated rocky area appeared more robust towards these changes. Such observations are in agreement with the principle that the geophysical properties of the imaged areas, such as the moisture content, are largely influenced by the weather conditions, which, especially in mountainous regions, can change conspicuously even within short time spans. In particular, it was observed that the increase of wind speed during the acquisitions and the occurrence of rainfalls could determine evident decorrelation and phase patterns.

The mechanical response of the vegetation to wind loading depends on the vegetation type (e.g. on the trees species) and, more specifically, on its structural parameters such as height, diameter, and stiffness [1]. Swaying of tree branches, of canopy leaves, as well as of grass blades leads to coherence loss when the movement of the targets within the resolution cells is significant with respect to the radar wavelength [2]. In the considered scenario, an average wind speed above 1.5 m/s was already sufficient to cause a coherence loss of about 30%–40% within a short time span. Nevertheless, the results also showed that even during higher wind speed periods, an average coherence above 0.3–0.4 could be retained in the meadow area as well as in one of the forested areas, and a coherence between 0.5 and 0.7 was achieved in a separate forested area, possibly thanks to the capability of the L-band signals to penetrate the foliage and to interact with stable scatterers such as the tree trunks, the larger branches, and with the ground.

It must be pointed out, however, that the spatial variability of the wind can be largely influenced by the local topography, which may partially explain the coherence difference in the two forested areas. An analysis entailing larger variations of wind speeds and possibly the use of a multitude of in-situ measurements to track the spatial variability of the wind in the imaged areas would be beneficial to better understand the interferometric behaviour under different wind regimes, possibly in function of the tree types.

Dielectric changes due to variations of the targets moisture caused by natural phenomena such as rainfall, condensation, evaporation, freezing, and thawing lead to varying scattering mechanisms between the acquisitions to which the interferometric coherence and phase are sensitive. Volume scattering, trunk-ground and canopy-ground double-bounce scattering (in the case of trees), and surface scattering are in principle all influenced by the variation of moisture content [3]. Moreover, the varying signal penetration inside the vegetation layer in function of the moisture level additionally influences the scattering mechanisms. Such effect was clearly observed in case of rainfalls. In particular, decorrelation and phase variations were observed when one of the two SAR images of the interferometric pair was acquired after a rainfall. The coherence displayed a larger drop occurring shortly after the rainfall and a progressive increase over time, with residual decorrelation persisting for more than one day. On the other hand, with interferograms formed using both SAR images acquired after the rainfall, a high coherence and an almost zero phase were achieved, indicating a similarity of the scattering mechanisms in the two acquisitions. Therefore, even in vegetated areas, interferometric SAR acquisition pairs can remain correlated within a time-window after a rainfall. Further tests should be conducted to delineate the range of validity of such phenomenon, whose main driver is in all probability the rate of change of the moisture level retained by the targets. Higher temperatures, for instance during summer, would likely imply faster moisture changes due to evaporation, thus potentially triggering faster decorrelation between interferometric pairs acquired after a rainfall.

Weather-related decorrelation patterns have shown to be fading over time, with extinction times depending on the phenomena. In case of wind speed increase, for example, which entails an immediate physical effect on the vegetation by randomly changing the orientation of leaves and branches, the coherence was recovered as soon as the wind speed reduced again. On the other hand, increase of moisture levels due to rainfalls, caused decorrelation effects lasting up to more than one day as a consequence of the persistence of moisture in the vegetation.

- **Is the availability of multiple acquisitions per day beneficial to circumvent temporally localized decorrelation effects?**

- **What are the implications of such interferometric changes for repeat-pass DInSAR acquisitions for deformation monitoring?**

The overall high level of interferometric coherence achieved with repeat-pass SAR acquisitions in sparsely vegetated and in completely vegetated areas (forest and meadow) confirms the suitability of the L-band car-borne SAR system for the observation of natural environment.

However, the possibility to exploit the phase information in vegetated areas for the retrieval of deformation signals or geophysical parameters is generally hampered by weather-related fluctuations and should be verified on a case-by-case basis. In the scenario analysed in Chapter 4, the observed average phase fluctuations were generally below 0.5–1 rad, corresponding to line of sight variations, at L-band, below 0.9–1.8 cm, potentially allowing to observe permanent surface changes in the order of few centimeters in the time span between the acquisitions.

SAR data acquisitions with sufficiently high temporal sampling over time intervals of hours or days allow to recognise the transient (fading) weather-related coherence and phase patterns along the time-series, which would be challenging or unfeasible at low temporal sampling. Therefore, permanent changes in delimited regions of the imaged area could be distinguished from such interferometric disturbances and identified, for example by means of coherence change detection algorithms, given that the regions affected by the permanent changes are sufficiently large compared to the spatial resolution of the SAR imagery.

The high coherence achieved after 6 days and 15 days indicates the potential to extend the monitoring to longer time-spans, possibly by employing a multi-primary approach, that is by linking sequences of interferometric time-series each characterised by a conveniently short maximum temporal baseline to minimise phase errors [4–6].

The availability of multiple acquisitions per day is also beneficial to increase the likelihood of acquiring SAR data not materially affected by unfavourable weather-related environmental conditions. This is particularly relevant in consideration of the impact of the choice of the primary acquisition on the the final performance of the interferometric stack, as observed in the case of acquisitions, used as primary, obtained during high wind speed and after a rainfall.

From a mission planning viewpoint, SAR acquisitions relevant to time intervals characterised by high wind speeds should be possibly avoided to retain the highest possible coherence in vegetated areas. Nevertheless, at least in the considered scenario, the wind did not induce a total decorrelation in the area of interest and the interferometric phase did not result in completely noisy variations.

Moisture variations occurring in the time span between the acquisitions, however, lead to interferometric fluctuations that can bias the evaluation of potential deformation signals. Circumventing such variations is a challenge. Higher moisture variations can be expected in the morning after sunrise when the increase of temperatures trigger the evaporation of dew that usually forms overnight as a consequence of the low temperatures and the high level of relative air humidity. More generally, high levels of relative air humidity represent a favourable condition for the condensation of the water vapor, which may lead to dynamic dielectric changes of the targets under the influence of the solar radiation during the day. Although less practical from an operational point of view, nighttime acquisitions are expected to meet more stable environmental conditions, which are beneficial for repeat-pass DInSAR applications and, potentially, for tomographic acquisitions from UAV.

REFERENCES

[1] J. Moore, B. Gardiner, and D. Sellier, *Tree Mechanics and Wind Loading*, pp. 79–106. Springer International Publishing, 2018.

[2] H. A. Zebker and J. Villasenor, "Decorrelation in interferometric radar echoes," *IEEE Transactions on Geoscience and Remote Sensing*, vol. 30, pp. 950–959, Sep 1992.

[3] S. Lee, F. Kugler, K. P. Papathanassiou, and I. Hajnsek, "Quantification of temporal decorrelation effects at L-band for polarimetric SAR interferometry applications," *IEEE Journal of Selected Topics in Applied Earth Observations and Remote Sensing*, vol. 6, pp. 1351–1367, June 2013.

[4] P. Berardino, G. Fornaro, R. Lanari, and E. Sansosti, "A new algorithm for surface deformation monitoring based on small baseline differential SAR interferograms," *IEEE Transactions on Geoscience and Remote Sensing*, vol. 40, pp. 2375–2383, Nov 2002.

[5] F. Rocca, "Modeling interferogram stacks," *IEEE Transactions on Geoscience and Remote Sensing*, vol. 45, pp. 3289–3299, Oct 2007.

[6] A. M. Guarnieri and S. Tebaldini, "On the exploitation of target statistics for SAR interferometry applications," *IEEE Transactions on Geoscience and Remote Sensing*, vol. 46, pp. 3436–3443, Nov 2008.

5

6

OUTLOOK

This chapter provides an outlook for future research paths that can branch-out from the current state of the car-borne SAR system.

Long-term interferometric performance   The first topic to further investigate is the long-term temporal analysis of L-band repeat-pass car-borne DInSAR data. The analysis will allow to observe the impact of the long temporal baseline on the interferometric performance for different land covers and at different vegetation growth stages. The seasonal changes of the vegetation are expected to cause coherence loss over longer time spans. However, as a consequence of the penetration capability of the L-band signal into the vegetation, the interaction with stable scatterers such as the tree trunks should contribute to maintain the coherence level at acceptable levels.

Fully polarimetric applications   Future studies could exploit the fully polarimetric capabilities of the L-band SAR system to expand the observation space with the aim to discern different scattering mechanisms.

In fact, a number of parameters can be of interest when monitoring a natural environment such as the characteristics of the vegetation (e.g. height, width, and/or type of trees), the vegetation or soil water content, and sub-canopy topographic changes. Inversion of electromagnetic scattering models is generally required to relate the physical parameters of the targets to the SAR observables. Since a number of parameters concurrently affect the SAR complex backscattering, distinguishing between the different scattering mechanisms and successfully solving the inversion problem is a challenging task.

Especially in the case of single frequency and single polarization acquisitions, the inherent ambiguity of the SAR observables can be hardly solved due to the under-determination of the inversion problem. For example, although the L-band signals can in principle penetrate through the vegetation and interact with the ground, the actual penetration depth is a function of the time-varying geometrical and physical properties of the vegetation layer such as density, depth, and dielectric constant. Especially in dry soil, the electromagnetic signal can also penetrate into the ground. Therefore, the actual scattering phase centre of a resolution cell generally lies somewhere between the boundary of the vegetation layer and the ground, thus mixing the information related to the vegetation parameters and the ground.

Polarimetric SAR (PolSAR) and polarimetric interferometric SAR (PolInSAR) exploit the dependence of the targets scattering mechanisms on the polarization of the incident electromagnetic waves to increase the number of observables and try to solve the ambiguity of the inversion problem [1, 2]. For example, cross-pol (HV) acquisitions are typically sensitive to volume scattering as a consequence of the multiple reflections inside the complex vegetation structures, while HH acquisitions are generally more sensitive to ground scattering. Nevertheless, there is not a sharp separation of the scattering mechanisms in the different polarizations so that, for example, HH acquisitions are still significantly affected by the scattering from the canopy. Polarimetric coherence optimization aims to find a suitable decomposition that enhances the interferometric coherence for specific scattering mechanisms, thus reducing the mixing of the different contributions. Temporal decorrelation and heterogeneity of the vegetation layer represent limiting factors in this context.

A number of scattering models have been introduced to reduce the uncertainty of the inversion problem in PolInSAR methods such as the oriented volume over ground model, the random volume over ground (RVoG) with different extinction models, and the random motion over ground (RMoG), which extends the RVoG by taking into account the intra-resolution-cell movement of the scatterers [1, 3–6].

The application of PolInSAR techniques to the car-borne L-band SAR acquisitions has the important potential to provide geophysical and biophysical information of the imaged area by separating the interferometric contributions owed to different parameters of the ground and the vegetation layers. Based on the single-polarization analyses conducted so far, the expectation is to achieve very high coherence over short/medium time spans, which is beneficial for PolInSAR applications.

Acquisition protocols can be designed to increase or reduce the contribution of specific signals. A spatial baselines, if needed to create a DEM, can be obtained by using two (dual-pol) receiving antennas vertically displaced or by travelling different paths from which the same area can be observed with suitable geometry. The car-borne SAR systems has two channels alternately transmitting V and H signals and 4 receive channels that can be connected to the two antennas (two ports per antenna). On the other hand, the perpendicular baseline can be minimized by using a single dual-pol receiving antenna, which is of interest for polarimetric DInSAR (PolDInSAR) applications. Small spatial and temporal baselines allow to reduce geometrical and temporal decorrelation effects on the measurements, thus improving the accuracy of the parameter inversion.

The local terrain slope has an impact on the scattering mechanisms as a consequence of the varying incidence angles that influence penetration depth and vertical wavenumber [7–9]. This aspect should be investigated in the context of repeat-pass Pol(D)InSAR acquisitions, since a large variation of look angles from near-range to far-range can be expected from a typical car-borne acquisition geometry. Furthermore, the investigation of the suitability of different polarimetric models in various scenarios (e.g. different geometries and vegetation covers) is needed. Valuable knowledge would be gained by performing acquisitions of areas characterised by homogeneous vegetation cover but different terrain slopes.

Multi-temporal (repeat-pass) PolInSAR acquisitions further augment the observation space and can improve the polarimetric coherence [10]. In such case, the coherence optimization can be performed

simultaneously over a number of acquisitions (multi-baseline). As the scattering mechanism can in general change over time, different optimization strategies can be implemented. For example, the multi-temporal data set can be investigated in its entirety or over acquisitions subsets relevant to short time spans in which the scattering mechanisms are supposedly similar, for example only during specific weather conditions.

Taking advantage of the fine temporal resolution achievable with the car-borne SAR system, the PolIn-SAR performance can be assessed for different weather conditions and type of vegetation cover. Weather conditions have a strong impact on the signal scattering. After a rainfall, for example, the dielectric constant of the vegetation increases in dependence of the retained water, thus, in principle, reducing the penetration depth. Experiments using metallic reflectors conveniently positioned under the tree canopy could be performed to assess the signal penetration in different weather conditions. With reference to the wind speed, the coherence owed to the interferometric signal relevant to the ground should in principle remain roughly the same also during high wind speed intervals, while larger interferometric variations should be observed for the canopy. Such knowledge could be exploited to constrain the polarimetric optimization for the decomposition of the different scattering mechanisms. For example, by imposing a sufficiently small bound for the PolInSAR coherence variations of the ground scattering during strong wind speed periods and by assuming that the ground scattering remains roughly the same over a predefined time span and with the same acquisition geometry, it might be possible to identify the ground scattering over such time span. Nevertheless, the contribution from large tree branches and trunks, which also typically remain stable under high wind speed, could bias the decomposition.

Multi-frequency applications Another viable solution to expand the SAR observation space is by performing multi-frequency SAR acquisitions. While tree trunks and ground represent important contributions at L-band, higher frequencies such as X-band and above have a small penetration into the vegetation and interact mainly with the leaves of the vegetation canopy. Therefore, simultaneous acquisitions in multiple bands can provide complementary information of the observed scene and, in principle, improve the estimation of physical parameters of interest. For example, an estimation of tree height can be performed by differencing the DEM obtained via single-pass InSAR in the two frequencies, assuming that the interferometric phase for the lower band is mostly relevant to the ground (for example after polarimetric optimization). Other possible applications include classification and inversion of parameter models for example to estimate the above-ground biomass [11].

To investigate the potential of the multi-frequency approach, in future campaigns the L-band car-borne SAR system could be augmented with a Ku-band radar system (wavelength of 1.75 cm). Imaging and single pass interferometric results from a Ku-band car-borne SAR system were already shown in [12]. However, to allow for repeat-pass interferometric acquisitions at Ku-band, a millimeter or sub-millimeter positioning accuracy should be achieved. Therefore, correction of residual positioning error should be performed, for example via multisquint, autofocusing, and/or by relying on ground control point or persistent scatterers present in the imaged scene. The latter approach would benefit from the higher resolution achievable at Ku-band, potentially implying a higher number of persistent scatterers compared to the L-band system.

Low-cost positioning system   In the development of the car-borne SAR system, an important share of the overall system cost is owed to the navigation-grade INS. Generally, the cost of an INS scales with the performance of its inertial measurement unit (IMU), with tactical-grade or lower grade systems having performance that are orders of magnitude worst than navigation-grade systems, for example in terms of bias stability of accelerometers and gyroscopes, but also much lower cost.

In recent years, micro-electro-mechanical systems (MEMS) have attracted significant interest particularly thanks to their characteristics such as low cost, low weight, and compactness, which make them well suited for use in consumer devices and other applications with weight, cost, and energy constrains [13–15]. MEMS accelerometers and gyroscopes have undergone consistent performance improvement and nowadays MEMS-based IMUs with performance comparable to tactical-grade IMUs are available at the cost of few thousands euros [16], which is a substantial cost reduction compared to the hundreds thousands euros necessary for navigation-grade IMUs.

The suitability of lower grade INSs in the context of repeat-pass DInSAR applications, where positioning accuracy in the order of a fraction of the radar wavelength is necessary, needs to be assessed. The positioning performance of lower-grade systems can be improved in a number of ways, most of which are the focus of current research. A common approach is to increase the number of sensors whose outputs are integrated via loosely-coupled or tightly-coupled extended Kalman filters. Sensors commonly used for this purpose are odometers or Doppler radars for velocity aiding, dual-antenna GNSS receiver for orientation, velocity, and positioning aiding, and magnetic compass for orientation aiding [17–19].

Velocity or positioning aiding systems complementary to GNSS receivers are also beneficial for operational use in challenging GNSS environments where the presence of buildings, trees, or other natural obstacles can obstruct the line of sight to the satellites, thus causing the lost of satellite tracking with consequent worsening of the positioning performance.

Another emerging interesting solution is the integration of multiple low-cost MEMS-based IMUs in a redundant configuration [20–22].

Data fusion schemes employing non-holonomic constraints, that is constraints on the vehicle velocity, can contribute to improve the positioning accuracy if assumptions on the vehicle dynamics can be attained. For example the lateral velocity of the vehicle can be assumed zero if sideways vehicle slips can be neglected [23, 24]. Non-holonomic constraints, however, do not reduce the space of possible positions that the vehicle can assume.

In the case of repeat-pass measurements performed while travelling on the same road, as it is of interest for car-borne DInSAR, further constraints could be dependent on the shape of the road surface, for example by imposing that the height difference between different runs cannot exceed a certain threshold.

Future works with the car-borne SAR system could focus on the investigation of the above-mentioned data fusion schemes employing low-cost sensors, whose positioning performance can be compared to the navigation-grade INS in the context of repeat-pass DInSAR measurements.

REFERENCES

[1] S. Cloude and K. Papathanassiou, "Polarimetric SAR interferometry," *IEEE Transactions on Geoscience and Remote Sensing*, vol. 36, no. 5, pp. 1551–1565, 1998.

[2] K. Papathanassiou and S. Cloude, "Single-baseline polarimetric SAR interferometry," *IEEE Transactions on Geoscience and Remote Sensing*, vol. 39, no. 11, pp. 2352–2363, 2001.

[3] R. Treuhaft and S. Cloude, "The structure of oriented vegetation from polarimetric interferometry," *IEEE Transactions on Geoscience and Remote Sensing*, vol. 37, no. 5, pp. 2620–2624, 1999.

[4] M. Lavalle and S. Hensley, "Extraction of structural and dynamic properties of forests from polarimetric-interferometric SAR data affected by temporal decorrelation," *IEEE Transactions on Geoscience and Remote Sensing*, vol. 53, pp. 4752–4767, Sep. 2015.

[5] J. Lopez-Sanchez, J. Ballester-Berman, and Y. Marquez-Moreno, "Model limitations and parameter-estimation methods for agricultural applications of polarimetric SAR interferometry," *IEEE Transactions on Geoscience and Remote Sensing*, vol. 45, pp. 3481–3493, Nov 2007.

[6] F. Garestier and T. Le Toan, "Forest modeling for height inversion using single-baseline InSAR/pol-InSAR data," *IEEE Transactions on Geoscience and Remote Sensing*, vol. 48, pp. 1528–1539, Mar 2010.

[7] H. Lu, Z. Suo, R. Guo, and Z. Bao, "S-RVoG model for forest parameters inversion over underlying topography," *Electronics Letters*, vol. 49, pp. 618–620, Apr 2013.

[8] Q. Xie, J. Zhu, C. Wang, H. Fu, J. M. Lopez-Sanchez, and J. D. Ballester-Berman, "A modified dual-baseline PolInSAR method for forest height estimation," *Remote Sensing*, vol. 9, p. 819, Aug 2017.

[9] F. Kugler, S.-K. Lee, I. Hajnsek, and K. P. Papathanassiou, "Forest height estimation by means of Pol-InSAR data inversion: The role of the vertical wavenumber," *IEEE Transactions on Geoscience and Remote Sensing*, vol. 53, pp. 5294–5311, Oct 2015.

[10] M. Neumann, L. Ferro-Famil, and A. Reigber, "Multibaseline polarimetric SAR interferometry coherence optimization," *IEEE Geoscience and Remote Sensing Letters*, vol. 5, pp. 93–97, Jan 2008.

[11] O. Cartus, M. Santoro, U. Wegmuller, and B. Rommen, "Estimating total aboveground, stem and branch biomass using multi-frequency SAR," in *2017 9th International Workshop on the Analysis of Multitemporal Remote Sensing Images (MultiTemp)*, IEEE, Jun 2017.

[12] O. Frey, C. L. Werner, U. Wegmüller, A. Wiesmann, D. Henke, and C. Magnard, "A car-borne SAR and InSAR experiment," in *2013 IEEE International Geoscience and Remote Sensing Symposium*, pp. 93–96, IEEE, Jul 2013.

[13] R. Bogue, "MEMS sensors: past, present and future," *Sensor Review*, vol. 27, pp. 7–13, Jan 2007.

[14] R. Gonzalez and P. Dabove, "Performance assessment of an ultra low-cost inertial measurement unit for ground vehicle navigation," *Sensors*, vol. 19, no. 18, 2019.

[15] E. L. Hinüber, C. Reimer, T. Schneider, and M. Stock, "INS/GNSS integration for aerobatic flight applications and aircraft motion surveying," *Sensors (Switzerland)*, vol. 17, p. 941, Apr 2017.

[16] Honeywell Aerospace, *HG4930 MEMS Inertial Measurement Unit*. Available at https://aerospace.honeywell.com/en/learn/products/sensors/hg4930-mems-inertial-measurement-unit (accessed on 08.06.2021).

[17] P. D. Groves, *Principles of GNSS, inertial, and multisensor integrated navigation systems*. GNSS technology and applications series, Boston: Artech House, 2nd ed. ed., 2013.

[18] J. Parviainen, M. A. V. Lopez, O. Pekkalin, J. Hautamaki, J. Collin, and P. Davidson, "Using doppler radar and MEMS gyro to augment DGPS for land vehicle navigation," in *2009 IEEE International Conference on Control Applications*, IEEE, Jul 2009.

[19] B. Yang, L. Xue, H. Fan, and X. Yanga, "SINS/odometer/doppler radar high-precision integrated navigation method for land vehicle," *IEEE Sensors Journal*, pp. 1–1, 2021.

[20] G. de Alteriis, C. Conte, R. S. Lo Moriello, and D. Accardo, "Use of consumer-grade MEMS inertial sensors for accurate attitude determination of drones," in *2020 IEEE 7th International Workshop on Metrology for AeroSpace (MetroAeroSpace)*, pp. 534–538, Jun 2020.

[21] T. Zhang, W. Zhao, X. Sun, Y. Rong, J. Duan, J. Chen, L. Song, and Q. Pan, "Optimization on the precision of the MEMS-redundant IMU based on adhesive joint assembly," *Mathematical Problems in Engineering*, vol. 2020, p. 8855141, 2020.

[22] W. Zhao, Y. Cheng, S. Zhao, X. Hu, Y. Rong, J. Duan, and J. Chen, "Navigation grade MEMS IMU for a satellite," *Micromachines*, vol. 12, no. 2, 2021.

[23] G. Dissanayake, S. Sukkarieh, E. Nebot, and H. Durrant-Whyte, "The aiding of a low-cost strapdown inertial measurement unit using vehicle model constraints for land vehicle applications," *IEEE Transactions on Robotics and Automation*, vol. 17, no. 5, pp. 731–747, 2001.

[24] A. Angrisano, M. Petovello, and G. Pugliano, "Benefits of combined GPS/GLONASS with low-cost MEMS IMUs for vehicular urban navigation," *Sensors*, 2012.

6

ACKNOWLEDGEMENTS

I would like to thank Prof. Irena Hajnsek for granting me the opportunity to pursue a PhD in one of the most renowned universities in the world. Many thanks to Dr. Othmar Frey for sharing his knowledge with me, for guiding me through the perils and the pitfalls of radar processing, and for the many interesting technical and non-technical discussions. I would also like to extend my gratitude to Dr. Charles Werner for his support and for the fruitful discussions in which we engaged. Thanks to my current and former colleagues: Armando Marino, Simone Baffelli, Virginia Brancato, Adnan Siddique, Manuele Pichierri, Simon Zwieback, Onur Yuzugullu, Celia Lukas, Philipp Bernhard, Shiyi Li, Manuel Luck, Marcel Stefko, Lanqing Huang. They have all contributed in one way or another to accompanying me to the end of this adventure.

This journey would have not been the same without my new friends in Zurich, whom I could always count on for enjoyable moments.

A special thanks goes to Ms. Carlotta Orlando, that supported me during some of the most challenging periods that I lived while writing my thesis.

Lastly, but most importantly, I would like to thank my family for the unconditional love, trust, and support. I would not be where I am today without them.

Roberto Coscione
Zurich, 2021